

AD-A126 318

UV EMISSIONS AND THE ELECTRON DENSITY IN THE AURORAL  
AND LOW TO MID-LATIT..(U) BEERS ASSOCIATES INC RESTON  
VA D J STRICKLAND ET AL. NOV 82 AFGL-TR-82-0373

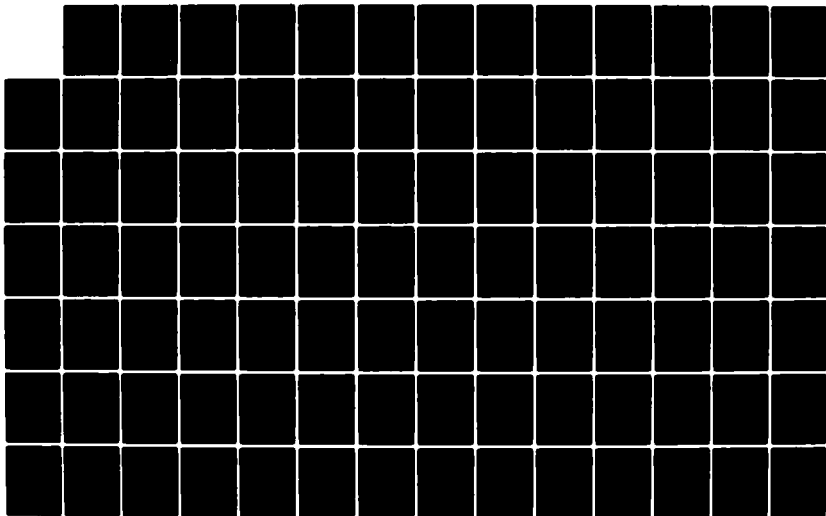
1/2

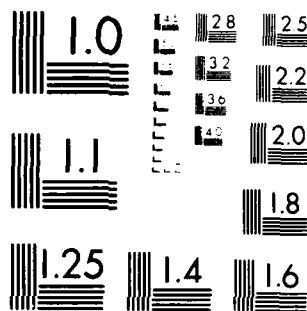
UNCLASSIFIED

F19628-81-C-0066

F/G 4/1

NL





MICROCOPY RESOLUTION TEST CHART  
NATIONAL BUREAU OF STANDARDS-1963-A

AD A 126318

AFGL-TR-82-0373

UV EMISSIONS AND THE ELECTRON DENSITY  
IN THE SUBARCTIC AND LOW TO MID-LATITUDE  
DAYTIME IONOSPHERES

D.J. Strickland  
R.E. Daniell

Beers Associates, Inc.  
P.O. Box 2549  
Reston, Virginia 22090

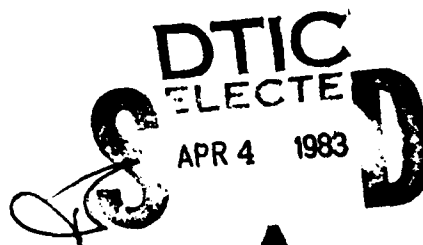
Final Report  
May 1981 - May 1982

November 1982

Approved for public release; distribution unlimited

DTIC FILE COPY

AIR FORCE GEOPHYSICS LABORATORY  
AIR FORCE SYSTEMS COMMAND  
UNITED STATES AIR FORCE  
HANSCOM AFB, MASSACHUSETTS 01731



88 04 04 03 5

Unclassified

MIL-STD-847A  
31 January 1973

SECURITY CLASSIFICATION OF THIS PAGE (When Data Entered)

REPORT DOCUMENTATION PAGE		READ INSTRUCTIONS BEFORE COMPLETING FORM
1. REPORT NUMBER AFGL-TR-82-0373	12. GOVT ACCESSION NO. AD-A126 318	3. RECIPIENT'S CATALOG NUMBER
4. TITLE (and Subtitle) UV Emissions and the Electron Density in the Auroral and low to mid-latitude Daytime Ionospheres		5. TYPE OF REPORT & PERIOD COVERED Final-81 May to 82 Sept
7. AUTHOR(s) D.J. Strickland and R.E. Daniell		6. PERFORMING ORG. REPORT NUMBER
9. PERFORMING ORGANIZATION NAME AND ADDRESS Beers Associates, Inc. P.O. Box 2549 Reston, Virginia		8. CONTRACT OR GRANT NUMBER(s) F19628-81-C-0066
11. CONTROLLING OFFICE NAME AND ADDRESS Air Force Geophysics Laboratory Hanscom Air Force Base, Mass. 01731 Monitor/Milton Klein/PHY		10. PROGRAM ELEMENT PROJECT TASK AREA & WORK UNIT NUMBERS 62101F 464306BA
14. MONITORING AGENCY NAME & ADDRESS (if different from Controlling Office)		12. REPORT DATE November, 1982
		13. NUMBER OF PAGES 144
		15. SECURITY CLASS (of this report) Unclassified
16. DISTRIBUTION STATEMENT (of this Report)  Approved for public release; distribution unlimited		
17. DISTRIBUTION STATEMENT (of the abstract entered in Block 20, if different from Report)		
18. SUPPLEMENTARY NOTES		
19. KEY WORDS (Continue on reverse side if necessary and identify by block number)  Aurora, Dayglow, Electron density, Electron transport, Ionosphere, Remote sensing, UV emissions		
20. ABSTRACT (Continue on reverse side if necessary and identify by block number)  A number of problems have been addressed in this work. They have been accompanied by extensive code development which has led to new capabilities such as the modeling of $O^+$ diffusion and to some significant reductions in code running times and disk allocation requirements. The given problems, either directly or indirectly, have dealt with the issue of using satellite optical		

DD FORM 1 JAN 73 1473 EDITION OF 1 NOV 68 IS OBSOLETE

Unclassified  
SECURITY CLASSIFICATION OF THIS PAGE (When Data Entered)

Unclassified

SECURITY CLASSIFICATION OF THIS PAGE (When Data Entered)

systems to monitor ionospheric conditions. The central question of interest is "How accurately can the E and F region electron density profiles ( $n_e$ ) be determined from satellite optical data on a global scale?". We have addressed this question as it pertains to the auroral E region and low to mid-latitude daytime E and F regions. Most of the reported work is on the first of these regions. The approach has been from first principles in which we start with either an incident auroral electron spectrum or a solar EUV/X-ray spectrum and proceed to determine the associated electron distribution function followed by its associated excitation and ionization rates, optical intensities, and electron and ion densities. In our auroral modeling, these quantities have been examined under a variety of conditions defined in terms of the incident electron spectrum and model atmosphere. We observe some significant relative variations among various UV intensities as the electron spectrum is changed. Features considered have been OI 1356 A,  $N_2^+$  3914 A, and LBH bands at 1273 A, 1325 A, 1354 A, and 1384 A. The relative variations are caused by the varying amount of  $O_2$  pure absorption from one feature to the next and are observed to be as much as a factor of  $\sim 5$  as the mean energy of the incident spectrum is changed from 1 to 10 keV. The results point to the potential of using satellite observed UV intensities to monitor auroral electron spectral hardness. They point also to the potential of monitoring the O density since O emissions such as OI 1356 A are sensitive to this density.

In our dayglow modeling, UV intensities and  $n_e$  have been calculated as functions of solar activity and model atmosphere. Both types of calculated quantities are shown to be sensitive to solar activity (factors of 2 to 3 variation from low to high activity). OI emissions, as expected, are also sensitive to changes in the O density.

Several quantities were calculated for comparison with data from the AFGL auroral E rocket program. These include electron spectra, ion and electron densities, and altitude profiles of several UV intensities. Overall good agreement is achieved between the calculations and preliminary versions of data so far made available to us.

Unclassified

SECURITY CLASSIFICATION OF THIS PAGE (When Data Entered)

# Table of Contents

<u>Section</u>		<u>Page</u>
1	Introduction and Technical Summary.....	1
2	Ionospheric Variability due to Neutral Winds and Electric Fields.....	7
3	Computer Code Development.....	9
4	The Chemistry of $O(^1S)$ and $N_2(A^3\Sigma)$ .....	12
	4.1 The $N_2(A)$ State and the Vegard-Kaplan System..	12
	4.2 The Chemistry of $O(^1S)$ .....	18
5	The Diffusion of $O^+$ in the F Region.....	21
6	The Effect of Rayleigh Scattering on Nadir Observed UV Intensities From Satellites.....	29
	6.1 General Comments.....	29
	6.2 Basic Expressions.....	30
	6.3 Derivation of the Intensity Equation.....	33
	6.4 Forms of $S_0$ .....	35
	6.5 Parameter Values.....	38
	6.6 Results.....	45
7	Predictions for Comparison with Data from the 1981 AFGL Auroral E Rocket Program and from the ISIS II Satellite.....	53
	7.1 Predictions for the Continuous Aurora.....	53
	7.2 Electron Backscatter Prediction for ISIS II Electron Spectrometer Data Analysis.....	62



A

## Table of Contents (continued)

<u>Section</u>		<u>Page</u>
8	UV Emissions and the Electron Density in the Daytime Ionosphere.....	66
	8.1 Background.....	66
	8.2 Computational Model.....	67
	8.3 Description of Input/Output Information.....	71
	8.4 Calculated Photoelectron Flux and Volume Excitation Rates.....	73
	8.5 Optical Intensities and Electron Densities....	73
9	References.....	81
	Appendix.....	85

# List of Figures

<u>Figure</u>		<u>Page</u>
1	Volume Production, Emission, and Loss Rates for the $v' = 0$ Progression of the Vegard-Kaplan System.....	15
2	Volume Production, Emission, and Loss Rates for the $v' = 0$ Progression of the Vegard-Kaplan System.....	16
3	Energy Dependence of Vegard-Kaplan Emission for an Energy Deposition Rate of $1.0 \text{ erg cm}^{-2}\text{sec}^{-1}$ in the Jacchia (1977) Model Atmosphere.....	17
4	Zenith Viewing Column Emission Rates for OI 5577 A and $\text{N}_2^+$ 3914 A.....	20
5	An Example of the Results of the Diffusion Calculation Using the Jacchia (1977) Model Atmosphere and a Maxwellian Distribution for the Incident Electrons.....	28
6	Satellite Nadir Viewing Geometry.....	34
7	Rayleigh Scattering Cross Section.....	40
8	$\text{O}_2$ Absorption Cross Section Taken From Sullivan and Holland (1966).....	41
9	$\text{O}_3$ Absorption Cross Section Taken From Sullivan and Holland (1966).....	42
10	Rayleigh Scattering Optical Depth $\tau$ and Pure Absorption Optical Depth $t$ at $z=0 \text{ km}$ . Absorption is by $\text{O}_2$ and $\text{O}_3$ .....	43
11	Optical Depths $\tau$ and $t$ Versus Altitude at Selected Wavelengths.....	44
12	Solar Flux Based on Tabulation Appearing in Banks and Kockarts (1973 A).....	46
13	Rayleigh Scattering Source Functions at 96 km for Solar Flux $\pi F_0$ Normalized to Unity at Each Wavelength.....	47
14	Similar to Figure 13 Except at 47 km.....	48
15	Functions $f_s$ and $4\pi I$ for Rayleigh Backscattering of Solar Radiation.....	50

# List of Figures (continued)

<u>Figure</u>		<u>Page</u>
16	Function $f_A$ for Rayleigh Backscattering of Auroral Radiation.....	52
17	Calculated auroral electron spectra.....	53
18	Calculated ion densities based on the incident electron spectrum shown in Figure 17.....	56
19	Calculated (symbols) and measured (curves; Swider and Narcisi, 1981) fractional ion abundances.....	58
20	Calculated zenith viewing intensities for conditions described in text.....	59
21	Calculated zenith viewing intensities for conditions described in text.....	60
22	Calculated zenith viewing intensities for conditions described in text.....	61
23	ISIS II electron spectrometer data for pitch angles of $7^\circ$ and $14^\circ$ ( $0^\circ$ refers to downward direction along field lines).....	63
24	Incident ( $\mu > 0$ ) and calculated backscattered ( $\mu < 0$ ) electron spectra based on ISIS II data such as appear in the previous figure.....	64
25	Comparison of calculated and measured $4\pi$ integrated photoelectron spectra.....	74
26	Solar spectrum for low solar activity used in the calculations.....	75
27	$O(^5S)$ and $N_2(a^1\Pi_g)$ volume excitation rates based on the solar spectrum in Figure 26.....	76
28	Zenith and Nadir viewing $OI$ 1356 A and $N_2$ LBH 1383 A dayglow intensities.....	78
29	Calculated daytime electron density. Labeling is the same as in Figure 28.....	79

## List of Tables

<u>Table</u>		<u>Page</u>
1	Cases for which results have been obtained with code PEGFAC.....	80

## Section 1

### Introduction and Technical Summary

In this report, we discuss work undertaken to better understand the properties of optical emissions in the auroral and low to mid-latitude daytime ionospheres. The approach is to use first-principles techniques to calculate the needed quantities under a variety of geophysical conditions. In particular, we have calculated optical intensities and electron densities  $[n_e(z)]$  noting their variability from one set of conditions to another. A long term goal of this work is to determine the usefulness of satellite observed optical intensities for deducing the electron density profile. This goal is of interest to as much of the global ionosphere as the technique proves applicable although here the discussion is limited to those regions noted above.

We know of no prominent emission features in the auroral and daytime ionospheres which give direct signatures of the ions present unlike, say, the  $O^+$  recombination emissions in the tropical nighttime airglow (see, e.g., Chandra et al., 1975 and Tinsley and Bittencourt, 1975).  $O^+$  834 Å comes closest to fulfilling the requirement since  $O^+$  can affect the 834 Å intensity through multiple scattering (see Feldman et al., 1981 and Kumar et al., 1982). This, in itself, poses a difficult problem which we shall not address here. It then becomes a two step process to obtain  $n_e$  from optical measurements. We must first obtain a representation of the source (solar ionizing spectrum or incident auroral electron spectrum) followed by its use in calculating  $n_e$ . The emphasis in this work is on how well the source spectrum can be determined from optical data. To address the second step, we then calculate  $n_e$  examining its sensitivity to variations in the source spectrum and the major neutral densities.

The variability of  $n_e$  can pose some serious problems to the above technique. This variability is caused by 1) time and spatial changes in the source, 2) the same type of changes in the major neutral density profiles, and 3) mechanisms which produce bulk transport of the plasma. As noted above, item 1 shall receive most of our attention. Item 2 is important because uncertainties

introduced can affect both the accuracy of the deduced source spectrum and the subsequently calculated  $n_e$  profile. The accuracy of  $n_e$  is dependent not only on the assumed source spectrum, but also on assumed neutral densities through chemistry and diffusion. More shall be said about item 2 in the next few paragraphs. Item 3 has to do with winds and fields and will be briefly discussed in the next section. Beyond this, however, we shall restrict ourselves to conditions for which  $n_e$  is dependent only on the ionizing source, chemistry, and diffusion.

The technique being addressed is most attractive for situations in which the density profiles of  $N_2$ ,  $O_2$ , and  $O$  are known. Then, variability of one optical intensity relative to another with changes in either time or location can be directly related to variability in source conditions. The neutral density profiles cannot be precisely known, however, because of their intrinsic variability and the difficulty of precisely describing that variability. The latter problem is due to the approximate nature of existing thermospheric density models (for recent models, see Jacchia, 1977; Hedin et al., 1977 a,b; Barlier et al., 1978; Hedin et al., 1981) and to the limitations of measurement techniques. Of particular interest here are satellite based measurements. In situ measurements can be expected to be the most reliable but may be insufficient for specifying altitude profiles to the degree of accuracy desired. Optical remote sensing techniques, on the other hand, do hold a potential for measuring column densities which can be used to scale corresponding volume density profiles. The next paragraph addresses this problem. Returning to the original issue of this paragraph, one of the objectives of the present work must be to determine just how precisely the major neutral densities need to be known to make the technique under investigation practical. The required precision is dependent on source conditions and, of course, on instrumental conditions. We have begun to answer the question of precision as it relates to source conditions which will be taken up later in this report.

The problem raised in the previous paragraph is whether it is possible to separate the effects of neutral density variations from source variations when using optical data. Various researchers are actively investigating the problem of sensing the neutral atmosphere (Newman et al., 1982 and

Meier and Anderson, 1982). Their concern has been with the analysis of satellite observed limb profiles for features such as OI 1356 A and N<sub>2</sub> LBH bands. We have concentrated our efforts on nadir viewing observations and we believe that with the right choice of features and instrumental parameters, the source and atmospheric variabilities can be decoupled. This is strengthened by the fact that there are limitations to the relative variability between N<sub>2</sub> and O<sub>2</sub> densities in the regions of peak excitation (for either auroral or daytime conditions). Furthermore, the models cited above are probably more than adequate under most observing conditions for describing these relative densities. It then becomes attractive to use selected N<sub>2</sub> band emissions for initially characterizing the source spectrum. For auroral conditions, their relative strengths indicate the hardness of the electron source spectrum through either of the basic mechanisms of pure absorption or quenching, depending on the features. Given a representation of the spectral hardness, the magnitudes of the observed intensities then determine the energy content of the spectrum. For daytime conditions, there is little variation in the hardness of the relevant part of the solar ionizing spectrum and so here, it is the energy content of the spectrum we seek. The magnitudes of the observed intensities provide this information.

With an initial characterization of the source spectrum, we may turn to the problem of better determining the neutral densities. The atomic oxygen density is of prime interest since it probably experiences the greatest relative variability (see above papers on thermospheric modeling) and has associated with it some key UV emission features (examples are OI 1304 A, OI 1356 A, and OI 2972 A). Because O is a minor species when considered over the entire excitation region, its optical intensities are sensitive to its overall density. Thus, given the source spectrum, a measure of say, the OI 1356 A intensity (with a minor contamination from N<sub>2</sub> LBH 1354 A) gives a direct measure of the magnitude of the O density profile. We may now repeat the process to further improve both the source representation and neutral density description. Quantitative information related to the discussion over the past few paragraphs will follow in subsequent sections.

A summary of the contract work now follows. This will be given in terms of results and improvements in models and codes. Some of the results have already been presented at the 1981 Annual Fall meeting of the AGU and in the papers by

Strickland et al. (1982b) submitted to JGR, and Strickland et al. (1982c) submitted to the AIAA. We begin by listing key results. Conclusions are based on the assumption that fields and winds are not significantly perturbing the plasma. Since this is frequently not the case in the F region, the results to follow refer to the E and possibly lower F regions.

- 1) In our auroral modeling, selected UV intensities have been found to have noticeable variations relative to one another as the incident electron spectrum and model neutral densities are varied. Some features whose intensities show this behavior are the LBH bands at 1273 Å, 1325 Å, 1354 Å, and 1383 Å, Vegard-Kaplan bands such as that at 2672 Å, and the atomic oxygen lines at 1356 Å and 2972 Å. The calculated electron density profile shows significant variation with the above variations in the intensities. We conclude that good satellite measurements of intensities such as the above should allow one to deduce  $n_e$  throughout the region of important optical emission to better than 50%. Some qualifications are called for and we refer the reader to the appendix.
- 2) For daytime conditions, there is little relative variation of intensities as the solar spectrum changes. Magnitudes of both intensities and the  $n_e$  profile do change, however, by factors of two in going from solar minimum to maximum conditions. An advantage of there being little relative variation among intensities is that altitude profiles of emissions and  $n_e$  remain essentially constant with time and location for similar solar zenith angles and exospheric temperatures. Changes in profile shape which do take place as a result of changes in these two parameters cause no problem since they can be accurately modeled. We conclude that good satellite measurements of intensities such as listed above should give a good magnitude measure of the ionizing part of the solar spectrum as well as the O density profile. From this information, we expect that  $n_e$  in the E and F regions can be determined to even greater accuracies than in the auroral E region under quiescent plasma conditions.

- 3) AFGL conducted an auroral E rocket program in March of 1981 to observe the continuous aurora. We have provided a variety of predictions for comparison with data. Quantities include intensity altitude profiles of numerous optical features, ion density profiles, and  $n_e(z)$ . Some of the data have been made available to us in preliminary form. We find good agreement in the fractional abundances of  $\text{NO}^+$ ,  $\text{O}_2^+$ ,  $\text{O}^+$  and  $\text{N}^+$ . Agreement in  $n_e$  to better than 50% is also obtained. Most of the calculated intensity profiles also compare favorably in shape and magnitude with the data from the fielded photometers and UV spectrometer. More definitive statements will be made when the data are released in their finalized forms but current indications suggest that the continuous aurora can be effectively modeled.
- 4) A satellite optical experiment designed to observe far UV ( $\leq 2000 \text{ \AA}$ ) emissions in the nadir direction will be limited to monitoring the region above  $\sim 100 \text{ km}$ . This is, of course, desirable for our problem of interest since it concerns remote sensing of the ionosphere. The question arises as to how long the wavelength of an emission feature can be before Rayleigh scattering as well as scattering from clouds, aerosols, and the earth's surface begin to produce a backscattered intensity interfering with the measurement of the direct ionospheric component. The answer depends on whether solar radiation is present or not. For auroral observations in the absence of sunlight, backscattering does not pose a problem shortward of  $\sim 3000 \text{ \AA}$ . For daytime conditions, this wavelength is in the Schumann-Runge band absorption region near  $1900 \text{ \AA}$ . A detailed discussion of this subject is given in Section 6.

To complete the summary, we note improvements that have been made to our models and corresponding codes. As is usually the case for this type of activity, the implementations constituted an important part of our overall effort. The following list highlights the most important of the improvements.

- 1) The chemistry codes now allow for diffusion of  $O^+$  in the F region. Section 5 details the applied algorithm.
- 2) The electron temperature is now calculated along with ion and neutral species in the chemistry codes. Heat conduction is not accounted for but will soon be added.
- 3) Intensities are now calculated for many more features than earlier in this program. Most additions are to band systems. ( $N_2^+$  1N,  $N_2$  2P,  $N_2$  VK,  $N_2$  LBH, and  $N_2$  BH).
- 4) Reaction rate coefficients have been updated as data became available. The chemistry of  $O(^1S)$  and  $N_2(A^3\Sigma^-)$  was examined in some detail leading to better descriptions of the emissions at 01 5577 Å and 01 2972 Å and in the Vegard-Kaplan system.
- 5) Code PEGFAC became functional on the AFGL system. This code calculates photoelectron spectra and associated excitation rates. Modifications were also made to the auroral chemistry code for daytime applications.

and

- 6) Significant reductions were made in disk storage and runtime requirements for key codes. Among the advantages of such reductions has been much better "turn around" time for the auroral electron transport code.

## Ionospheric Variability due to Neutral Winds and Electric Fields

In the F region ionosphere (above 180 km) both the ion-neutral and electron-neutral collision frequencies are much less than the respective gyro-frequencies. This means that the mobility of a charged particle is much greater along a field line than across field lines. The neutral winds of the thermospheric circulation produce a frictional force on the ionospheric plasma, but only the component of that force which acts along a field line is effective at imparting motion to the plasma. Magnetic field lines lie approximately in meridional planes and rise in altitude toward the equator. During daytime hours, the normal thermospheric circulation is from equator to pole (Bauer, 1973 and Evans, 1976) which tends to drive the plasma down. This reduces not only the altitude of the ionization peak, but also the peak concentration since chemical losses are larger at the lower altitudes. At middle latitudes the effects of these winds can be as important as diffusion, resulting in a lowering of the  $F_2$  peak by  $\sim 50$  km and a reduction in peak electron density by  $\sim 35\%$  (Hargreaves, 1979 and Banks and Kockarts, 1973B). However, the thermospheric circulation is quite variable on a daily basis which makes the ionospheric variability difficult to predict. One source of variability is the energy deposited at high latitudes during geomagnetic substorms which can alter the global thermospheric circulation even reversing the direction of flow (Evans, 1976 and Prolss, 1982). Furthermore, the resistance of ions to cross field motion can alter the thermospheric winds in the altitude regime above 300 km, further complicating the picture.

In the E region ionosphere (105-160 km) the ion cross field mobility is considerably larger than that of electrons. In this altitude regime neutral winds induce a charge separation which results in a global electric field system. Because magnetic field lines are nearly equipotentials, this electric field system is mapped into the F region where it causes plasma ( $\mathbf{E} \times \mathbf{B}$ ) drifts (Hargreaves, 1979). One may think of the E region winds acting as a dynamo generator while the F region plasma responds as an electric motor. The effect of

the electric field is generally smaller than that due to F region winds and varies throughout the day.

In addition to the large scale effects caused by thermospheric winds and the dynamo electric field, there are small scale structures - ionospheric irregularities - which have a variety of sources. The irregularities are present in both the E region and F region and at all latitudes (Ossakow, 1979 and Fejer and Kelley, 1980). At auroral and equatorial latitudes the primary causes of ionospheric irregularities are plasma instabilities, although the relative importance of neutral dynamics in the explanation of equatorial spread F is subject to debate. At mid-latitudes the situation is less well understood. Wind shears are known to produce sporadic E layers while traveling ionospheric disturbances have been explained by gravity waves propagating from below or from the auroral zone (Hargreaves, 1979). A number of plasma mechanisms have been proposed to explain smaller scale structures, but verification of these hypotheses awaits more complete sets of observational data (Fejer and Kelley, 1980).

Both E region and F region thermospheric winds can have a significant influence on the electron distribution above 200 km or so. They are hard to observe and continue to be the subject of theoretical and experimental research. If the winds are known, their effects on the ionosphere can be determined (Banks and Kockarts, 1973B). The principal implication for satellite monitoring of the ionosphere is that some method of measuring or calculating thermospheric winds must be developed. Global models of the thermospheric circulation provide a useful beginning but the effects of geomagnetic activity must also be included if reasonable accuracy is to be obtained. Since ionospheric irregularities are less well understood, particularly at mid-latitudes, they present a formidable problem for satellite monitoring. These problems are not addressed further in this report, but remain important research subjects.

## Section 4

### Computer Code Development

Substantial improvements were made in key computer codes during the course of this work. These improvements will be noted below as we briefly describe the function of each code which has been applied to our auroral and daytime modeling efforts. The following list identifies these codes:

- 1) MX
- 2) B3C
- 3) PRATES
- 4) CHEM1
- 5) PEGFAC
- and 6) CHEM2

The first four are used to model electron transport, chemistry, and photon emission in the auroral ionosphere and come from previous work, part of which has been recently sponsored by AFGL (Strickland, 1981). The remaining two codes are used for daytime ionospheric modeling. PEGFAC comes from independent work while CHEM2 comes from modifications of CHEM1 performed under this contract. Information on individual codes now follows.

Code MX generates matrices approximating the Boltzmann collision integral for electron scattering and energy loss as well as secondary electron production. A description of the applied transport equation may be found in the appendix. Two improvements to MX have recently been made. One of these decreases the running time by more than a factor of 10. This was made possible by replacing a numerically based matrix inversion technique by an analytic one. The matrices to be inverted are of dimension  $6 \times 6$  and can be decomposed into a product of matrices with dimensions  $3 \times 3$  and  $2 \times 2$ . This enables one to apply analytic techniques to the inversion without being overly burdened with algebra. The second improvement has led to a significant reduction in the number of matrix elements to be stored on disk. Basically, redundant elements have been removed before writing to disk

and re-inserted at the time they are needed to perform the transport calculation.

Code B3C is the Boltzmann three (3) constituent electron transport code. (see Strickland et al., 1976 and the appendix). It calculates the differential electron spectrum  $\phi(z, E, \mu)$  in units of electrons/cm<sup>2</sup>-s-eV-sr where  $z$ ,  $E$ , and  $\mu$  refer to altitude, energy, and cosine of the pitch angle. B3C currently allows for 35 altitudes, 50 energies, and 20  $\mu$  values. The most noteworthy improvement recently made allows for local energy deposition at low energies, thereby significantly reducing memory requirements and running time. The local energy deposition approximation has been found to be valid so long as most of the energy content of the incident spectrum lies above the transition energy chosen for going from the transport to the local description. For an incident spectrum characterized by, say, a 2 keV Maxwellian distribution, the transition energy can be chosen to be as high as several hundred eV.

Code PRATES calculates a variety of volume excitation and ionization rates using  $\phi(z, E, \mu)$ . The rates provide the driver for chemistry modeling in CHEM1. PRATES is now significantly larger than it was earlier in this work following the above described modifications to B3C. The expansion is due to the transferal of numerous routines from B3C which performed various operations following the actual transport calculations giving  $\phi(z, E, \mu)$ . One such operation is the testing of energy conservation. The reason for the above transferal was to increase the "turn around time" of B3C runs which had become approximately one day.

Code CHEM1 solves a set of time dependent rate equations for numerous ion and neutral species. It currently also calculates optical intensities for a large number of atomic and molecular emission features. CHEM1 has been undergoing continued development throughout the given contract period of performance. Some of this effort has involved updating chemical reaction rate coefficients and adding emission parameters for additional optical features. The rest has led to CHEM1's ability to treat diffusion and calculate the electron temperature,  $T_e$ . A discussion of the diffusion work appears in Section 5.  $T_e$  is currently calculated assuming no conduction but our plans call for the removal of this restriction during the next phase of work on the code.

Code PEGFAC calculates the differential photoelectron spectrum  $\phi(z, E)$  in units of electrons/cm<sup>2</sup>-s-eV-4 $\pi$  sr. Section 8 details PEGFAC's history, computational model, input data, and selected results. Most of the required effort related to PEGFAC was directed to its transferal to the AFGL CDC computing system from a non-CDC system upon which it had resided.

Code CHEM2 serves in the same capacity for daytime ionospheric modeling as CHEM1 does for auroral modeling. As noted above, CHEM2 was developed using CHEM1 as its basis. Differences between these codes are minor as of this writing and primarily relate to the handling of input data generated by respective electron flux/excitation rate codes.

## Section 4

### The Chemistry of $O(^1S)$ and $N_2(A\ ^3\Sigma)$

Because the  $O(^1S)$  emission feature at 5577 Å is one of the most prominent auroral features, it should be included in any comprehensive auroral model. Although non-ionospheric emission, scattering, and albedo effects prevent the useful nadir observation of this emission from satellites, its calculation does provide a useful check on the chemistry model. In addition, the chemistry of  $O(^1S)$  is coupled to that of  $N_2(A\ ^3\Sigma_u^+)$  which gives rise to the Vegard-Kaplan bands. These bands may prove useful for monitoring the hardness of precipitating electron spectra from satellites. Consequently, we have directed some of our effort to include the best available information on  $O(^1S)$  and  $N_2(A)$  in our model.

#### 4.1 The $N_2(A)$ State and the Vegard-Kaplan System

The  $N_2(A\ ^3\Sigma_u^+)$  metastable state is populated by direct excitation from the ground state and by cascade from higher lying triplet states. Since the cascade occurs in a much shorter time than the lifetime of the  $A\ ^3\Sigma$  state, we can calculate the total production rate for  $N_2(A\ ^3\Sigma_u^+)$  by summing the electron impact cross sections of all the triplet states. Since the cross sections for the  $B\ ^3\Pi_u^-$ ,  $E\ ^3\Pi_g^+$ , and  $D\ ^3\Sigma_u^+$  cross sections are much smaller than the others, we have neglected them in the sum. Also, because approximately half of the  $C\ ^3\Pi_u$  state dissociates, we only include half of its cross section:

$$\tau_{\text{total}} = \sigma(A\ ^3\Sigma_u^+) + \sigma(B\ ^3\Pi_g) + \frac{1}{2} \sigma(C\ ^3\Pi_u) + \sigma(W\ ^3\Delta_u)$$

Following Sharp and Torr (1979) we concentrate on the  $v' = 1$  vibrational level. Using the relative populations of the different vibrational levels as calculated by Cartwright (1973), and the transition probabilities of Shemansky (1969) we have calculated the emission rates for each vibrational level assuming

no quenching. In the steady state and in the absence of quenching, the production rate must equal the emission rate. Using our calculated emission rates, we have calculated the relative production rates of the  $v' = 0$  and  $v' = 1$  levels, and we assume that these rates are valid even when quenching becomes important.

There are only two loss mechanisms for the  $N_2(A^3\Pi_u^+)$  state: quenching and emission. Except at the lowest altitudes where  $O_2$  becomes important, the dominant quencher is atomic oxygen. For completeness, we have also included quenching by  $N_2$  and  $NO$ . The density of any vibrational level is determined by the balance between production and loss:

$$p(A, v') = (q_{v'} + \sum_{v''} A_{v', v''}) n(A, v') \quad (1)$$

where  $q_{v'} = \sum_i k_i(v') n_i$  is the sum of the quenching rates due to each neutral species,  $k_i(v')$  is the quenching coefficient for the  $v'$  level, and  $A_{v', v''}$  is the transition probability from the  $v'$  level of the A state to the  $v''$  level of the ground state. The actual emission from any vibrational level is

$$\epsilon(A, v') = (\sum_{v''} A_{v', v''}) n(A, v') \quad (2)$$

Eliminating the concentration of the  $v'$  level between Equation (1) and (2) results in

$$\epsilon(A, v') = \frac{A_{v', p(A, v')}}{q_{v'} + A_{v', p(A, v')}} p(A, v')$$

where

$$A_{v'} = \sum_{v''} A_{v'v''}.$$

We have adopted the transition probabilities given by Vallance Jones (1974). Since these are somewhat larger than those reported by Cartwright (1978), they may need to be revised in future calculations. The quenching coefficients,  $k_i(v')$  were taken from the review by Torr and Torr (1982). Unfortunately, the quenching coefficient for the most important species, 0, is also the most uncertain. A recent laboratory measurement (Piper et al., 1981) found  $k_0(v' = 0) = 2.8 \times 10^{-11}$  and  $k_0(v' = 1) = 3.4 \times 10^{-11} \text{ cm}^3 \text{ s}^{-1}$ . This is in general agreement with the values adopted by Cartwright (1978) based on the ground based observations of Vallance Jones and Gattinger (1976). However, these values are in sharp disagreement with the rocket determination by Sharp (1971) who found  $k_0(v' = 0) = 9 \times 10^{-11}$  and  $k_0(v' = 1) = 2 \times 10^{-10}$ . Until this discrepancy is resolved, any calculation of the Vegard-Kaplan emissions is subject to some uncertainty.

Using the laboratory values of  $k_0(v')$ , we have calculated the Vegard-Kaplan emission for several incident electron energies. Volume production, quenching, and emission rates for 1 keV and 5 keV Maxwellian cases are displayed in Figures 1 and 2, respectively. Column emission rates are shown in Figure 3 as a function of incident electron energy. The total emission from each vibrational level and the two most prominent bands of each progression are displayed. Also shown is the energy dependence of the total emission when the larger quenching coefficients of Sharp (1971) are used. Some noticeable differences in emission are seen to occur when using the Sharp coefficient values in place of the Piper values. Since the weight of evidence favors the Piper et al. (1981) quenching coefficients, it is likely that we can expect a factor of 3 to 5 variation in some of the stronger bands as the incident electron energy changes from 1 to 5 keV.

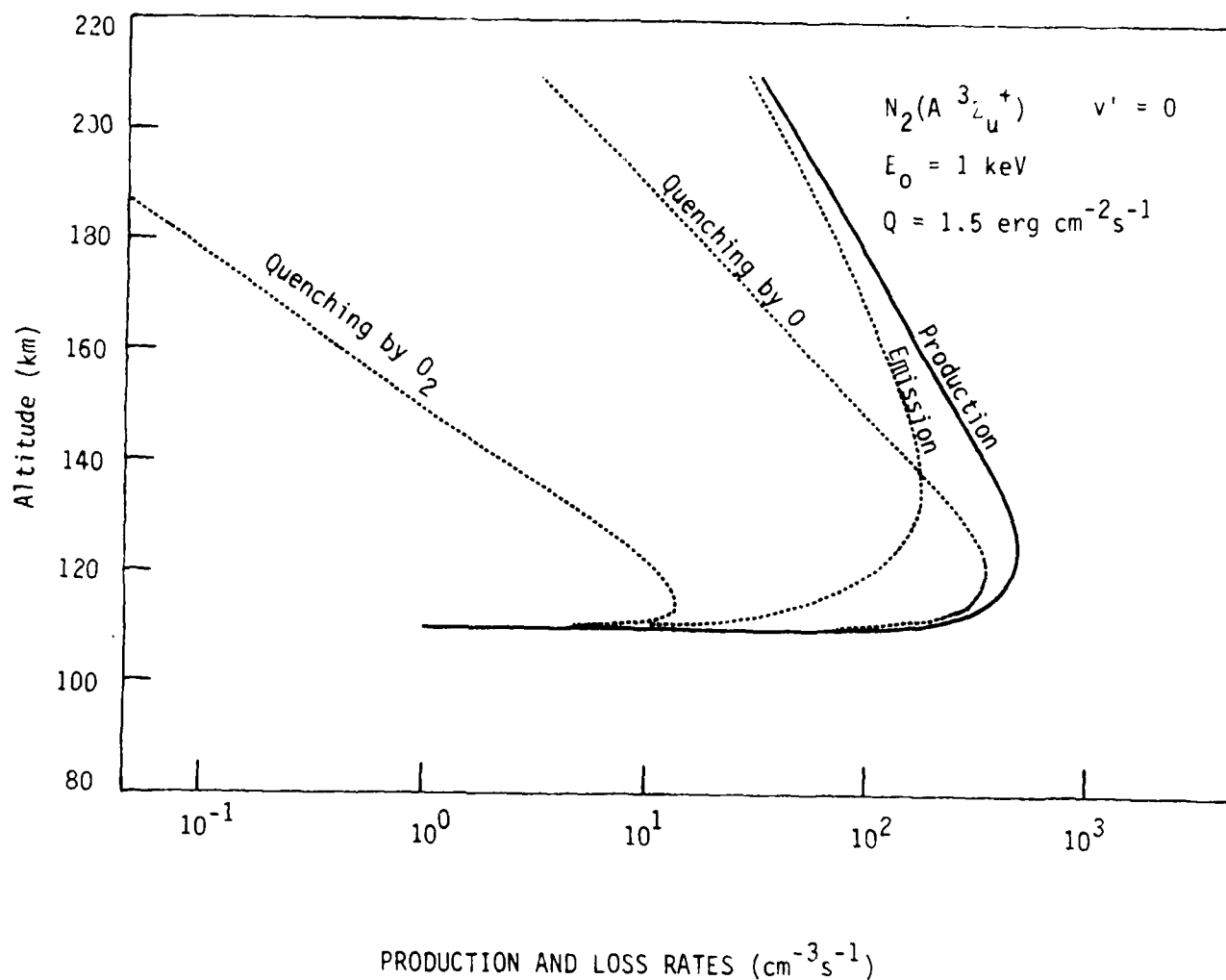


Figure 1 Volume Production, Emission, and Loss Rates for the  $v' = 0$  Progression of the Vegard-Kaplan System. The Incident Electron Spectrum was a 1 keV Maxwellian. We have used the quenching coefficients of Piper et al. (1981) and the Jacchia (1977) model atmosphere.

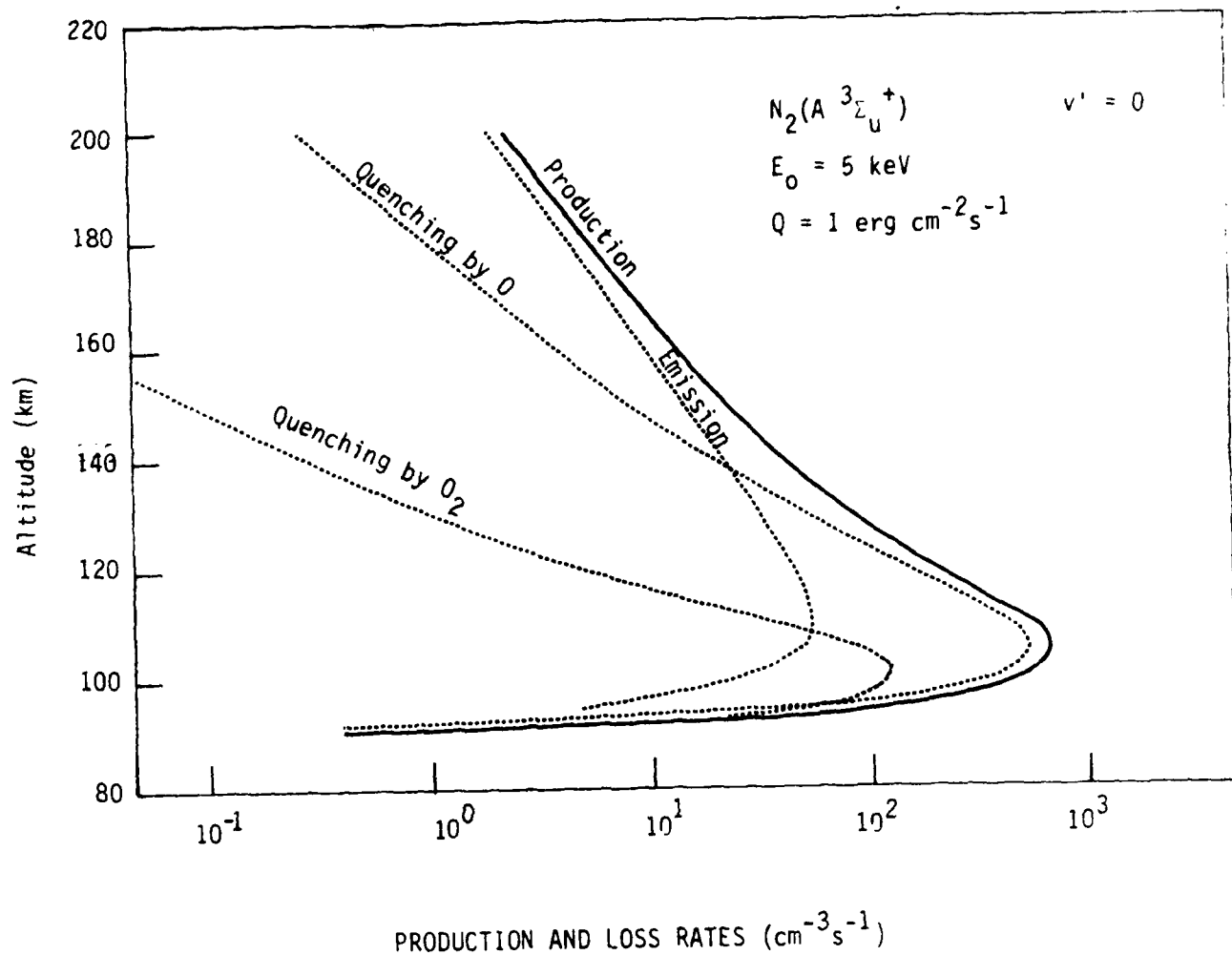


Figure 2 Volume Production, Emission, and Loss Rates for the  $v' = 0$  Progression of the Vegard-Kaplan System. Conditions are the same as given in Figure 1.

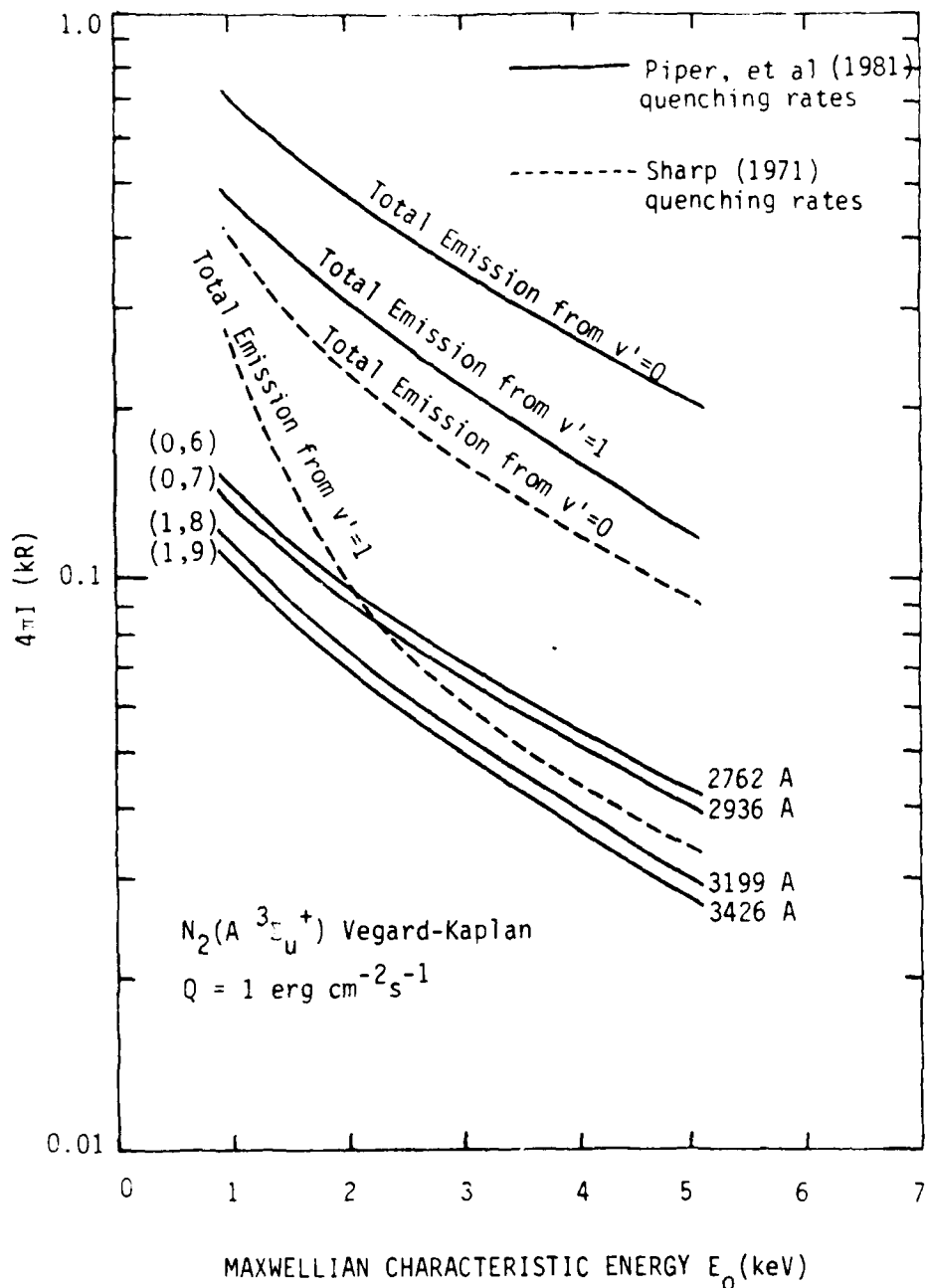
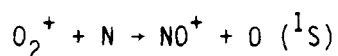
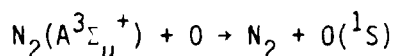
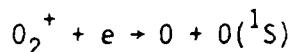


Figure 3 Energy Dependence of Vegard-Kaplan Emission for an Energy Deposition Rate of  $1.0 \text{ erg cm}^{-2} \text{ sec}^{-1}$  in the Jacchia (1977) Model Atmosphere. Total Emission From the  $v' = 0$  and  $v' = 1$  Progressions are Shown for two Different Values of the Atomic Oxygen Quenching Coefficient (see text). In Addition, the Emissions Rates of the two Most Prominent Bands in Each Progression are Shown for the Most Probable Value of the Quenching Coefficient.

#### 4.2 The Chemistry of $O(^1S)$

Aside from direct excitation by energetic-electrons, the principal sources of  $O(^1S)$  are (Torr and Torr, 1982):



The temperature dependent reaction rate for dissociative recombination of  $O_2^+$  has been given by Roble and Rees (1977) which is similar to the rate determined from atmospheric explorer measurements (Torr and Torr, 1978). The branching ratio varies from 2% to 10% depending on the vibrational level of  $O_2^+$  (Torr and Torr, 1982). We have adopted a value of 8%. For the third reaction,  $O_2^+$  with N, we have adopted a value of  $2.5 \times 10^{-11} \text{ cm}^3 \text{ s}^{-1}$  which falls in the middle of of the range reported by Torr and Torr (1982).

Sharp and Torr (1979) determined the rate of production of  $O(^1S)$  from the quenching of  $N_2(A^3\Sigma_u^+)$  by O. Using the population of the  $v' = 1$  level of  $N_2(A^3\Sigma_u^+)$ , whose calculation is described in the preceeding section, and an efficiency of 25%, they obtained the effective rate  $3.6 \times 10^{-11} \text{ cm}^3 \text{ s}^{-1}$ . Note that this rate, when multiplied by the atomic oxygen concentration and the population of the  $v' = 1$  level of  $N_2(A^3\Sigma_u^+)$ , gives the total production of  $O(^1S)$  from all vibrational levels of  $N_2(A)$ .

The principal chemical losses we have included are quenching by O, NO, and  $O_2$ . Of these, quenching by  $O_2$  is the most important one. We have used a temperature dependent coefficient for this reaction from Hyman and Julienne (1975).

We are now calculating the  $O(^1S)$  density and its corresponding 5577 Å emission using the above described information. Figure 4 gives an example of a zenith viewing 5577 Å column emission rate for a incident electron spectrum given by a 1 keV Maxwellian with an energy content of  $1 \text{ erg/cm}^2\text{-s}$ . Also included is the emission for  $N_2^+$  at 3914 Å since it is commonly measured along with 5577 Å in the same experiment. The observed ratio for the column emissions (5577 Å/3914 Å) is generally between 1 and 2 which provides us with some confidence that we are achieving a reasonable description of the 5577 Å emission.

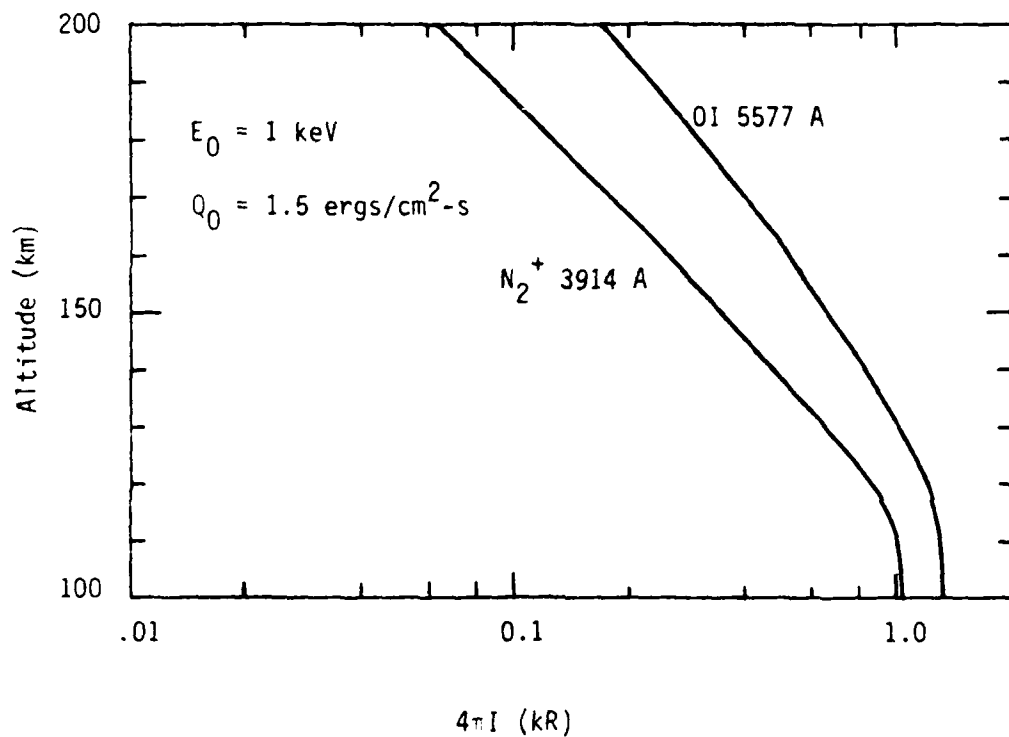


Figure 4 Zenith Viewing Column Emission Rates for OI 5577 Å and  $N_2^+ 3914 \text{ Å}$ . The Incident Electron Spectrum is Characterized by a Maxwellian Distribution With Characteristic Energy and Energy Content as Shown.

## Section 2

### The Diffusion of $O^+$ in the F Region

In the dayside and auroral ionospheres, the F2 region is predominantly  $O^+(^4S)$  (hereafter referred to as  $O^+$ ). Calculations of the  $O^+$  density (which is equivalent to the electron density) need take into account only those processes which involve that particular species. This results in considerable simplification of the diffusion equation, which may be written as (Banks and Kockarts, 1973 B. p. 170) as :

$$\frac{\partial n}{\partial t} = q - Ln - \frac{\partial \epsilon}{\partial z} \quad (3a)$$

$$\epsilon = nv = -D_a \sin^2 I \left[ \frac{\partial n}{\partial z} + \left( \frac{1}{T_p} \frac{\partial T_p}{\partial z} + \frac{1}{H_p} \right) n \right] \quad (3b)$$

with the following definitions :

$\epsilon = O^+$  flux in ions/cm<sup>2</sup>-s

$n = O^+$  concentration

$v = z$  component of ion (and electron) velocity

$q =$  production rate

$L =$  loss rate per  $O^+$  ion due to chemistry (loss by recombination, given by  $\alpha n^2$ , is negligible)

$T_p =$  plasma temperature (ion temperature + electron temperature)

$H_p =$  plasma scale height ( $kT_p/m_i g$ )

$D_a =$  ambipolar diffusion coefficient ( $kT_p/m_i \nu_{in}$ )

$\nu_{in} =$  ion neutral collision frequency

$I =$  magnetic dip angle, measured from horizontal and positive in the northern hemisphere

In writing Equation (3) we have neglected inertial terms, cross-field ion motion, and neutral winds.

When the expression for the flux (3b) is substituted into the continuity Equation (3a), the result is a linear parabolic partial differential equation:

$$\begin{aligned} \frac{\partial n}{\partial t} = & D_a \sin^2 I \frac{\partial^2 n}{\partial z^2} + D_a \sin^2 I \left[ \frac{1}{D_a} \frac{\partial D_a}{\partial z} + \frac{1}{H_p} + \frac{1}{T_p} \frac{\partial T_p}{\partial z} \right] \frac{\partial n}{\partial z} \\ & + \left\{ D_a \sin^2 I \left[ \frac{1}{D_a} \frac{\partial D_a}{\partial z} \left( \frac{1}{H_p} + \frac{1}{T_p} \frac{\partial T_p}{\partial z} \right) + \frac{\partial}{\partial z} \left( \frac{1}{H_p} + \frac{1}{T_p} \frac{\partial T_p}{\partial z} \right) \right] - L \ln \right. \\ & \left. + q \right\} \end{aligned} \quad (4)$$

In general the coefficients can depend on both altitude and time so that numerical methods must be used to obtain a solution. We are interested in the steady state solution which results from time independent coefficients. Nevertheless, the simplest method for obtaining the steady state solution is to choose a reasonable initial condition and then integrate Equation (4) until a steady state is reached. This has the additional advantage that the same computer code may be used for problems with time varying coefficients and boundary conditions.

To obtain the solution we must specify not only an initial condition, but also boundary conditions. The lower boundary is specified at  $z_0$  and is made low enough that chemical equilibrium prevails. The resulting boundary condition is

$$n(z_0) = q(z_0)/L(z_0) \quad (5)$$

The altitude,  $z_n$  refers to the upper boundary and must be chosen to be above the electron density peak but below the altitude at which  $H^+$  becomes the dominant

ion. Following Strobel and McElroy (1970) we have chosen the upper boundary condition to be

$$\phi(z_n) = - \int_{z_n}^{\infty} q(z) dz \sim - q(z_n) H_0(z_n) \quad (6)$$

where  $H_0(z_n)$  is the scale height of neutral oxygen at  $z_n$ . Using Equation (3b), the upper boundary condition takes the form

$$F(z_n) \left. \frac{\partial n}{\partial z} \right|_{z=z_n} + G(z_n) n(z_n) = \int_{z_n}^{\infty} q(z) dz \quad (7)$$

with  $F(z) = D_a \sin^2 I$  and  $G = D_a \sin^2 I \left( \frac{1}{T_p} \frac{\partial T_p}{\partial z} + \frac{1}{H_p} \right)$ .

To obtain an approximate numerical solution of Equation (4) we have adopted the Crank-Nicolson scheme proposed by Ames (1977, p. 67). First we re-write Equation (4) as

$$\frac{\partial n}{\partial t} = a(z) \frac{\partial^2 n}{\partial z^2} + b(z) \frac{\partial n}{\partial z} + c(z)n + q(z,t) \quad (8)$$

$$\text{where } a(z) = D_a \sin^2 I \quad (9a)$$

$$b(z) = a(z) \left[ \frac{1}{D_a} \frac{\partial D_a}{\partial z} + \frac{1}{H_p} + \frac{1}{T_p} \frac{\partial T_p}{\partial z} \right] \quad (9b)$$

$$c(z) = a(z) \left[ \frac{1}{D_a} \frac{\partial D_a}{\partial z} \left( \frac{1}{H_p} + \frac{1}{T_p} \frac{\partial T_p}{\partial z} \right) + \frac{\partial}{\partial z} \left( \frac{1}{H_p} + \frac{1}{T_p} \frac{\partial T_p}{\partial z} \right) \right] - L \quad (9c)$$

and we have assumed that  $a, b$ , and  $c$  are independent of time. We choose an altitude grid of  $n + 1$  points numbered from zero at the lower boundary,  $z_0$ , to  $n$  at the upper boundary,  $z_n$ . The grid spacing is uniform and given by  $\Delta z = (z_n - z_0)/n$ . The time step is chosen to be  $\Delta t$  and the following notation is adopted:

$$z_i = z_0 + i\Delta z$$

$$t_j = j\Delta t$$

$$n_{ij} = n(z_i, t_j)$$

$$\delta_x n_{ij} = n_{i+1/2,j} - n_{i-1/2,j}$$

$$u_x n_{ij} = \frac{1}{2} (n_{i+1/2,j} + n_{i-1/2,j})$$

The discrete version of (8) is (for  $0 < i < n$ )

$$\begin{aligned} \frac{1}{\Delta t} (n_{i,j+1} - n_{ij}) = & \frac{1}{2\Delta z^2} (a_i \delta_x^2 + \Delta z b_i u_x \delta_x + \Delta z^2 c_i) (n_{i,j+1} + n_{ij}) \\ & + \frac{1}{2} (q_{i,j+1} + q_{ij}) \end{aligned} \quad (10)$$

For  $i = 0$ , the equation is

$$n_{0,j+1} = \frac{q_{0,j+1}}{L_{0,j+1}} \quad (11)$$

where  $L_{0,j} = L(z_0, t_j)$  is the chemical loss term. For  $i = n$ , the equation is the same as Equation (10) except that we must replace quantities evaluated at

$i = n + 1$  using the boundary condition (7):

$$n_{n+1,j} = n_{n-1,j} - \frac{G_n}{F_n} n_{n,j} + \frac{Q_n}{F_n} \quad (12)$$

where  $F_n = F(z_n)$ ,  $G_n = G(z_n)$  and  $Q_n = \int_{z_n}^{\infty} q(z) dz$

When the indicated operations and substitutions are carried out and the unknown quantities ( $n_{i-1,j+1}$ ,  $n_{i,j+1}$ ,  $n_{i+1,j+1}$ ) are isolated on the left side, Equations (10 - 12) may be written in matrix form as

$$\underline{A} \underline{n}_{j+1} = \underline{B} \underline{n}_j + \underline{r}_j \quad (13)$$

where  $\underline{n}_j$  is a vector whose components are the values of the density at each point of the altitude grid at time  $t_j$ . The matrices A and B are tridiagonal matrices whose non-zero components are

$$\underline{i} = 1: \quad e_1^{(0)} = \frac{a_1}{\Delta z^2} - \frac{c_1}{2}$$

$$d_1 = - \left( \frac{a_1}{2\Delta z^2} - \frac{b_1}{4\Delta z} \right)$$

$$A_{11} = e_1 = \frac{1}{\Delta t} + e_1^{(0)}$$

$$B_{11} \frac{1}{\Delta t} - e_1^{(0)}$$

$$A_{12} = f_1 = - \left( \frac{a_1}{2\Delta z^2} + \frac{b_1}{4\Delta z} \right)$$

$$B_{12} = - f_1$$

$$\underline{2 \leq i \leq n-1}: \quad e_i^{(0)} = \frac{a_i}{\Delta z^2} - \frac{c_i}{2}$$

$$A_{i,i,-1} = d_i = - \left( \frac{a_i}{2\Delta z^2} - \frac{b_i}{4\Delta z} \right)$$

$$B_{i,i-1} = -d_i$$

$$A_{ii} = e_i = \frac{1}{\Delta t} + e_i^{(0)}$$

$$B_{ii} = \frac{1}{\Delta t} - e_i^{(0)}$$

$$A_{i,i+1} = f_i = - \left( \frac{a_i}{2\Delta z^2} + \frac{b_i}{4\Delta z} \right)$$

$$B_{i,i+1} = -f_i$$

$$\underline{i = n}: \quad e_n^{(0)} = \frac{a_n}{\Delta z^2} - \frac{c_n}{2}$$

$$e_n^{(1)} = \frac{1}{F_n} \left( \frac{a_n}{\Delta z} + \frac{b_n}{2} \right)$$

$$A_{n,n-1} = d_n = - \frac{a_n}{\Delta z^2}$$

$$B_{n,n-1} = -d_n$$

$$A_{nn} = e_n = \frac{1}{\Delta t} + e_n^{(0)} + G_n e_n^{(1)}$$

$$B_{nn} = \frac{1}{\Delta t} - (e_n^{(0)} + G_n e_n^{(1)})$$

The vector  $r_j$ , closely related to  $q(z,t)$  is

$$r_{1j} = q_{1j} - 2d_1 n_0$$

$$r_{id} = q_{ij}$$

$$r_{nj} = q_{nj} + 2e_n^{(1)} Q_n$$

The solution of Equation (13) is simplest when  $\underline{A}$  is positive definite, or at least diagonally dominant and irreducible. Irreducibility is assured if  $A_{i,i+1} = f_i \neq 0$  for  $i = 1, 2, 3, \dots, n-1$ . Diagonal dominance requires  $|A_{i,i}| > |A_{i,i-1}| + |A_{i,i+1}|$  for all  $i$ . This condition can be met by requiring

$$\Delta z < \min_i \left( \frac{2a_i}{b_i} \right)$$

$$\Delta t < \frac{2}{\max_i (c_i)}$$

In the auroral ionosphere, neither condition is very restrictive:  $\Delta z \leq 25$  km and  $\Delta t \leq 40$  sec are generally sufficient. Of course, stability and convergence considerations place further restrictions on  $\Delta z$  and  $\Delta t$ .

With  $\Delta z$  and  $\Delta t$  chosen so that the matrix  $A$  is diagonally dominant, Equation (13) may be solved using Gaussian elimination without pivoting. Furthermore, when the coefficients  $a, b$ , and  $c$  are independent of time,  $\underline{A}$  can be factored once at the beginning and the resulting decomposition used at each time step. A computer code incorporating these features has been written and tested and has been integrated into the existing chemistry code. Preliminary results indicate that it increases the execution time of the chemistry code by only a small amount. An example of the results is shown in Figure 5. Although chemical equilibrium is established quickly in the E-region, diffusive equilibrium is reached only after several hours. Application of this computer code to the daytime ionosphere is described in Section 8.5.

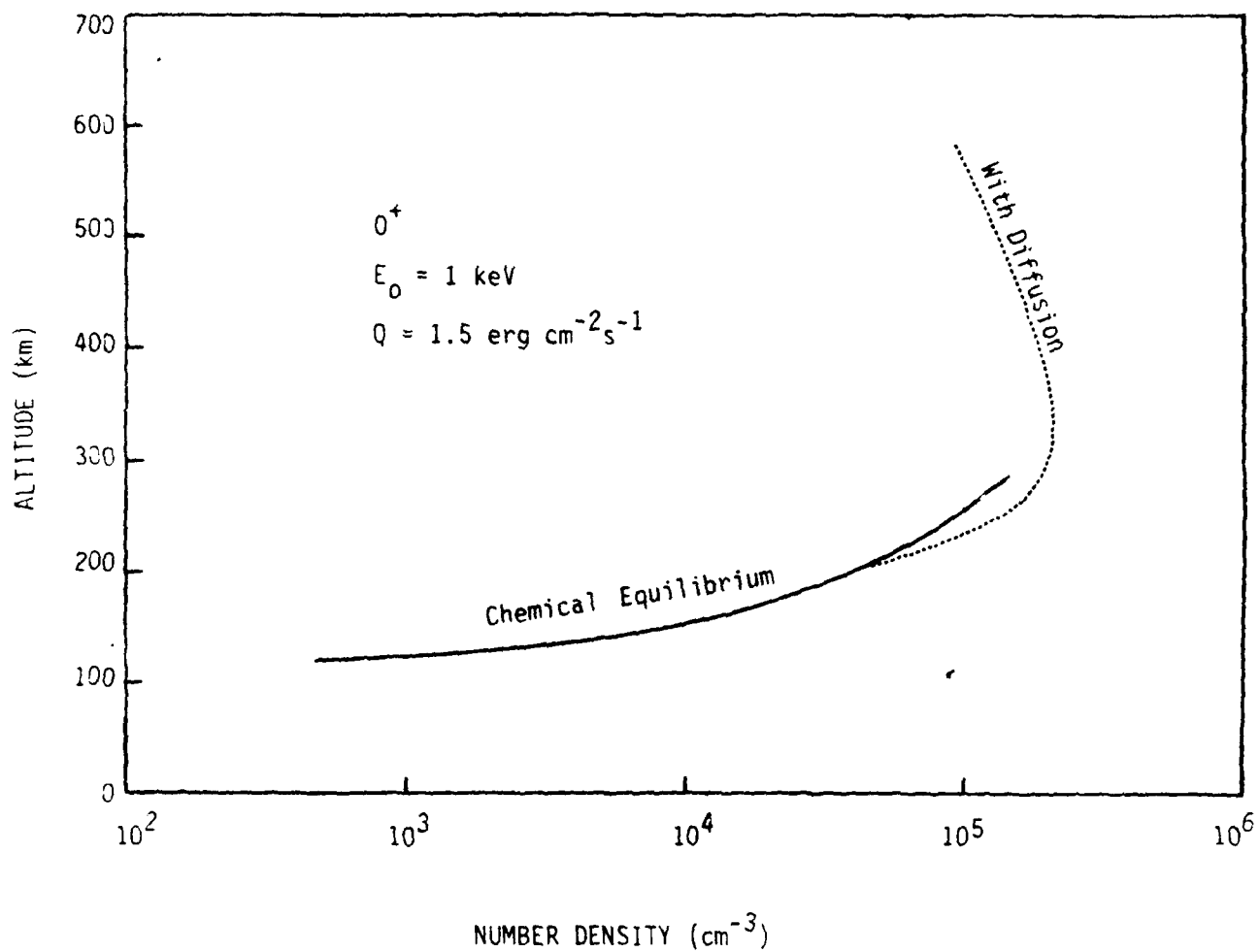


Figure 5. An Example of the Results of the Diffusion Calculation Using the Jacchia (1977) Model Atmosphere and a Maxwellian Distribution for the Incident Electrons. Note That Diffusion Causes Noticeable Departures From Chemical Equilibrium as low as 200 km.

## Section 6

### The Effect of Rayleigh Scattering on Nadir Observed UV Intensities From Satellites

#### 6.1 General Comments

We wish to address the problem of possible contamination of ionospherically produced UV intensities due to the backscattering of either solar or auroral produced radiation by Rayleigh scattering. Viewing is to be downward (not necessarily true nadir) from satellite altitudes. The wavelength region to be addressed is 2000 to 4000 Å. Below  $\sim 2000$  Å, there is no problem caused by Rayleigh scattering due to the strength of pure absorption by  $O_2$ . Longward of 3000 Å, Rayleigh scattering is not the only possible source of contamination. Scattering from clouds, aerosols, and the earth's surface become possible. Here, we shall restrict ourselves to Rayleigh scattering but must keep in mind these other mechanisms when dealing with features such as  $N_2^+$  3914 Å.

We shall see that there can be serious contamination from back-scattered solar radiation. The key to this problem is both the strength of the solar flux and the width of the instrumental bandpass. Let us consider, for example, a spectrometer with a resolution of  $\sim 1$  Å. The width of the emission feature to be measured will be a small fraction of 1 Å. Backscattered solar radiation mixed with this intensity, on the other hand, will cover the entire bandpass width. This will place more severe restrictions on observable wavelength regions for daytime conditions in contrast to nighttime (auroral included) conditions where the contaminated intensity has the same line shape characteristics as the intensity of interest.

D.E. Anderson Jr. of the Naval Research Laboratory kindly provided some of his time to help us begin this analysis. He also has provided the computer generated plots to follow. The multiple scattering effects to be discussed are based on information in two of these plots.

## 6.2 Basic Expressions

The quantity of interest is the intensity  $I$  in units of photons (ph)/cm<sup>2</sup>-s-sr-A for a wavelength distributed source or ph/cm<sup>2</sup>-s-sr for a discrete source. The equation for  $I$  is

$$I(\mu) = I_I(\mu) + I_R(\mu) \quad (14)$$

where  $\mu$  is the direction cosine relative to the downward vertical direction (here, we are interested in  $\mu > 0$ ),  $I_I$  is the intensity component due to direct emission from the ionosphere, and  $I_R$  is the intensity component from below the ionosphere due to Rayleigh scattering. In the discussion to follow, we assume a plane-parallel geometry and isotropic scattering (justified in this subsection). Then, either component has the following integral form:

$$I(\mu) = \int \frac{S(\tau)}{4\pi} T(\tau/\mu) d\tau/\mu \quad (15)$$

where  $\tau$  is the optical depth for self absorption,  $S(\tau)$  is the source function in units of ph/cm<sup>2</sup>-unit depth  $\tau$  - s, and  $T$  is a transmission function accounting for self and pure absorption. For a continuum source, the unit A<sup>-1</sup> must be added to the units of  $S$ . The optical depth in differential form, is

$$d\tau = \sigma ndz \quad (16)$$

where  $\sigma$  is the self-absorption cross section in cm<sup>2</sup> and  $n$  is the density of the self-absorbers.

The source function  $S(\cdot)$  is related to the total volume emission rate by

$$S(\cdot) = S(z)/n \quad (17)$$

where the rate  $S(z)$  has units of  $\text{ph/cm}^3\text{-s}$ . We choose to use  $S$  for either the source function or total volume emission rate and let the argument distinguish between them. We introduce  $S(z)$  since it is the quantity to use if one is dealing with an optically thin emission. We will be considering wavelengths which apply to both optically thick and thin media. Equations (16) and (17) allow us to express Equation (15) in its alternate form, namely

$$I(\nu) = \int \frac{S(z) T(z, \nu)}{4\pi} dz/\nu \quad (18)$$

where we have followed the same convention with  $T$  as with  $S$ , namely, in using  $z$  and  $\tau$  as arguments of the same function. Equation (18) is still general, in that it applies to either optically thick or thin media. For the latter case, it becomes

$$I(\nu) = \int \frac{S_0(z) e^{-\tau/\nu}}{4\pi} dz/\nu \quad (19)$$

where  $S_0(z)$  is the single scattering or initial volume emission rate and  $\tau$  is the optical depth for pure absorption which may or may not be zero.

Similar to  $S$ ,  $S_0$  is expressed as a function of either  $\tau$  or  $z$ . The relationship is that given in Equation (17). There are several possible mechanisms for producing  $S_0$ . Those of interest to us in the ionosphere are

- 1) auroral electron impact excitation
  - 2) photoelectron impact excitation
- and
- 3) direct excitation by solar photons.

Those of interest to us below the ionosphere are the Rayleigh scattering of

- 1) auroral produced radiation
- and
- 2) solar radiation.

Another mechanism, excitation by chemical reactions, is not of interest here.

If the medium is optically thick, then  $S$  will be greater than  $S_0$ . This is due to radiation imprisonment caused by the multiple scattering of the photons of interest. In this case, the relationship between  $S$  and  $S_0$  may be expressed through the integral equation of radiative transfer. It is

$$S(\tau) = S_0(\tau) + \int S(\tau') H(|\tau - \tau'|) d\tau' \quad (20)$$

where  $H$  is a kernel giving the probability of photons emitted at  $\tau'$  reaching level  $\tau$  and being scattered there. Detailed discussions of properties of this equation for resonance line radiations are given by Strickland and Donahue (1970) and Strickland and Rees (1974). Anderson and Meier (1979) have applied this equation to the problem of Rayleigh scattering. They observed that adequate solutions to Equation (20) as well as Equation (14) can be obtained assuming isotropic scattering in place of the more complicated scattering given by the Rayleigh phase function. This was determined by making comparisons with 'exact' solutions obtained by the Monte Carlo method. Later we will show examples of  $S$  obtained by Anderson for daytime conditions over the wavelength range from 2000 to 4500 Å.

### 6.3 Derivation of the Intensity Equation

It is instructive to relate Equation (14) to what is actually observed by a detector. Consider the detector to be situated at satellite altitudes viewing the ionosphere and lower atmosphere at some angle  $\mu$  ( $\cos^{-1} \mu$ ) relative to the downward vertical direction. Figure 6 depicts the observing conditions. Let  $\delta N$  be the rate of photons received from the volume element  $\delta V$ . It is

$$\delta N = S(z) T(z, \mu) \delta V \frac{\omega}{4\pi} \quad (21)$$

where  $\omega$  is the solid angle for emission which enters the detector.  $S$  is assumed to have an isotropic behavior which leads to the presence of  $1/4\pi$ . We wish to integrate  $\delta N$  over  $A_E$  since this is the actual observing cross sectional area at distance  $R$ . We assume  $S$  to be constant over  $A_E$ . Letting  $\delta N'$  refer to the integrated quantity, it is

$$\delta N' = S(z) T(z, \mu) A_E \delta s \frac{\omega}{4\pi} \quad (22)$$

We now wish to modify  $\delta N'$  to remove its dependence on any particular detector. To do so, we divide  $\delta N'$  by  $A_d \Omega_d$  where  $A_d$  is the area of the detector and  $\Omega_d$  is the detector's solid angle field of view. Since the modified  $\delta N'$  has the units of an incremental intensity, let it be denoted by  $\delta I$ . It is

$$\delta I = \frac{S(z)}{4\pi} \frac{A_E}{A_d \Omega_d} T(z, \mu) \delta s \quad (23)$$

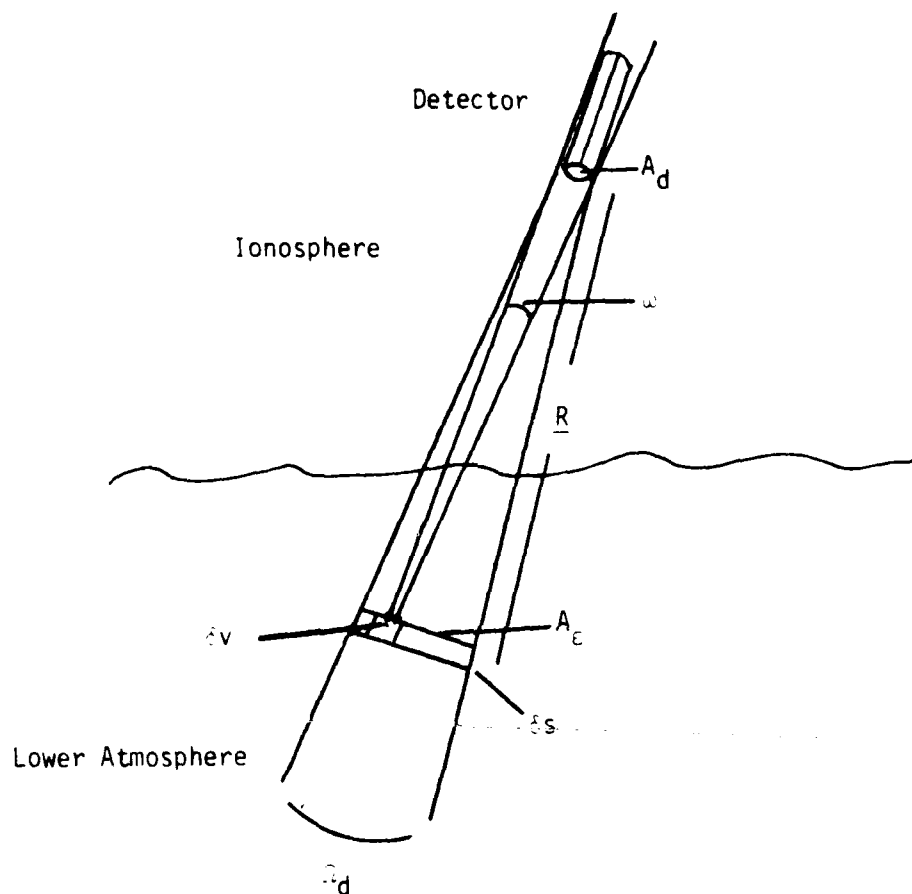


Figure 6 Satellite Nadir Viewing Geometry.

The quantity  $\mu/d A_c/A_d$  is unity as can be seen by noting that  $\mu = A_d/R^2$  and  $d = A_c/R^2$ . Replacing  $ds$  by  $dz/\mu$ , Equation (23) becomes

$$\delta I = \frac{S(z)}{4\pi} T(z, \mu) dz/\mu \quad (24)$$

which can be equivalently expressed as

$$\delta I = \frac{S(\tau)}{4\pi} T(\tau/\mu) d\tau/\mu \quad (25)$$

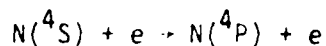
Integration of  $\delta I$  gives  $I$  as shown in Equation (15).

#### 6.4 Forms of $S_0$

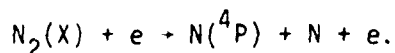
Expressions will follow for the initial volume emission rate  $S_0(z)$ . In the ionosphere, we are here interested in excited state production by electron impact. Let us introduce  $P$ , the volume excitation rate which equals  $S_0(z)$  only if quenching is unimportant. The expression for  $P$  due to electron impact excitation is

$$P_{\ell k}(z) = \sum_{\ell'} n_{\ell'}(z) \int \sigma_{\ell', k}(E) \Phi(z, E) dE \quad (26)$$

with units of excitations/cm<sup>3</sup>-s. The sum is over species and applies to certain atomic states such as N(<sup>4</sup>P) which can be produced by either



or



States of interest to us will be effectively produced by electron impact on a single type of neutral particle. The terms  $\sigma_{\ell,k}$  and  $\phi$  in Equation (26) are the electron impact cross section and spherical flux for either auroral or photoelectrons. The index  $k$  refers to the particular state which may be an atomic state, an electronic state of a molecule, or a vibrational state of a molecule.

Let us now relate  $S_0$  to  $P_{\ell k}$  and in the process we shall delete the  $\ell k$  indices. For an atomic state unaffected by quenching,

$$S_0(z) = P(z). \quad (27)$$

With quenching, the relationship is

$$S_0(z) = \frac{A P(z)}{A_T + \sum_i q_i n_i(z)} \quad (28)$$

where  $A$  is the transition rate ( $s^{-1}$ ) for the emission of interest,  $A_T$  is the total rate from the upper state, and  $q_i$  is the quenching coefficient ( $cm^3-s^{-1}$ ) for the  $i^{th}$  species.

For molecules, we are interested in emission within a band. Let us assume  $P$  refers to the excitation rate for a particular  $v'$  level of the excited electronic state. Excitation may be a combination of direct excitation from the ground state and cascading. In the case of the  $A^3\Sigma$  state of  $N_2$ , cascading is the dominant excitation mechanism (see Cartwright, 1978). In the absence of quenching,  $S_0$  is related to  $P_v$  by

$$S_0(z) = \frac{A_{v',v''}}{\sum_{v''} A_{v',v''}} P_{v'}(z) \quad (29)$$

where  $A_{v',v''}$  is the transition rate from level  $v'$  of the upper state to level  $v''$  of the lower state. With quenching, the relationship is

$$S_0(z) = \frac{A_{v',v''} P_{v'}}{\sum_{v''} A_{v',v''} + \sum_i q_i n_i(z)} \quad (30)$$

similar to Equation (28) for atomic emission.

For Rayleigh scattering, we are interested in two different expressions for  $S_0$  - one for the unidirectional solar source and the other for diffuse auroral emissions. For the solar case,  $S_0$  has the form

$$S_0(z) = \pi F_0(\lambda) e^{-(\tau_R + t)/\mu_s} n \sigma_R \quad (31)$$

where  $\pi F_0$  is the unattenuated solar flux at some given wavelength  $\lambda$  in photons/cm<sup>2</sup>-s-A,  $n$  is the total neutral scattering density, and  $\sigma_R$  is the Rayleigh cross section. By normalizing  $S_0$  to a unit solar flux,  $S_0(\tau)$  is simply

$$S_0(\tau_R) = e^{-(\tau_R + t)/\mu_s} \quad (32)$$

which is a convenient form for comparisons of  $S_0$  and  $S$  from one wavelength to another.

The form of  $S_0(z)$  for an auroral radiation source is

$$S_0(z) = n\sigma_R \int I(\underline{\Omega}) e^{-(\tau_R + t)/\mu} d\underline{\Omega} \quad (33)$$

where  $I$  is the auroral intensity for some feature of interest as it leaves the ionosphere in the downward direction given by  $\underline{\Omega}$ . Here,  $z$ , as in Equation (31), refers to altitudes in the lower atmosphere. We may think of the integration region in Equation (33) as being over  $2\pi$  with  $I(\underline{\Omega})$  properly set to zero for directions from which no auroral luminosity is emitted. In reality, there can be a variety of directional luminosity distributions from those giving limited ranges such as for a single arc to more hemispherical distributions as can be found under weak, diffuse conditions.

## 6.5 Parameter Values

The basic parameters, already introduced, are

- 1)  $\sigma_R(\lambda)$ , the Rayleigh cross section in  $\text{cm}^2$
- 2)  $\tau_R(\lambda)$ , the corresponding optical depth
- 3)  $\sigma_p(\lambda)$ , the pure absorption cross section

and

- 4)  $t_p(\lambda)$ , the corresponding optical depth
- 5)  $\pi F_0(\lambda)$ , the unattenuated solar flux in  $\text{photons/cm}^2\text{-s-A}$ .

For  $\sigma_R$ , we use the expression

$$\sigma_R(\lambda) = \frac{3.9 \times 10^{-28}}{\lambda^\alpha} \quad \text{cm}^2 \quad (34)$$

with  $\alpha$  given by

$$\alpha = 3.916 + .074 \lambda + \frac{.05}{\lambda} \quad (35)$$

(Frolich and Scaw, 1980). The units of  $\lambda$  are  $10^{-4}$  A. Figure 7 displays  $\tau_R$  between 1800 and 3200 A.

Pure absorption is caused by  $O_2$  and  $O_3$  over the wavelength range of interest. For  $O_2$ ,  $\tau_p$  is shown in Figure 8 from 1700 to  $\sim 2600$  A, taken from data gathered by Sullivan and Holland (1966). The region shown below 2000 A is dominated by Schumann-Runge band absorption. Above 2000 A, absorption is associated with the Herzberg continuum. Figure 9 shows  $\tau_p$  for  $O_3$  between 2000 and 3000 A, again taken from Sullivan and Holland (1966). The dominant absorption in this region is Hartley continuum absorption.

The depths  $\tau_R$  and  $t_p$  at  $z = 0$  km are shown in Figure 10. Altitude profiles at selected wavelengths appear in Figure 11. We note from Figure 10 that  $t$  becomes small as well as less than  $\tau_R$  longward of  $\sim 3000$  A. As will be seen, this leads to a noticeable increase in Rayleigh scattering longward of this wavelength.

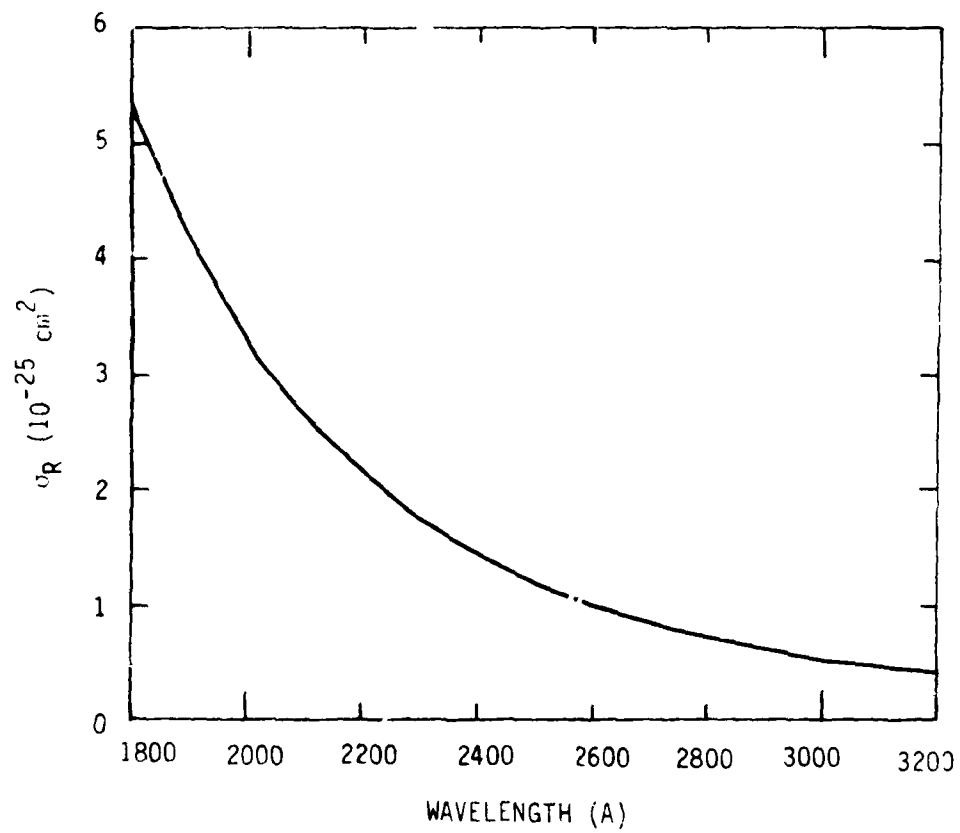


Figure 7 Rayleigh Scattering Cross Section.

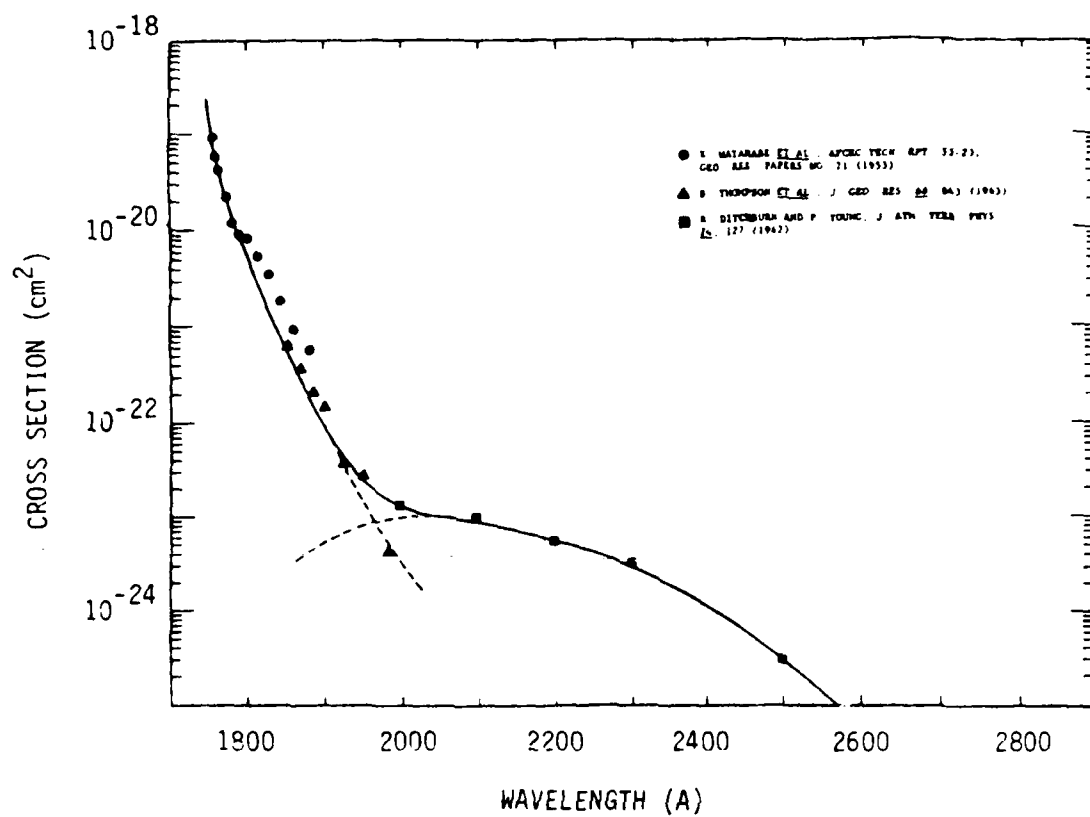


Figure 8 O<sub>2</sub> Absorption Cross Section Taken From Sullivan and Holland (1966).

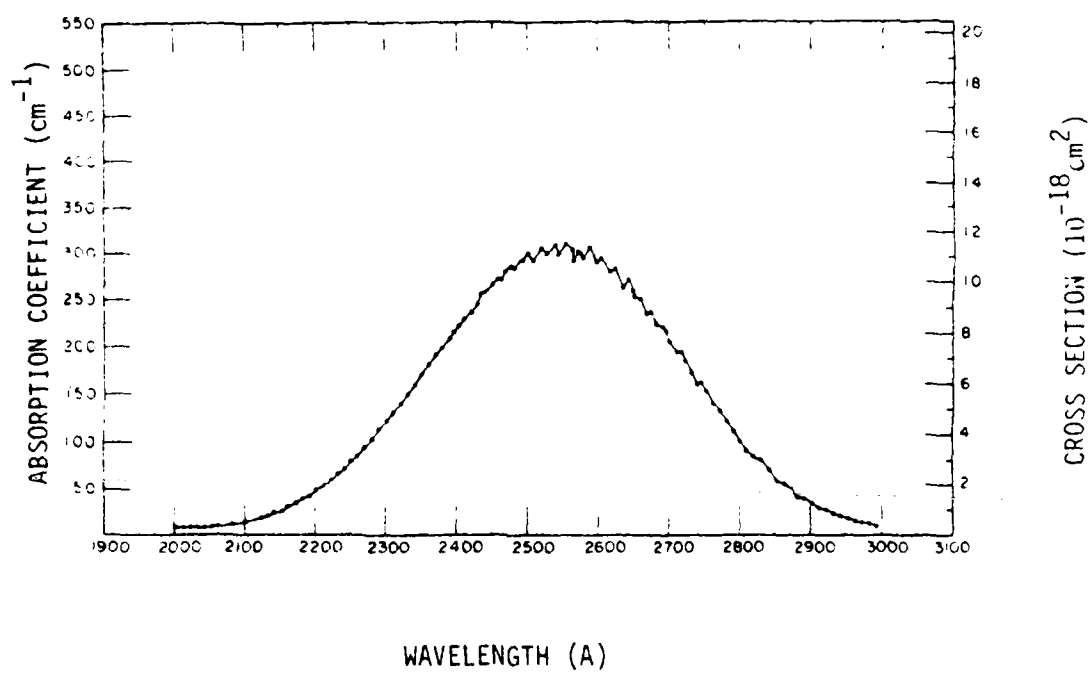


Figure 9 O<sub>3</sub> Absorption Cross Section Taken From Sullivan and Holland (1966).

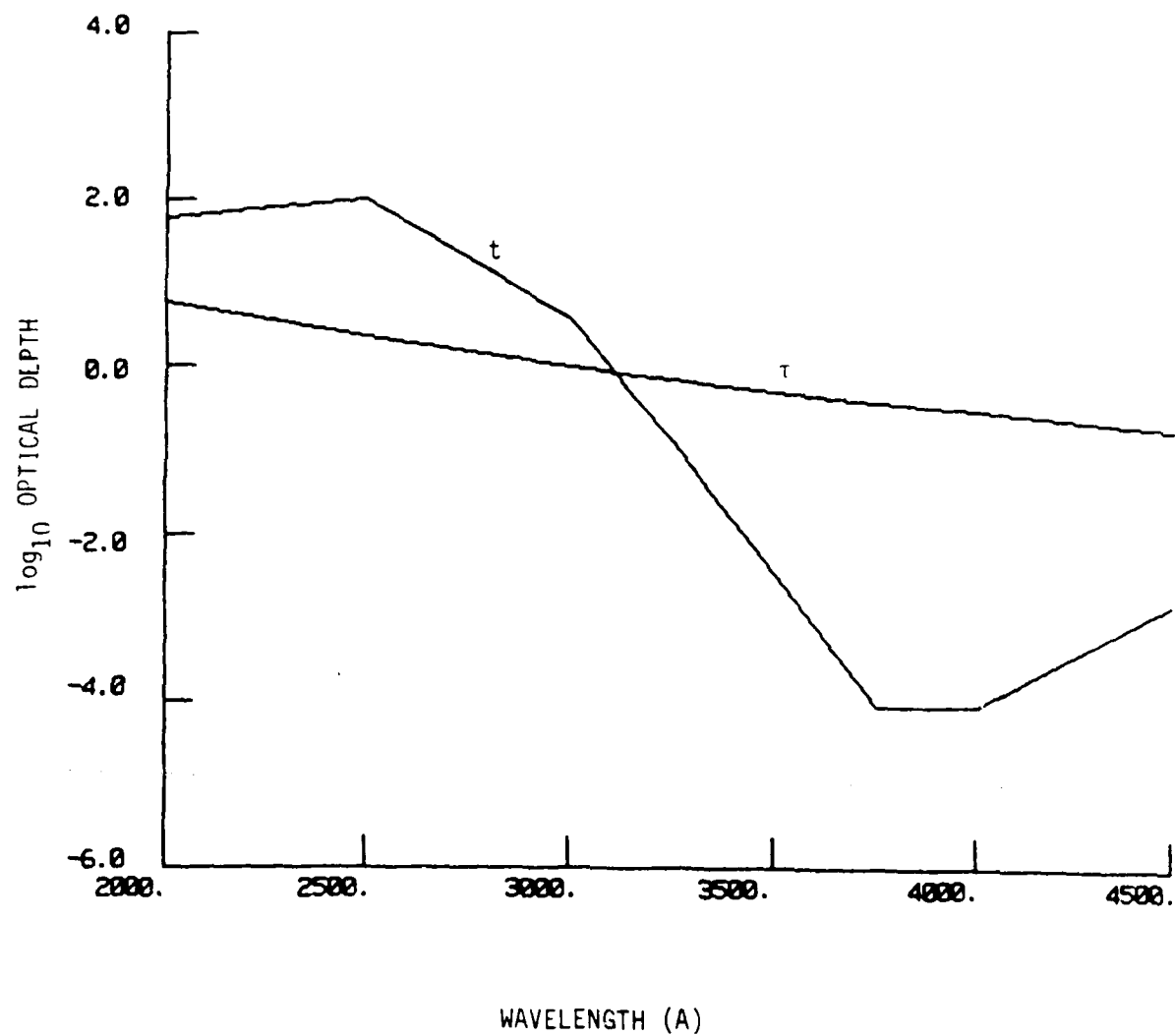


Figure 10 Rayleigh Scattering Optical Depth  $\tau$  and Pure Absorption Optical Depth  $t$  at  $z=0$  km. Absorption is by  $O_2$  and  $O_3$

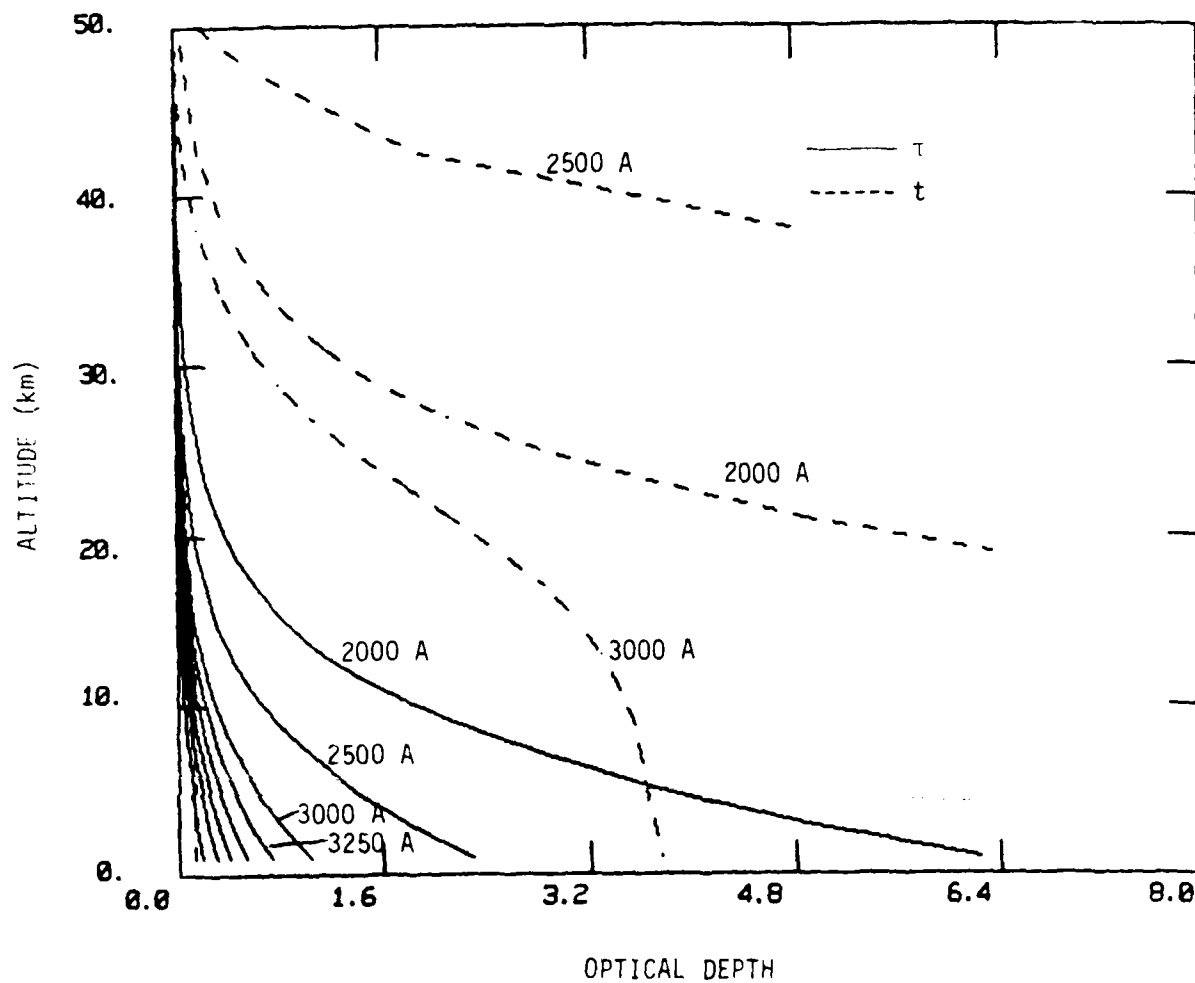


Figure 11 Optical Depths  $\tau$  and  $t$  Versus Altitude at Selected Wavelengths.

An example of a solar spectrum is shown in Figure 12 from 1800 Å to 3200 Å, (Banks and Kockarts, 1973A). The only point we wish to make here is that even weak Rayleigh scattering at wavelengths such as 3000 Å can swamp ionospherically produced intensities as observed from satellite altitudes in the daytime due to the strength of the solar flux. More quantitative information will follow in the next subsection.

## 6.6 Results

We begin by showing the effect of multiple scattering over the wavelength range 2000 - 4500 Å. This is done in Figures 13 and 14 which show  $S_0(\tau)$  and  $S(\tau)$  at altitudes of 96 and 47 km (D.E. Anderson, private communication).  $S(\tau)$  was obtained from Equation (20) with  $S_0(\tau)$  given by Equation (32).  $S_0$  thus refers to the initial scattering of solar radiation (with  $\pi F_0$  set to unity). A similar  $\tau$  dependence is exhibited, however, for the initial Rayleigh scattering of auroral radiation and thus this discussion applies to either situation. By comparing  $S$  to  $S_0$  within either Figure 13 or 14, we see that multiple scattering only becomes important above 3000 Å. Below this wavelength, pure absorption is strong enough by  $O_2$  and  $O_3$  to prevent radiation from effectively penetrating to altitudes where the condition  $\tau \gg 1$  is met.

We now present results for the backscatter of solar radiation. We use Equation (15) to calculate  $4\pi I$ , the apparent column emission rate. The  $T$  function is just  $e^{-(\tau+t)/u}$ . Then, setting  $S$  to  $S_0$  as given by Equation (32),  $4\pi I$  is

$$4\pi I_R(u, \mu_s) = \pi F_0 f_s \quad \text{ph/cm}^2\text{-s-A} \quad (36)$$

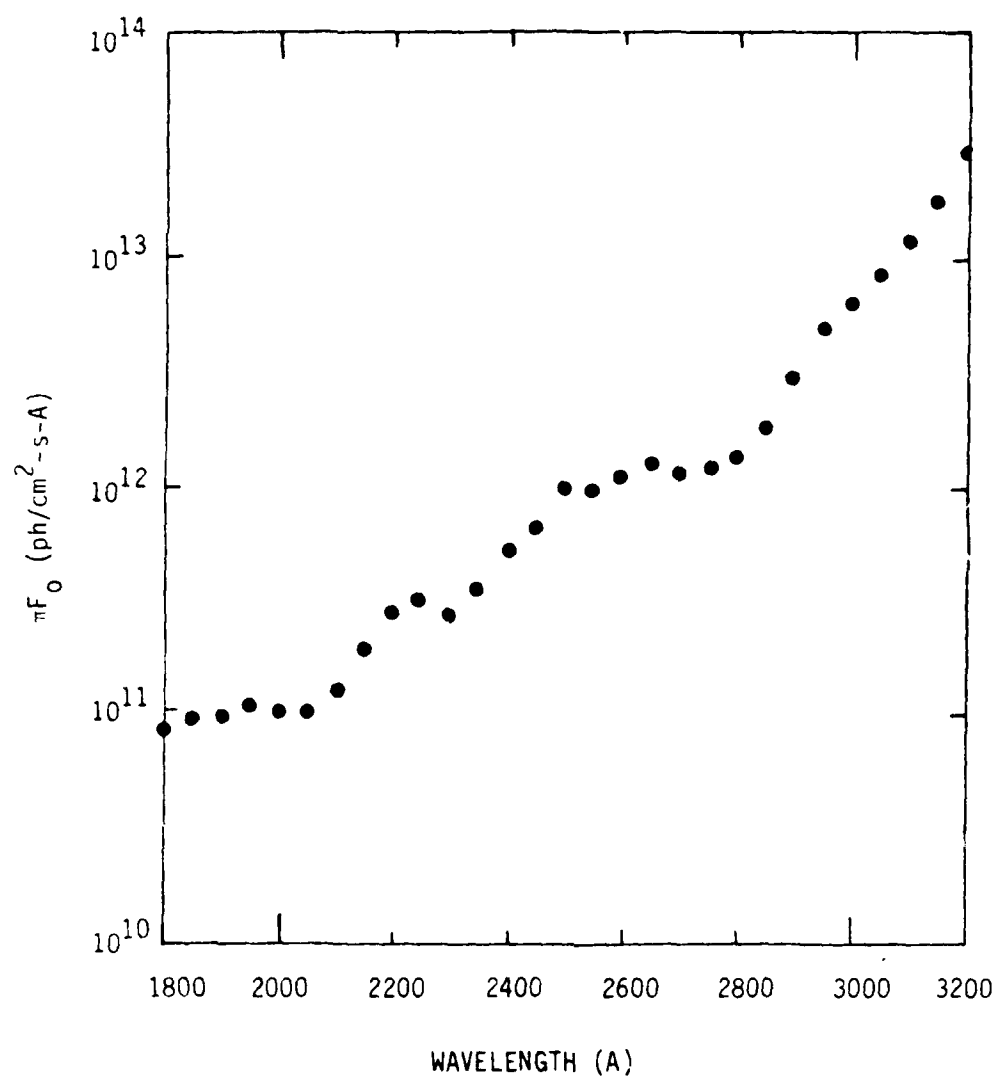


Figure 12 Solar Flux Based on Tabulation Appearing in Banks and Kockarts (1973 A).

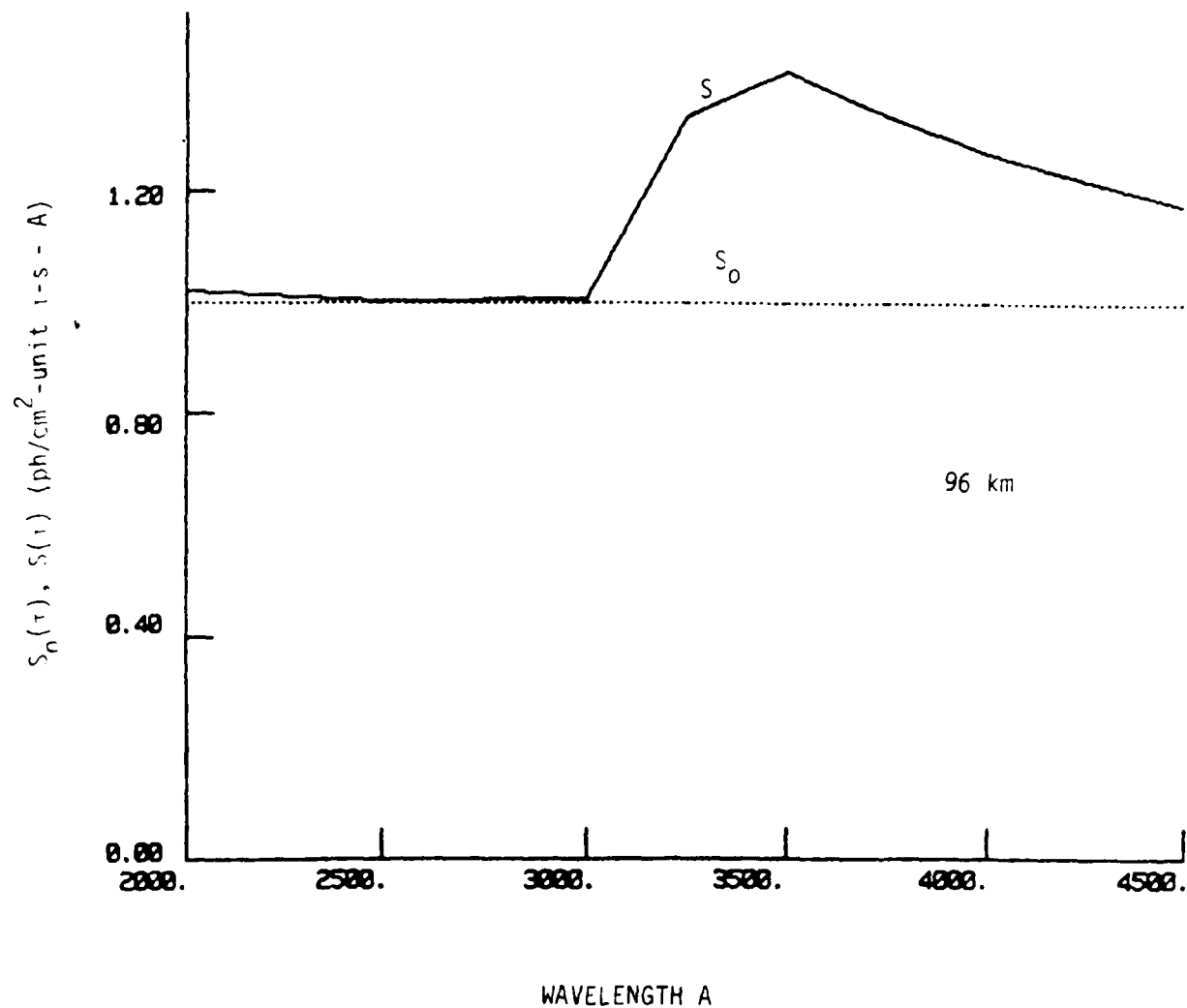


Figure 13 Rayleigh Scattering Source Functions at 96 km for Solar Flux  $\pi F_0$  Normalized to Unity at Each Wavelength.

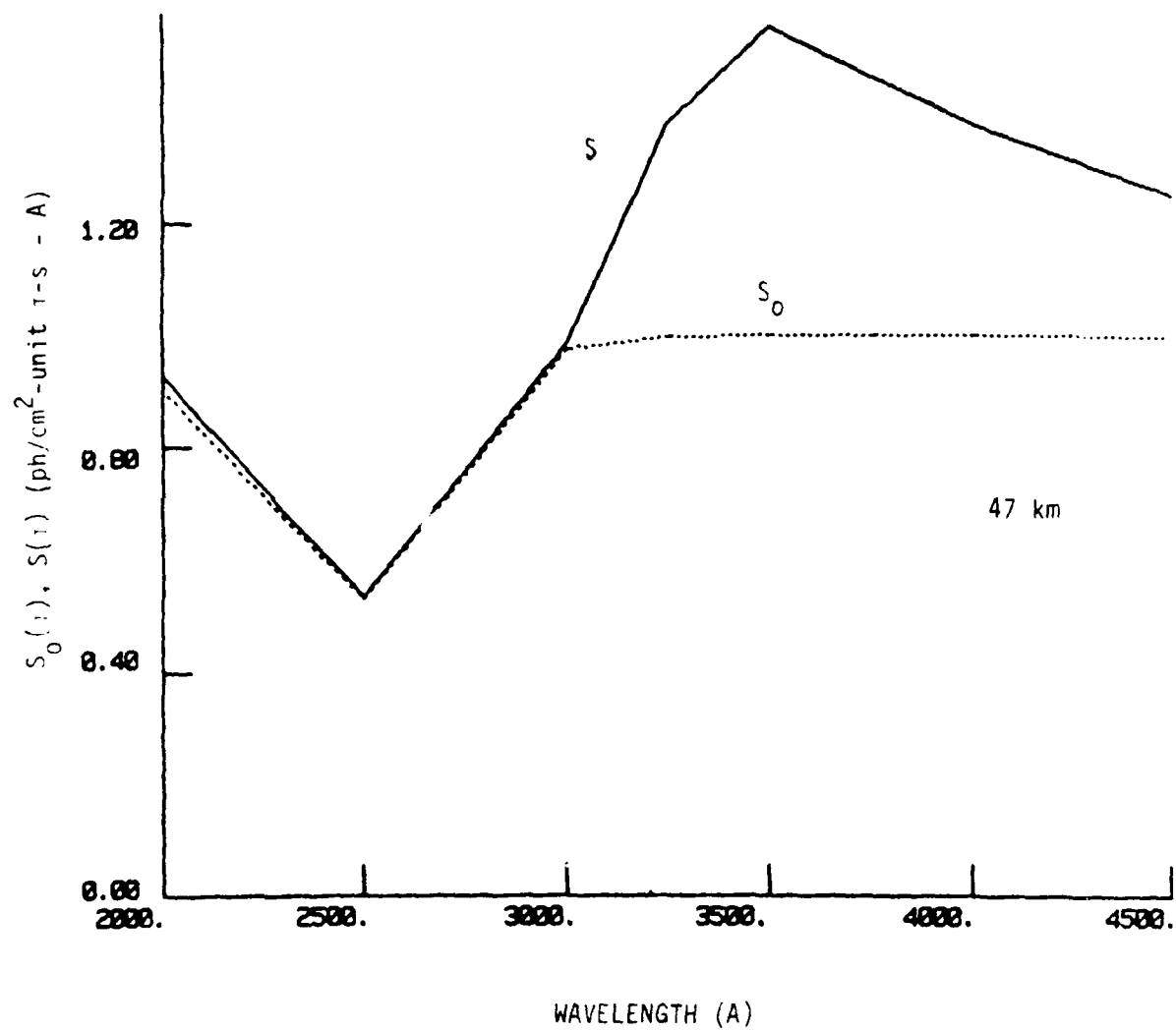


Figure 14 Similar to Figure 13 Except at 47 km.

with  $f_s$  given by

$$f_s = \int_0^{\tau_0} e^{-(\mu + \mu_s) \int_0^{\tau} S(t) dt} d\tau \quad (37)$$

Note that the Rayleigh phase function does not appear because of the isotropic scattering approximation justified earlier in this discussion.

Figure 15 shows  $f_s$  and  $4\pi I_R$  as functions of wavelength from 1400 to 3200 Å. For these results,  $\mu = \mu_s = 1$ . The peak in  $f_s$  at 2000 Å is due to a minimum in the combined pure absorption by  $O_2$  and  $O_3$ . It should be noted that structure in  $f_s$  will be present below 2000 Å due to structure in Schumann-Runge band absorption which is responsible for the exhibited decrease. The decrease in  $f_s$  longward of 2000 Å is caused by  $O_3$  absorption. The dramatic rise near 3000 Å results from this absorption decreasing to the point that radiation can penetrate deeply into the atmosphere. We have included multiple scattering effects above 3000 Å in an approximate way. This has been done by scaling  $4\pi I$  as calculated in Equation (36) by  $S(\tau)/S_0(\tau)$  with  $\tau$  given near its mid-point value.

The profile for  $4\pi I_R$  was obtained using  $\pi F_0$  from Figure 12. We observe that more than a kilo-Rayleigh per Angstrom is backscattered above 1900 Å. Thus, satellite observations must be restricted to wavelengths shorter than this since ionospherically produced emission features above 1900 Å will be swamped by the given Rayleigh intensity component.

Our last results are for the Rayleigh component of auroral observed intensities. As we shall see, the observational restrictions with regard to wavelength are less severe here since there is no strong external radiation source as there is in the daytime. Again we replace  $S$  by  $S_0$  with  $S_0$  here given by Equation (33). To obtain an upper limit to  $S_0$ , we assume the auroral luminosity  $I(\Omega)$  to be uniform and independent of  $\Omega$  across the sky. Then Equation (33) becomes

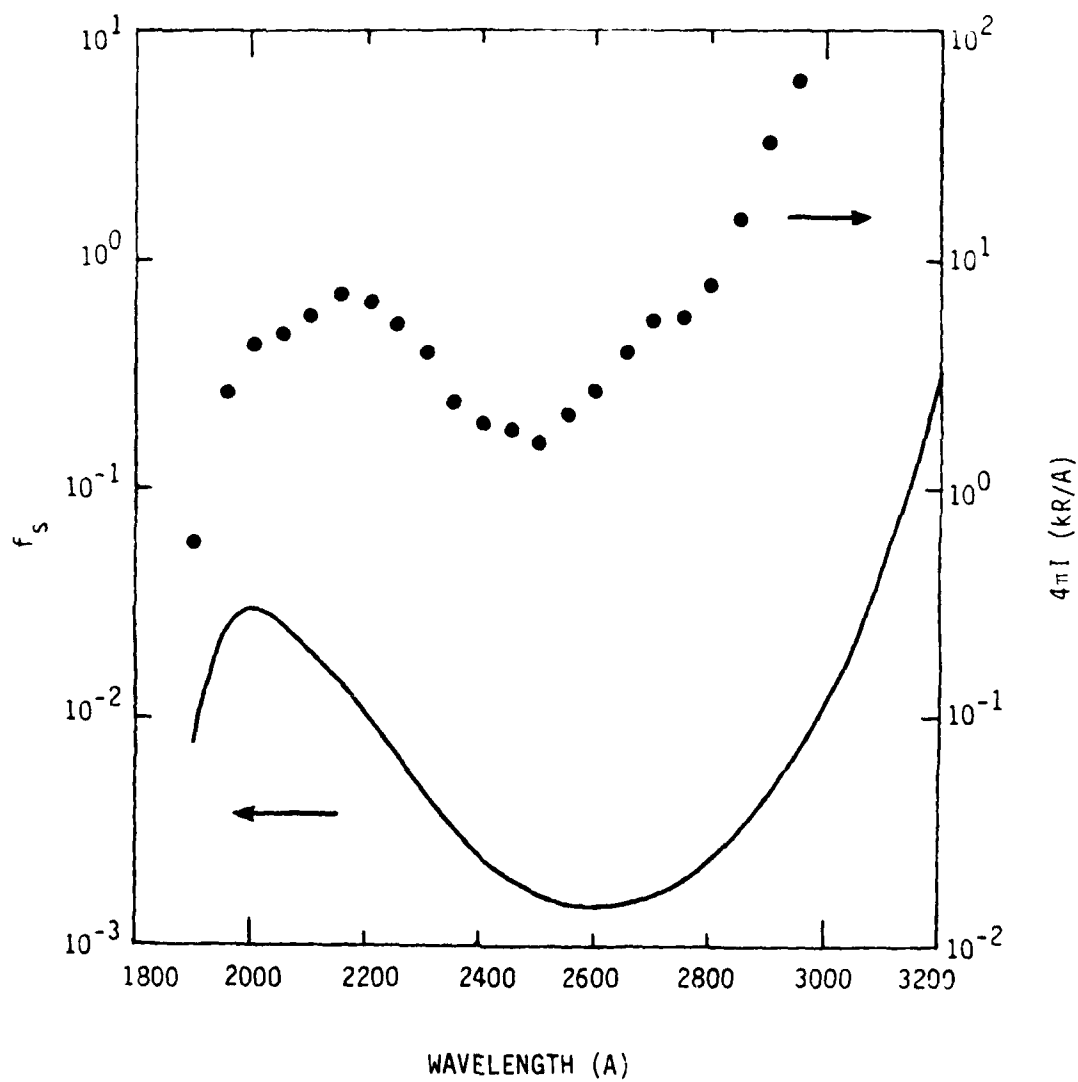


Figure 15 Functions  $f_s$  and  $4\pi I$  for Rayleigh Backscattering of Solar Radiation

$$S_0(\tau) = 2\pi I_I E_2(\tau + t) \quad (38)$$

where  $E_2$  is the second exponential integral. Inserting this into Equation (15),  $4\pi I_R$  becomes

$$4\pi I_R(\mu) = 4\pi I_I f_A \quad \text{ph/cm}^2\text{-s} \quad (39)$$

with  $f_A$  given by

$$f_A = \frac{1}{2} \int_0^{\tau_0} E_2(\tau + t) e^{-(\tau + t)/\mu} d\tau/\mu \quad (40)$$

The total column emission rate  $4\pi I$  is then

$$4\pi I(\mu) = 4\pi I_I (1 + f_A) \quad (41)$$

Figure 16 shows  $f_A$  from 1800 Å to 3200 Å. The behavior exhibited is similar to that of  $f_s$  and as with that function, multiple scattering effects have been accounted for at the longer wavelengths. We see that Rayleigh scattering is unimportant below  $\sim 3200$  Å.

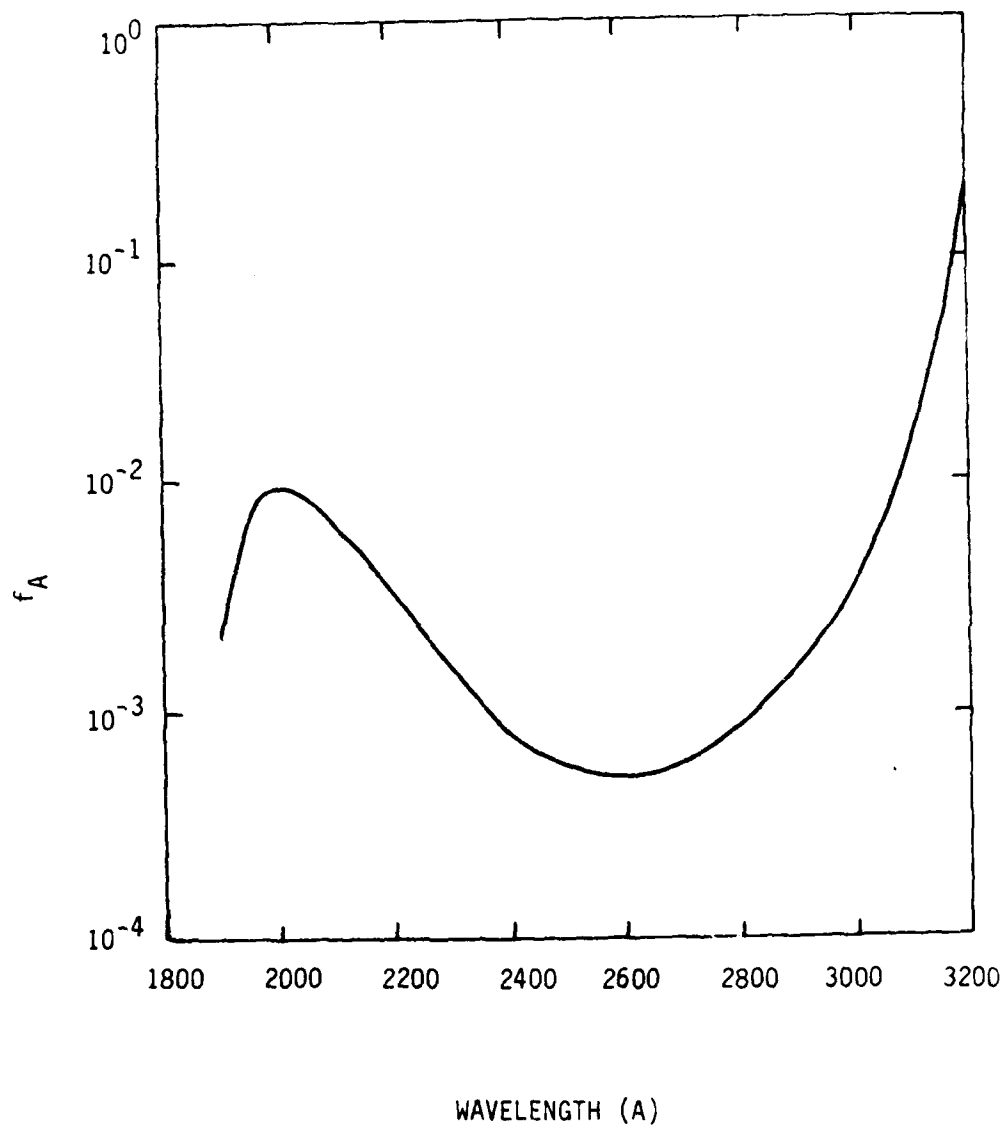


Figure 16 Function  $f_A$  for Rayleigh Backscattering of Auroral Radiation.

## Section 7

### Predictions for Comparison with Data from the 1981 AFGL Auroral E Rocket Program and from the ISIS II Satellite

In this section, we address two unrelated experimental programs which have provided various types of data under auroral conditions. The first to be considered will be the AFGL Auroral E Rocket Program which was carried out on March 7, 1981. Four rockets were launched from the Poker Flat Research Range near Fairbanks, Alaska into the continuous auroral. Observations were made of particles, fields, and optical emissions. The second program involves the ISIS II satellite and of specific interest here are observations which were made with soft particle spectrometers (see Klumpar and Heikkila, 1982).

#### 7.1 Predictions for the Continuous Aurora

The quantities of interest here are the following:

- 1) primary and secondary electron spectra
- 2) ion densities
- and 3) selected optical intensities (OI 1356 A, OI 5577 A, OI 2972 A,  $N_2^+$  IN 3914 A,  $N_2$  2P 3371 A, several LBH bands, and finally the  $N_2$  Vegard-Kaplan (VK) band at 2762 A).

They have been calculated using a Jacchia (1977) model atmosphere with the incident electron spectrum represented by a 1 keV Maxwellian distribution. The energy content  $Q$  is  $1.5 \text{ ergs/cm}^2\text{-s}$  and isotropy is assumed over the downward hemisphere. The chosen representation is close so that deduced from coincident Chatanika radar data (Robinson and Vondrak, 1981) and from AFGL Airborne Laboratory data (J.A. Whalen, private communication, 1981). Primary electron data were not available during the study for direct input into the transport calculations.

We begin with the electron transport results in Figure 17. Shown are spherical fluxes ( $\text{e/cm}^2\text{-s-eV-4}\pi\text{sr}$ ) at the altitudes 300 km (upper boundary), 135 km, and 120 km over the energy range 1.5 eV to 5 keV. We note that we have allowed the incident spectrum to depart from a Maxwellian below  $\sim 200$  eV. If one starts with a true Maxwellian it will be seen to evolve to the spectrum shown at 300 km due to secondary electron production. This occurs before any noticeable energy degradation of the primary spectrum has taken place above a few hundred eV. We thus choose to start with this slightly evolved version of the incoming spectrum.

The minima occurring at  $\sim 2.5$  eV are due to  $\text{N}_2$  vibrational excitation. In this low energy region, some of the loss is also caused by plasma electrons as well as transitions to excited states with low energy thresholds. The plasma density needed for describing loss to the plasma was chosen to be consistent with the incident electron spectrum.

The results shown in Figure 17 are based on a particle-particle interaction description. They show stronger variations below 100 eV than have sometimes been observed (see, e.g. Sharp and Hays, 1972 and Feldman and Doering, 1975). Such discrepancies have been suggested to arise from wave-particle interactions not accounted for in the calculations (see Papadopoulos and Coffey, 1974). Our point here is to acknowledge a potentially important role of plasma turbulence and note under what conditions our own calculations have been made. It seems unlikely, however, that the calculated secondary spectrum is in serious error when taken over the entire altitude range of interest. This is based on its associated emission rates and their agreement with observations (see Meier et al., 1982).

Figure 18 shows calculated ion densities for  $\text{NO}^+$ ,  $\text{O}_2^+$ ,  $\text{N}_2^+$  as well as their sum which is equated to the electron density  $n_e$ . These results come from our time dependent chemistry model which does not include the effect of ion transport. The calculation was continued until chemical equilibrium was achieved. The behavior of the  $\text{NO}^+$  and  $\text{O}_2^+$  densities are sensitive to the amount of NO present. The chosen NO density altitude profile may be found in Table 1 of the appendix.

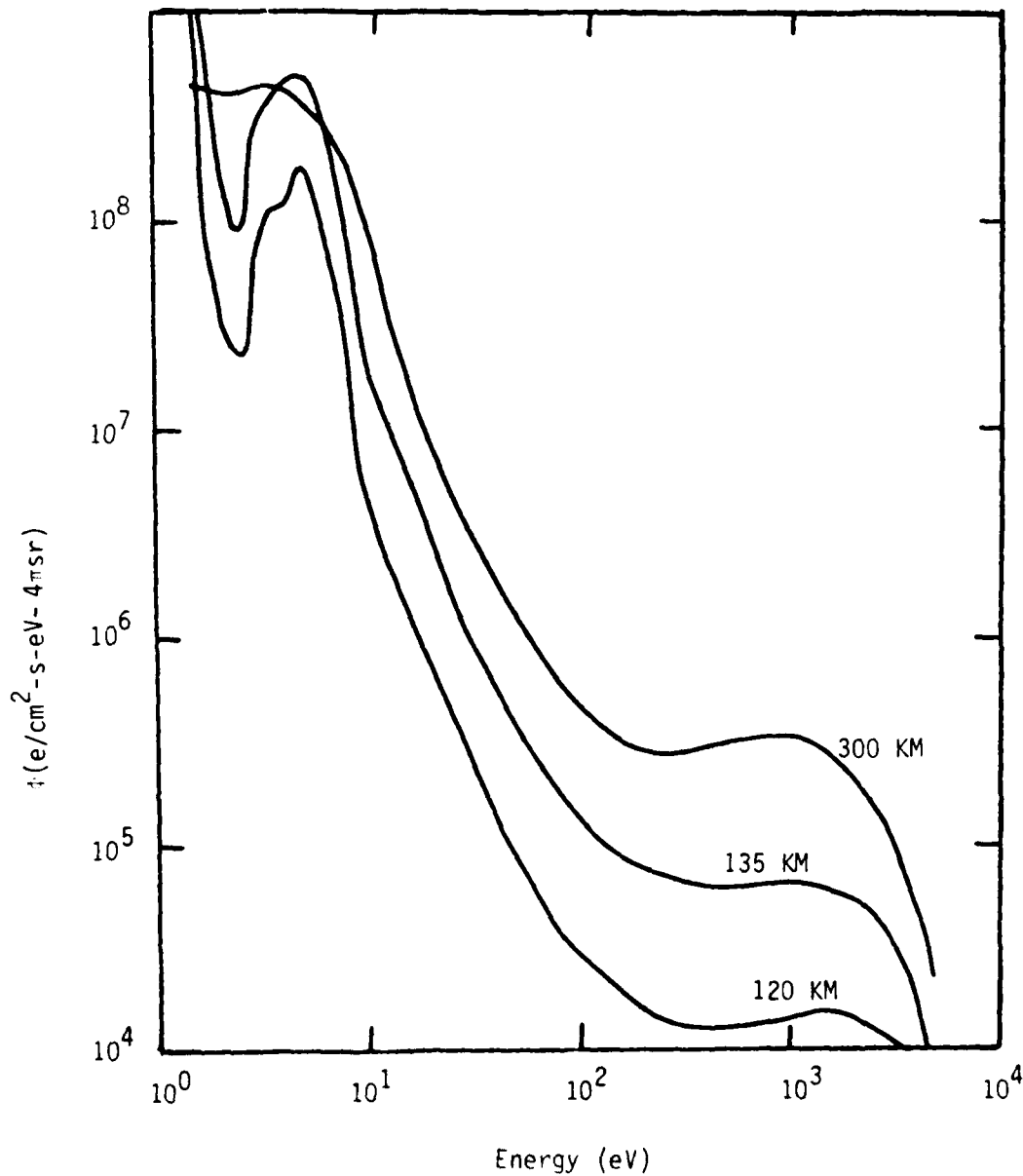


Figure 17 Calculated auroral electron spectra. The incident spectrum is that shown at 300 km which has the dependence of a 1 keV Maxwellian distribution above  $\sim 200$  eV where most of the energy resides.

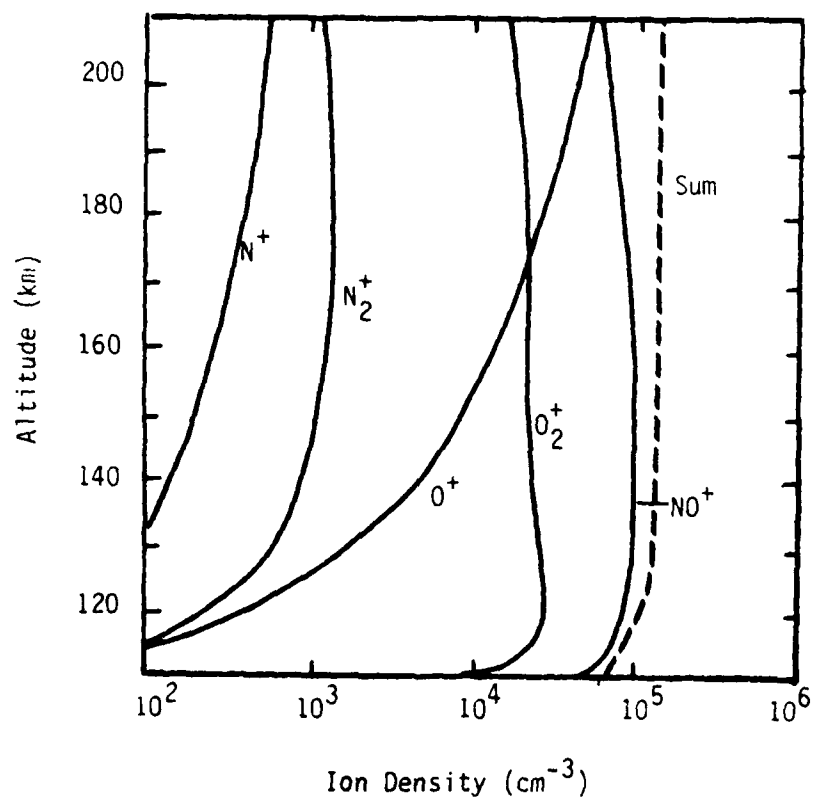


Figure 18 Calculated ion densities based on the incident electron spectrum shown in Figure 17.

The densities in Figure 18 may be compared with various data. We observe the same basic behavior in  $n_e$  deduced by Robinson and Vondrak (1981) although their profile is  $\sim 50\%$  higher. This is not a serious difference given that we do not have a direct measure of what the actual energy content of the incident electron spectrum was. Figure 19 provides a comparison between our results and the data of Swider and Narcisi (1981) for fractional abundances of ions. The data were obtained with an ion mass spectrometer. The overall agreement is good with the exception of  $N_2^+$  for which our results are  $\sim 3$  times larger. We have not yet investigated the cause of this discrepancy.

We now consider the optical emission features listed earlier. Column emission rates (to be referred to as intensities) in kilo-Rayleighs (kR) will be presented for viewing in the zenith direction. Data for the chosen features were obtained for this viewing direction (R.E. Huffman, private communication, 1981, R.A. Van Tassel, private communication, 1981). We begin with the features  $N_2^+ 1N$  3914 A and OI 5577 A whose intensities are among the most prominent in auroras. Figure 4 shows altitude profiles of these intensities (previously presented in our discussion of  $O(^1S)$  chemistry). Both features yield intensities in excess of 1 kR for the given aurora with  $4\pi I_{5577}$  being  $\sim 50\%$  larger at low altitudes. This is consistent with numerous observations which typically show the ratio  $4\pi I_{5577}/4\pi I_{3914}$  to be between 1 and 2.

Figure 20 shows intensities for OI 2972 A,  $N_2$  2P 3371 A, and  $N_2$  VK 2762 A. The differences between the 2762 A and 3371 A profiles are caused by quenching which affects the  $A^3\Sigma$  state leading to 2762 A emission but not the  $C^3\Pi$  state which leads to 3371 A emission. Intensities for selected LBH bands are shown in Figure 21. The profile labeled 1493 A contains contributions from NI 1493 A and the (3,3) band at the same wavelength. The other profiles contain contributions from pairs of bands as indicated in the figure. Pure absorption by  $O_2$  is responsible for the decreases at low altitudes. It is weaker near 1425 A than at, say, 1384 A which leads to the smaller decrease below 120 km for the combined 1426 A - 1430 A intensity profile. The LBH 1354 A intensity is shown in Figure 22 along with that for OI 1356 A as well as their sum. For the given incident electron spectrum, we observe that the LBH contribution to the summed intensity is minor. It will become more important as the hardness of the electron spectrum increases since in this situation, more of the energy becomes deposited in  $N_2$  relative to O.

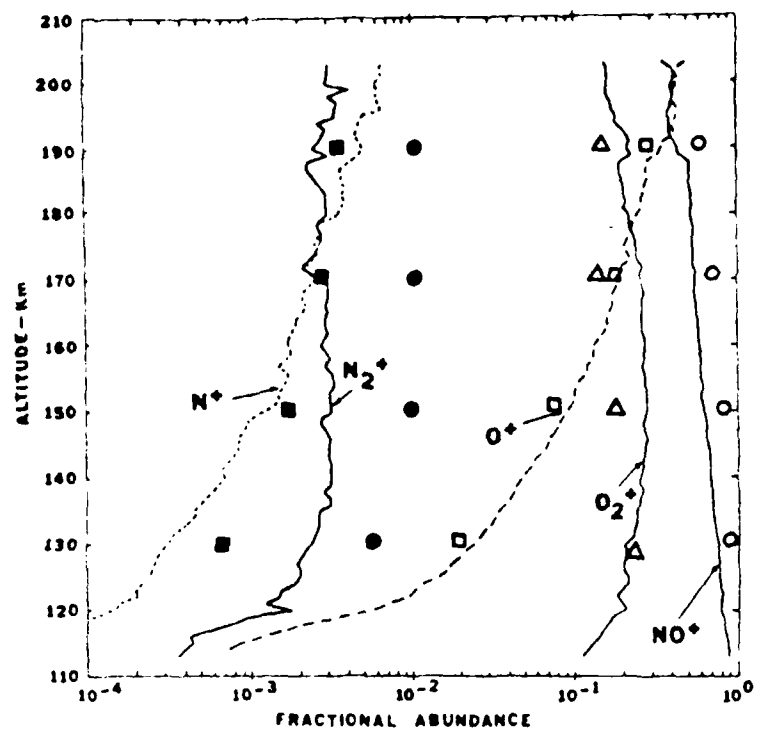


Figure 19 Calculated (symbols) and measured (curves; Swider and Narcisi, 1981) fractional ion abundances.

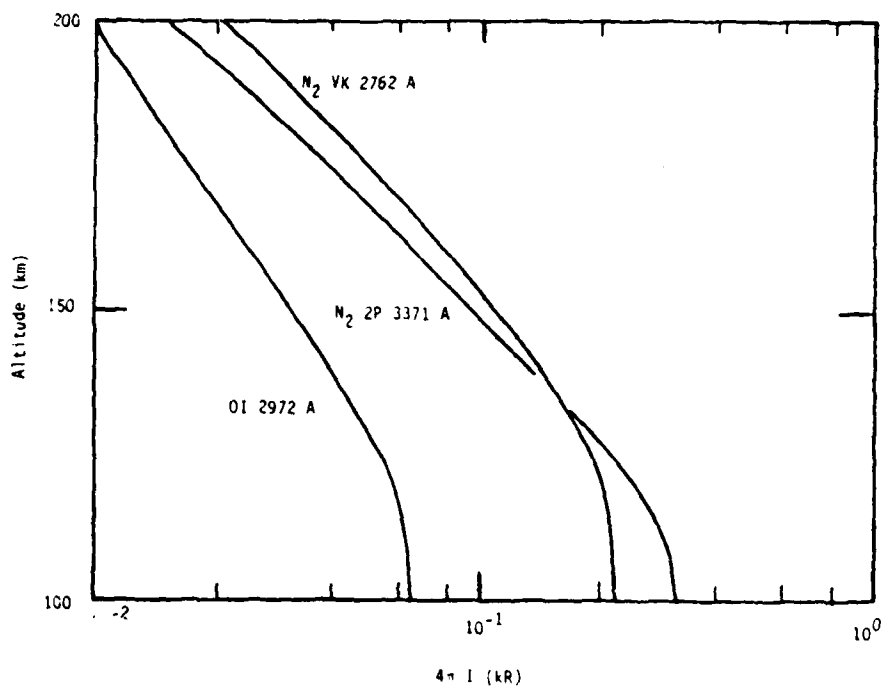


Figure 20 Calculated zenith viewing intensities for conditions described in text.

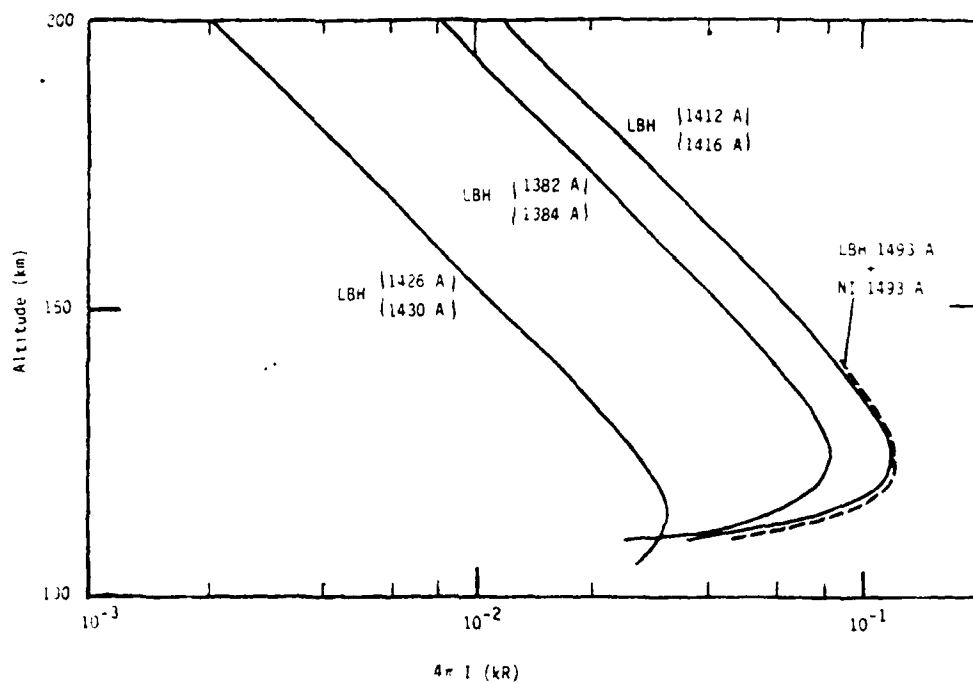


Figure 21 Calculated zenith viewing intensities for conditions described in text.

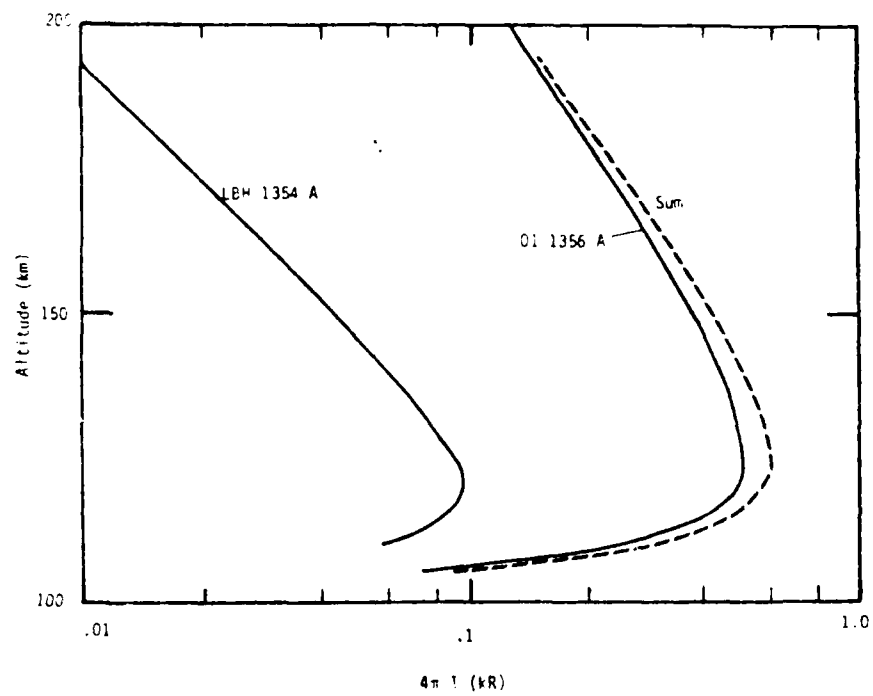


Figure 22 Calculated zenith viewing intensities for conditions described in text.

## 7.2 Election Backscatter Prediction for ISIS II Electron Spectrometer Data Analysis

Two sets of auroral electron spectral data were received from ISIRI with the request to calculate backscattered spectra. The interest in these particular data come from their beam like quality in the downward hemisphere (strongly field aligned at certain energies) and large values at low energies over the upward hemisphere. The behavior of some of the data strongly suggests the existence of parallel electric fields below the satellite. Klumpar and Heikkila (1982) have specifically addressed this issue using data from the experiment we are considering here. Our calculations were requested to determine the extent of backscatter due to collisions so as to better quantify the interaction of electrons (plasma and energetic) with electric fields beneath the satellite.

Figure 23 shows an example of the data used to specify the incident electron spectrum. The left and right panels contain spectra at pitch angles of  $7^\circ$  and  $14^\circ$  respectively and illustrate the beam like nature of the data below a few keV. The altitude at which the observations were made is 1400 km. Transport calculations were done for two sets of data which we shall designate by the labels A and B. For case A, data are available at pitch angles of  $7^\circ$ ,  $14^\circ$ ,  $27^\circ$ ,  $48^\circ$ ,  $68^\circ$ , and  $88^\circ$ . Case B data are available at  $11^\circ$ ,  $31^\circ$ , and  $53^\circ$ . (It should be noted that data do exist at angles above  $90^\circ$  but were not received by us for this analysis.) The pitch angle is here referenced to the downward direction along the geomagnetic field lines. The data at  $53^\circ$  for case B are questionable since numerous data dropouts occur and are otherwise of low magnitude with considerable fluctuation. Case A results, therefore, deserve the greater emphasis.

Figure 24 shows our smoothed representation of the data and the calculated backscattered spectra at selected energies. The calculations were performed with many more energy points than shown in the figure. Twenty non-uniformly spaced  $\mu$  values ( $\mu$  is the cosine of the pitch angle) were used for both cases. At high energies, the backscattered spectrum is weak as expected since forward scattering is strong and few electrons are available at higher energies

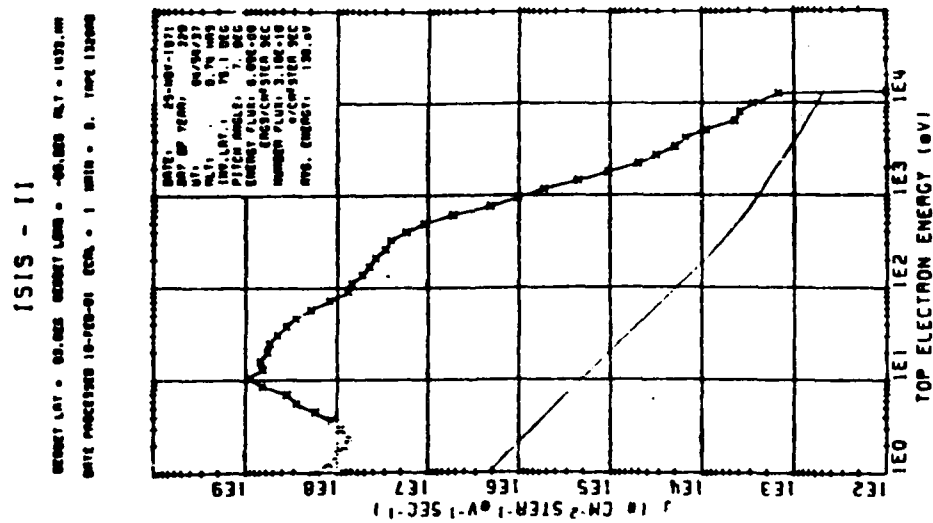
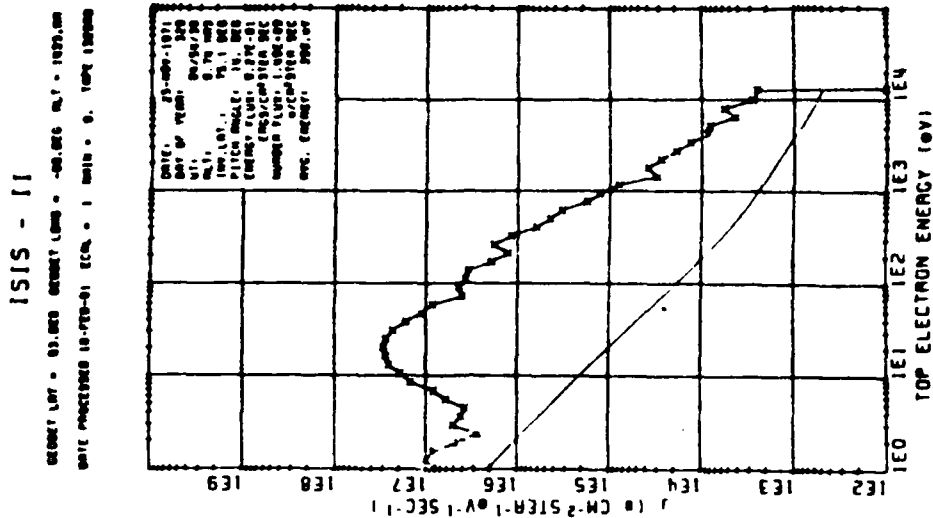


Figure 23 ISIS II electron spectrometer data for pitch angles of 7° and 14° (0° refers to downward direction along field lines).

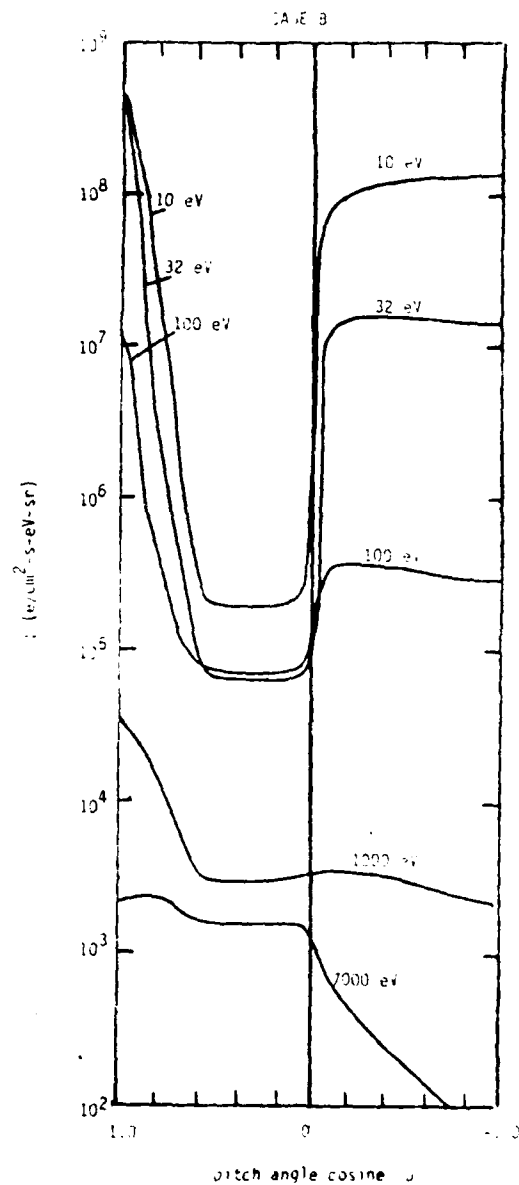
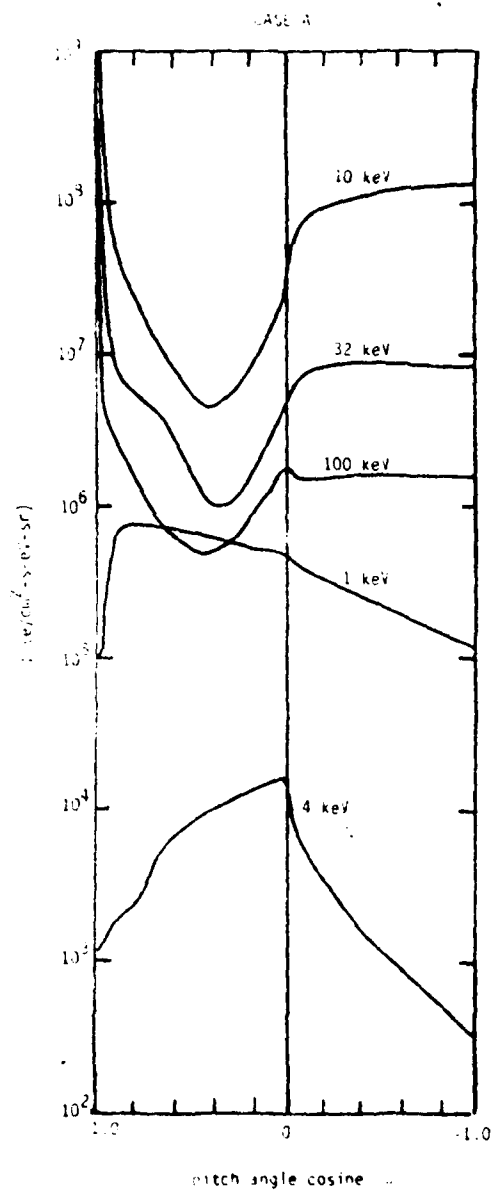


Figure 24 Incident ( $\mu > 0$ ) and calculated backscattered ( $\mu < 0$ ) electron spectra based on ISIS II data such as appear in the previous figure.

which might contribute after considerable energy degradation. At low energies, the upward flux is appreciable due mainly to the rate at which secondary electrons are produced. If one examines the data in the paper of Klumpar and Heikkila (1982), however, it is clear that the amount of backscatter exhibited in our results is insufficient at times to explain observed low energy upward electron fluxes, thus suggesting some acceleration mechanism in the upper ionosphere.

## Section 8

### UV Emissions and the Electron Density in the Daytime Ionosphere

#### 8.1 Background

The problem we address in this section has to do with properties of UV emissions and the electron density in the daytime ionosphere. These quantities vary with geographical location, local time, and from day to day. The causes of variation in emissions other than local time variation are 1) changes in the solar flux producing ionization and 2) changes in the neutral atmosphere above  $\sim 100$  km. These changes also directly affect the electron density. The presence of plasma turbulence, winds, and large scale weak electric fields will also affect the electron density, particularly in the F region. Here, we will restrict ourselves to emission and electron density variations caused by composition and solar flux changes.

We are particularly interested in knowing how useful UV emissions are in determining the daytime electron density profile in the E and F regions. We leave to a later time considerations of how accurately such a determination must be for the technique to be judged useful. To begin addressing the problem, code PEGFAC has been placed on the AFGL computing system and coupled to code CHEM. We are now beginning to obtain results using these codes. These results include photoelectron fluxes, photoelectron produced excitation and ionization rates, primary ionization rates caused directly by the solar flux, densities of all major chemical species, and optical intensities.

PEGFAC refers to photoelectron g-factors which are the parameters that provided the initial motivation for us to develop the code. A g-factor is defined to be some volume excitation or ionization rate divided by the density of the parent species from which the excited species originated. For photoelectron produced excitation, it is also the integral over energy of the excitation cross section times the photoelectron flux. Code PEGFAC provides for the calculation of this flux for various solar conditions and model atmospheres as well as calculation of a large number of excitation rates and their corresponding g-factors.

Code CHEM is our auroral chemistry code which calculates the densities of the important chemical species as well as numerous intensities of molecular band systems and atomic lines. The code now allows for diffusion of  $O^+$  and thus enables us to model the electron density into the F region. Some code modifications have been necessary to adapt CHEM to the daytime problem which are now complete.

In the following subsections, some information will be given concerning the model incorporated into PEGFAC. Calculated intensities and electron densities will also be given as we begin to address the problem as stated at the beginning of this subsection.

As an historical note, a significant part of the coding leading to PEGFAC was done under DARPA/NRL sponsorship to address the problem of secondary electron energy deposition during and following the passage of high current-high energy electron beams in air. Unsponsored work by one of us (D.J.S.) then led to the initial untested version of PEGFAC. Most of this effort was directed to development of a photoelectron source code. Valuable assistance was given by R.R. Meier and colleagues at NRL in providing the necessary detailed information on photoionization cross sections and solar fluxes. Testing and initial application of PEGFAC was then carried out under NASA sponsorship through the Aerospace Corporation. Part of the descriptive information to follow is taken for the documentation of this effort. The results, however, come from this work.

## 8.2 Computational Model

The photoelectron flux is calculated from an integral equation in the local approximation. The equation is basically that considered by Strickland et al. (1976) for auroral electrons and by Oran and Strickland (1978) for photoelectrons without the  $u \frac{du}{dz}$  term. Deleting the transport term greatly simplifies the calculations and is valid for our purposes over the altitude range of important impact excitation. We have compared our solution with one generated using the Oran-Strickland code and observe close agreement to 300 km.

The integral equation is

$$0 = - \sum_l n_l(z) \sigma_l(E) \phi(z, E) + \sum_l n_l(z) \sum_k \int_E^{E_{\max}} \sigma_{lk}(E', E) \phi(z, E') dE' \\ + n_p \frac{\partial}{\partial E} [L_p(E) \phi(z, E)] + S(z, E) \quad (42)$$

with terms defined as follows

- $\phi$  photoelectron flux in  $e/cm^2$ -s-eV
- $S$  source spectrum in  $e/cm^3$ -s-eV
- $n_l$  density of  $l^{th}$  neutral species ( $N_2, O_2$  and  $O$  treated)
- $\sigma_l$  total inelastic cross section of  $l^{th}$  species in  $cm^2$
- $\sigma_{lk}$  inelastic cross section for  $k^{th}$  process involving  $l^{th}$  species in  $cm^2/eV$
- $n_p$  plasma density
- $L_p$  loss function for energy loss to plasma.

We are interested in a variety of volume excitation rates (the term "excitation" will be used at times for both excitation and ionization) for providing chemistry source terms and volume emission rates. These excitation rates come from photoelectron impact excitation and in some cases from direct solar photon excitations. The rates of concern here produced by both processes are ionization rates. The direct solar part is given by

$$P_s(z, \mu_0) = n(z) g_s(z, \mu_0) \quad \text{cm}^{-3}\text{-s}^{-1} \quad (43)$$

with  $\mu_0$  being the cosine of the solar zenith angle and the solar ionization g-factor given by

$$g_s(z, \mu_0) = \int \pi F_\lambda e^{-\tau_\lambda(z)/\mu_0} \sigma_\lambda d\lambda \quad \text{s}^{-1} \quad (44)$$

The terms  $\pi F_\lambda$ ,  $\tau_\lambda$ , and  $\sigma_\lambda$  refer to the unattenuated solar flux ( $\text{cm}^{-2}\text{-s-A}$ ), the total photo-absorption optical depth, and the photo-ionization cross section for some specific ion state.

Since  $P_s$  refers to some specific ion state, it is appropriate to include various subscripts in Equations (43) and (44). We have chosen to leave them off for the sake of simplicity in notation. It should be noted, however, that a sum will be involved in Equation (43) if more than one species leads to production of the given ion species.

The volume excitation rate by photoelectrons for some specific process is

$$P_{pE}(z, \mu_0) = n(z) g_{pE}(z, \mu_0) \quad \text{cm}^{-3}\text{-s}^{-1} \quad (45)$$

with the photoelectron g-factor given by

$$g_{pE}(z, \mu_0) = \int_W^{E_{\max}} \phi_{\mu_0}(z, E) \sigma(E) dE \quad (46)$$

where  $W$  is the excitation threshold energy and subscripts  $\mu_0$  has been added to  $\phi$  to designate that  $\phi$  has this dependence. Again, for simplicity in notation, we chose not to show this dependence in Equations (42) and (43).

The next quantity to be defined is the intensity. We shall consider its computational form for a plane-parallel geometry. Designated as  $I(z, \mu)$ , it is

$$I(z, \mu) = (4\pi)^{-1} \int S(z') T(z, z', \mu) dz' / |\mu| \quad \text{ph/cm}^2\text{-s-sr} \quad (47)$$

where  $S(z)$  is the total volume emission rate and  $T$  is the transmission function between altitudes  $z$  and  $z'$  along a slant path specified by  $\mu$ , the cosine of the look direction. We have not shown the integration limits since they depend on whether  $\mu$  is positive (the convention here is that  $\mu > 0$  corresponds to nadir viewing) or negative (looking up). The emission rate includes a multiple scattered contribution if the medium is optically thick. Here, we will consider only media which are sufficiently thin that  $S(z)$  can be adequately represented by  $S_0(z)$ , the emission rate with no multiple scattering contribution.

The final quantities to be defined are the densities determined from chemistry modeling. These include densities for both neutral and ion species in ground and excited states. The applied rate equation for each species is

$$\frac{dn_i}{dt} = p_i - \lambda_i \quad \text{cm}^{-3}\text{-s}^{-1} \quad (48)$$

where  $p_i$  and  $\lambda_i$  are the production and loss rates for the  $i^{\text{th}}$  species. We shall be interested in the steady state solutions to Equation (48). To solve

the coupled rate equations, we have applied code CHEM, our auroral chemistry code. Transport of  $O^+$  is treated in CHEM and consequently we may examine ionospheric properties in both the E and F regions.

### 8.3 Description of Input/Output Information.

The calculation of photoelectron spectra and associated volume excitation rates requires a large body of input data. In this subsection, we will note the extent of the needed input parameters.

The input information may be catagorized as follows

- model atmosphere
- solar spectrum (EUV to X-ray)
- photoabsorption cross sections
- partial photoionization cross sections
- inelastic cross sections for modeling the photoelectron energy degradation
- loss function for energy loss to the plasma
- and ● excitation cross sections for specifying excitation processes of interest.

Some of these quantities have already been discussed. Nevertheless, we will briefly address each of them here noting either their source or extent. The model atmosphere comes from Jacchia (1971) and is generated in the code once the exospheric temperature,  $T_\infty$ , is specified. We allow for a scaling of the O density through a factor appearing in the input data.

The solar flux values come from Torr et al. (1979) and Donnelly and Pope (1973). In a given run, one of five available spectra is selected

depending on the degree of solar activity to be modeled. A combination of line and continuum band fluxes totaling 38 in number is provided with the Torr et al. spectra. We have replaced their short wavelength band fluxes with line fluxes from Donnelly and Pope (1973). A scaling factor has been introduced to allow experimentation on our part for lack of knowledge on how the soft X-ray fluxes vary with time.

The total absorption cross sections are used to specify the attenuated solar spectrum. They come from Torr et al. (1979). The partial ionization cross sections come from Kirby et al. (1979) and selected papers referenced therein. Photoionization is modeled for five states of  $N_2^+$ , ten states of  $O_2^+$ , and five states of  $O^+$ . The ionization thresholds span an energy range from 12.1 to 25 eV.

There are two sets of electron impact cross sections. The first set defines the energy loss matrix elements while the second set contains members for excitation to states of specific interest to dayglow studies. In terms of energy loss, the latter is a subset of the first. Most of the applied cross sections come from the previous work of Strickland. These may be found in the papers by Strickland et al. (1976) and Oran and Strickland (1978). Recent members have been added for processes such as dissociative ionization of  $O_2$  leading to OII 834 Å. Most of these have come from measurements by E.C. Zipf and colleagues.

The final parameter on the above list is the loss function for energy loss to the plasma. It should be noted that such loss is not important to the study of the UV dayglow. Electron impact excitation leading to UV emission is primarily at electron energies above 10 eV while plasma absorption of the photoelectron energy which affects the flux spectrum occurs below this energy. In spite of this, we include the effect of plasma energy loss so as not to exclude the low energy region from future studies. The applied loss function comes from Schunk and Hays (1971).

We will now briefly describe the output information. The flux  $\phi(z,E)$  is currently calculated for  $\sim 40$  altitudes between 400 and 100 km and for as many as 75 energies. Approximately 40 excitation rates and 45 g-factors are specified on the altitude grid. These refer to ionization, vibrational excitation, electronic state excitation of the states producing important energy loss, and additional processes leading to UV emission at selected wavelengths. The excited state species producing the emission's include  $N_2$ ,  $N_2^+$ ,  $O$ ,  $O^+$ , and  $N$ .

#### 8.4 Calculated Photoelectron Flux and Volume Excitation Rates

An example of the calculated photoelectron flux as obtained from Equation (42) is shown in Figure (25) together with data by Lee et al. (1980). Both spectra apply to low solar activity and are seen to be in good agreement with one another. The applied solar spectrum is shown in Figure 26 with conditions given in the caption.

Figure 27 shows examples of photoelectron produced volume excitation rates for  $N_2$  (a  ${}^1\Pi_g$ ) and  $O$  ( ${}^5S$ ). Conditions are the same as applied to the information in Figures 25 and 26. Solar zenith angles are considered over the range from  $0^\circ$  to  $90^\circ$ . The given states were chosen since we are currently examining their associated emissions which occur in the LBH bands and at 1356 Å.

#### 8.5 Optical Intensities and Electron Densities

The purpose for showing the following results is to both demonstrate a working daytime ionospheric chemistry-emission code and to provide some new information on the use of optical observations for deducing electron densities. We shall restrict the emission results to the  $N_2$  LBH 1383 Å and OI 1356 Å features.

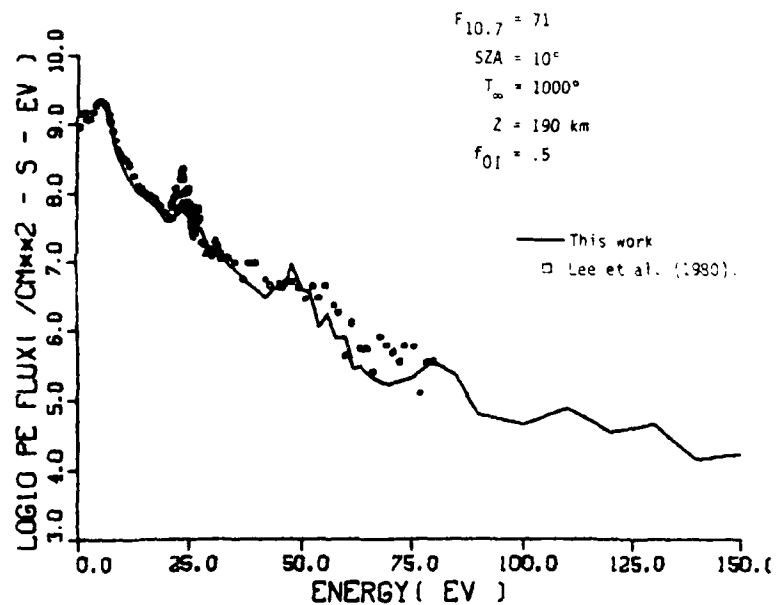


Figure 25 Comparison of calculated and measured  $4\pi$  integrated photoelectron spectra. Both spectra correspond to low solar activity.  $f_{01}$  is the Jacchia (1971)  $n(0)$  scaling factor.

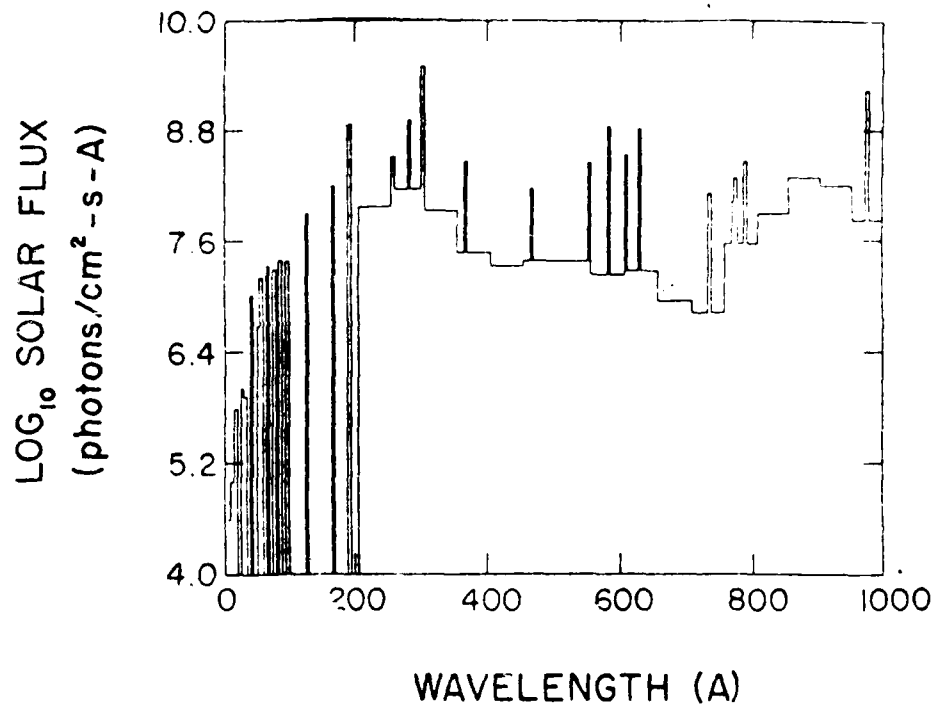


Figure 26 Solar spectrum for low solar activity used in the calculations. Lines have been given a rectangular distribution with a 5 Å width. The spectrum between 200 and 1000 Å is from Torr et al. (1979) who have associated with it a 10.7 cm solar flux of 71. The spectrum below 200 Å come from Donnelly and Pope (1973).

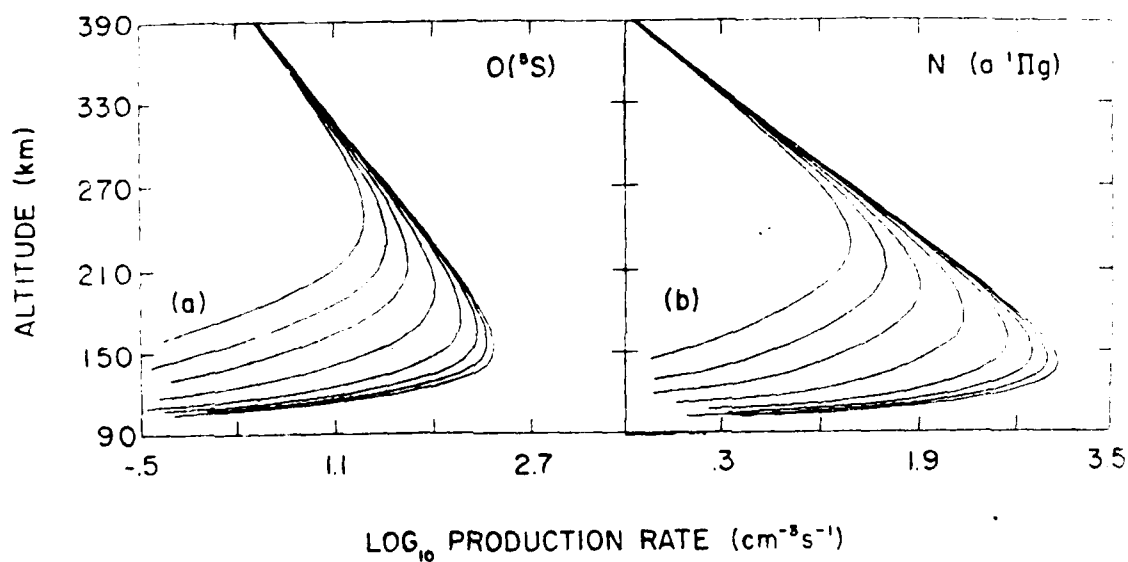


Figure 27 O(<sup>5</sup>S) and N<sub>2</sub>(a <sup>1</sup>Π<sub>g</sub>) volume excitation rates based on the solar spectrum in Figure 26. The rates in each panel from right to left refer to the following solar zenith angles: 0°, 30°, 45°, 60°, 75°, 83°, 88°, and 90°. The exospheric temperature is 1000° K and the Jacchia (1971) n(o) scaling factor is .5.

The 1383 A feature is composed of the (2,0) and (5,2) bands. The LBH band at 1354 A contributes only a small amount to the total 1356 A feature and for this reason will not be considered in the results to follow.

Figure 28 shows zenith and nadir viewing intensities for the chosen features under three sets of conditions. Table 1 identifies these conditions which refer to the level of solar activity and the amount of atomic oxygen present. The case numbers in the table are used to label the curves in Figure 28. We observe a change in intensity of  $\sim 2$  in going from low to high solar activity. As expected, reducing the O density by a factor of 2 reduces the OI 1356 A intensity by a similar factor. The LBH 1383 A intensity is altered only slightly because of a small re-apportionment of photoelectron energy received by  $N_2$ .

Figure 29 shows electron densities for cases 1 and 2. The results above 200 km include the effect of diffusion. We regard these results as preliminary since they are the first obtained by code CHEM as applied to the daytime problem and since the diffusion model is still under development. As preliminary results, we limit them to cases 1 and 2 which is sufficient for the demonstrating variability in the electron density profile and how it relates to corresponding variability in optical intensities.

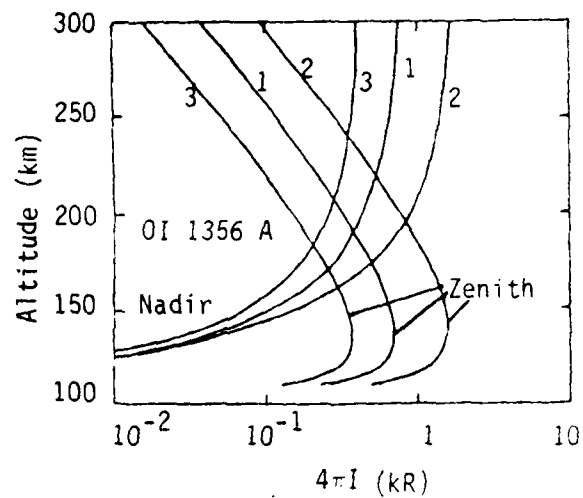
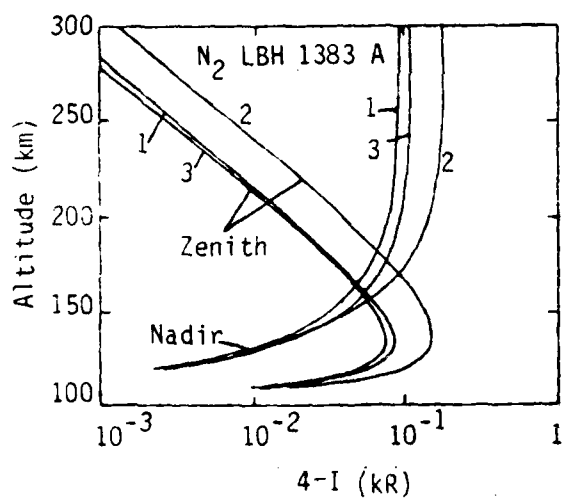


Figure 28 Zenith and Nadir viewing OI 1356 A and  $N_2$  LBH 1383 A dayglow intensities. The solar zenith angle is  $60^\circ$  and  $T_\infty = 1000^\circ$  K. See Table 1 for conditions corresponding to the three cases considered.

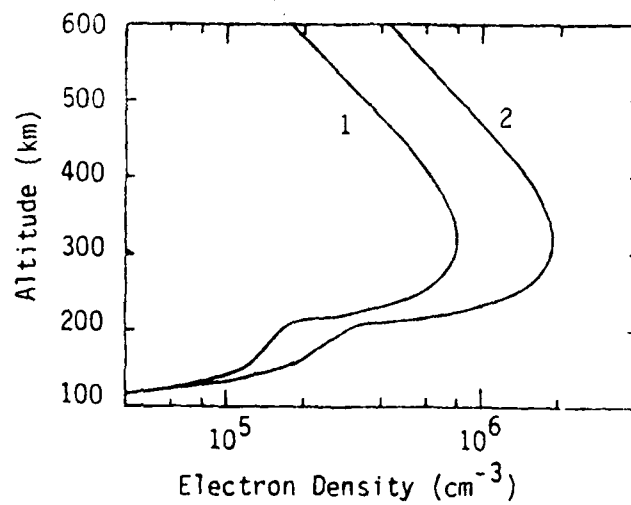


Figure 29 Calculated daytime electron density. Labeling is the same as in Figure 28.

Table 1

Cases for which results have been obtained  
with code PEGFAC.  $T_{\infty} = 10^{10}^{\circ}$  and the solar  
zenith angle is  $60^{\circ}$

Case	Jacchia (1971) n(0) scaling factor	$F_{10.7}$
1	1	71
2	1	206
3	.5	71

# Section 4

## References

- Ames, W.F., Numerical Methods for Partial Differential Equations, Academic Press, New York, 1977.
- Anderson, D.E., Jr. and R.R. Meier, Effects of Anisotropic Multiple Scattering on Solar Radiation in the Troposphere and Stratosphere, Applied Optics, 18, 1955, 1979.
- Banks, P.M. and G. Kockarts, Aeronomy, Parts A and B, Academic Press, New York, 1973.
- Barlier, E., C. Berger, J.L. Falin, G. Kockarts, and G. Thuiller, A Thermospheric Model Based on Satellite Drag Data, Ann. Geophys., 34, 9, 1978.
- Bauer, S.J., Physics of Planetary Ionospheres, Springer-Verlag, New York, 1973
- Cartwright, D.C., Vibrational Populations of the Excited States of  $N_2$  Under Auroral Conditions, J. Geophys. Res., 83, 517, 1978.
- Cartwright, D.C., Excitation of  $N_2$  and  $N_2^+$  Band Emissions in Normal Auroras, in Symposium on Aurora and Airglow, IAGA, Kyoto, 1973.
- Chandra, S., E.I. Reed, R.R. Meier, C.B. Opal, and G.T. Hicks, Remote Sensing of the Ionospheric F Layer by use of OI 6300 A and OI 1356 A Observations, J. Geophys. Res., 80, 2327, 1975.
- Donnelly, R.F. and J.H. Pope, The 1-3000 A Solar Flux for a Moderate Level of Solar Activity for use in Modeling the Ionosphere and Upper Atmosphere, Tech. Rep. ERL 276-SEL 25, NOAA, Boulder, Colo., 1973.
- Evans, J.V., The Dynamics of the Ionosphere and Upper Atmosphere in Physics of Solar Planetary Environment, AGU, Washington, 1976, pp. 630-671.
- Fejer, B.G. and M.C. Kelly, Ionospheric Irregularities, Rev. Geophys. Space Phys., 18, 401, 1980.
- Feldman, P.D., D.E. Anderson, Jr., R.R. Meier, and E.P. Gentieu, The Ultraviolet Dayglow 4. The Spectrum and Excitation of Singly Ionized Oxygen, J. Geophys. Res., 86, 3583, 1981.
- Feldman, P.D. and J.P. Doering, Auroral Electrons and the Optical Emissions of Nitrogen, J. Geophys. Res., 80, 2808, 1975.
- Frolich, C. and G.E. Scaw, "New Determination of Rayleigh Scattering in Terrestrial Atmosphere", Applied Optics, 19, 1773, 1980.
- Hargreaves, J.K., The Upper Atmosphere and Solar Terrestrial Relations, Van Nostrand Reinhold, New York, 1979.

- Hedin, A.E., J.E. Salah, J.V. Evans, C.A. Reber, G.P. Newton, N.W. Spencer, P.C. Kayser, D. Alcayde, P. Bauer, L. Cogger, and J.P. McClure, A Global Thermospheric Model Based on Mass Spectrometer and Incoherent Scatter Data, MSIS 1, N<sub>2</sub> Density and Temperature, J. Geophys. Res., 82, 2139, 1977a.
- Hedin, A.E., C.A. Reber, G.P. Newton, N.W. Spencer, H.C. Brinton, H.G. Mayr, and W.E. Potter, A Global Thermospheric Model Based on Mass Spectrometer and Incoherent Scatter Data, MSIS 2 Composition, J. Geophys. Res., 82, 2148, 1977b.
- Hedin, A.E., N.W. Spencer, H.G. Mayr, and H.S. Porter, Semi-empirical Modeling of Thermospheric Magnetic Storms, J. Geophys. Res., 86, 3515, 1981.
- Hyman, E. and P. Julienne, AURORA: An NRL Auroral Chemistry Code, NRL Memorandum Report 2965, 1975.
- Jacchia, L.G., Revised Static Models of the Thermosphere and Exosphere with Empirical Temperature Profiles, Smithsonian Astrophysical Observatory Special Report 332, 1971.
- Jacchia, L.G., Thermospheric Temperature, Density, and Composition: New Models, Smithsonian Astrophysical Observatory Special Report 375, 1977.
- Kirby, K., E.R. Constantinides, S. Babeu, M. Oppenheimer, and G.A. Victor, Photoionization and Photoabsorption Cross Sections of He, O, N<sub>2</sub>, and O<sub>2</sub> for Aeronomic Calculations, At. Data Nucl. Tables, 23, 63, 1979.
- Klumpar, D.M. and W.J. Heikhila, Electrons in the Ionosphere Source Cone: Evidence for Runaway Electrons as Carriers of Downward Birkeland Currents, Geophys. Res. Lett., 9, 873, 1982.
- Kumar, S., F. Paresce, S. Chakrabarti, and S. Bowyer, Satellite Observations of O<sup>+</sup> 834 A Dayglow, submitted to J. Geophys. Res., 1982.
- Lee, J.S., J.P. Doering, T.A. Potemra, and L.H. Brace, Measurements of the Ambient Photoelectron Spectrum from Atmospheric Explorer 1. AE-E Measurements Below 300 km During Solar Minimum Conditions, Planet. Space Sci., 28, 947, 1980.
- Meier, R.R. and D.E. Anderson, Jr., Determination of Atmospheric Composition and Temperature from the UV Airglow, submitted to Planet. Space Sci., 1982.
- Newman, A.L., A.B. Christensen, and D.E. Anderson, Jr., Atomic Oxygen Density Deduced from Limb Scans of the UV Dayglow, to be submitted to J. Geophys. Res., 1982.

- Oran, E.S. and D.J. Strickland, Calculation of the Ionospheric Photoelectron Distribution Function, Planet. Space Sci., 26, 1161, 1978.
- Ossakow, S.L., Ionospheric Irregularities, Rev. Geophys. Space Phys., 17, 521, 1979.
- Papadopoulos, K. and T.P. Coffey, Nonthermal Features of the Auroral Plasma Due to Precipitating Electrons, J. Geophys. Res., 79, 674, 1974.
- Piper, L.G., G.E. Caledonia, and J.P. Kennealy, Rate Constants for Reactivation of  $N_2(A^3\Sigma_u^+, v'=0,1)$  by O, J. Chem. Phys., 75, 2847, 1981.
- Probst, G.W., Perturbation of the Low-Latitude Upper Atmosphere During Magnetic Substorm Activity, J. Geophys. Res., 87, 5260, 1982.
- Robinson, R.M. and R.R. Vondrak, Chatanika Radar Measurements During the Auroral E Program, AFGL-TR-81-0283, 1981.
- Roble, R.G. and M.H. Rees, Time-Dependent Studies of the Aurora: Effects of Particle Precipitation on the Dynamic Morphology of Ionospheric and Atmospheric Properties, Planet. Space Sci., 25, 991, 1977.
- Sharp, W.E., Rocket-Borne Spectroscopic Measurements in the Ultraviolet Aurora: Nitrogen Vegard-Kaplan Bands, J. Geophys. Res., 76, 987, 1971.
- Sharp, W.E. and D.G. Torr, Determination of the Auroral  $O(^1S)$  Production Sources from Coordinated Rocket and Satellite Measurements, J. Geophys. Res., 84, 5354, 1979.
- Sharp, W.E. and P.B. Hays, Low-energy Auroral Electrons, J. Geophys. Res., 77, 6828, 1972.
- Shemansky, D.E., The  $N_2$  Vegard-Kaplan System in Absorption; J. Chem. Phys., 51, 689, 1969.
- Shunk, R.W. and P.B. Hays, Photoelectron Energy Losses to Thermal Electrons, Planet. Space Sci., 19, 113, 1971.
- Strickland, D.J. and T.M. Donahue, Excitation and Radiation Transport of 1304 Å Resonance Radiation I. The Dayglow, Planet. Space Sci., 18, 661, 1970.
- Strickland, D.J. and M.H. Rees, the OI 1304 and 1356 Å Emissions in Aurora, Planet. Space Sci., 22, 465, 1974.

- Strickland, D.J., D.L. Book, T.P. Coffey, and J.A. Fedder, Transport Equation Techniques for the Deposition of Auroral Electrons, J. Geophys. Res., 81, 2755, 1976.
- Strickland, D.J., Electron Transport, Chemistry, and Optical Emissions in the Auroral E-Layer, Final Report submitted to AFGL, 1981.
- Strickland, D.J. and R.R. Meier, A Photoelectron Model for the Rapid Computation of Atmospheric Excitation Rates, NRL Memorandum Report, in progress, 1982a.
- Strickland, D.J., J.R. Jasperse, and J.A. Whalen, Dependence of Auroral FUV Emissions on the Incident Electron Spectrum and Neutral Atmosphere, submitted to J. Geophys. Res. 1982b.
- Strickland, D.J., R.E. Daniell, and J.R. Jasperse, Using Satellite Observed UV Intensities to Deduce Electron Density Profiles, submitted to American Institute Aeronautics and Astronautics, 1982c.
- Strobel, D.F. and M.B. McElroy, The F2-Layer at Middle Latitudes, Planet. Space Sci., 18, 1181, 1970.
- Sullivan, J.O. and A.C. Holland, A Congeries of Absorption Cross Sections for Wavelengths Less Than 3000 A, NASA CR-371, 1966.
- Swider, W. and R.S. Narcisi, Problems With the  $N_2^+ + O \rightarrow NO^+ + N$  Reaction in Aurora, Geophys. Res. Lett., 8, 1239, 1981.
- Tinsley, B.A. and J.A. Bittencourt, Determination of the F Region Height and Peak Electron Density at Night Using Airglow Emissions from Oxygen, J. Geophys. Res., 80, 2333, 1975.
- Torr, D.G. and M.R. Torr, Review of Rate Coefficients of Ionic Reactions determined from Measurements made by Atmospheric Explorer Satellites, Rev. Geophys. Space Phys., 16, 327, 1978.
- Torr, D.G. and M.R. Torr, The Role of Metastable Species in the Thermosphere, Rev. Geophys. Space Phys., 20, 91, 1982.
- Torr, M.R., D.G. Torr, R.A. Ong, and H.E. Hinteregger, Ionization Frequencies for Major Thermospheric Constituents as a Function of Solar Cycle 21, Geophys. Res. Lett., 6, 771, 1979.
- Vallance Jones, A., Aurora, Reidel, Boston, 1974.
- Vallance Jones, A. and R.L. Gattinger, Quenching of the  $N_2$  Vegard-Kaplan System in Aurora, J. Geophys. Res., 81, 497, 1976.

Appendix

DEPENDENCE OF AURORAL FUV EMISSIONS  
ON THE INCIDENT ELECTRON SPECTRUM AND  
NEUTRAL ATMOSPHERE

Submitted to J. Geophys. Res., 1982

DEPENDENCE OF AURORAL FUV EMISSIONS  
ON THE INCIDENT ELECTRON SPECTRUM AND  
NEUTRAL ATMOSPHERE

D.J. Strickland  
BEERS ASSOCIATES, INC.  
Post Office Box 2549  
Reston, Virginia 22090

J.R. Jasperse and J.A. Whalen  
AIR FORCE GEOPHYSICS LABORATORY  
Hanscom AFB  
Massachusetts 01731

# ABSTRACT

In this paper we examine the relationship among certain prominent auroral FUV emission features, the incident electron spectrum, and the model neutral atmosphere. Given the neutral atmosphere we show that for simple models of the incident electron spectrum (Maxwellian and Gaussian in energy) satellite measurements of FUV emission features, in principle, determine the incident electron spectrum. We also discuss the relationship between the incident electron spectrum and the E-region plasma density profile for the continuous (diffuse) aurora and for a stable arc.

## 1. INTRODUCTION

Our motivation for studying the relationship between auroral UV emissions and the associated electron spectra is our desire to utilize satellite optical emission observations to infer the particle spectra which produce them. Under certain conditions it may also be possible to use satellite UV measurements to infer certain E-region ionospheric properties, e.g., the plasma density profile.

This is the first of two papers addressing auroral optical emissions in the UV. In this paper we examine the dependence of selected features in the short wavelength region of the  $O_2$  Schumann-Runge absorption continuum on the incident electron spectrum. This region lies within the FUV region which runs from  $\sim 1050$  Å to 1800 Å. As will be seen, the variation of the  $O_2$  absorption with wavelength leads to some noticeable intensity ratio changes as the hardness of the incident auroral electron spectrum changes. The ratio we refer to is the intensity ratio of two distinct emission features for nadir viewing conditions.

The second paper now in preparation will address features in the middle UV such as OI 2972 Å and the Vegard-Kaplan bands. As the wavelength increases, the question arises as to when Rayleigh scattering, ground and cloud albedo, and scattering from aerosols become important. For auroral conditions the answer is at wavelengths longer than  $\sim 3000$  Å. At shorter wavelengths and especially for the region to be addressed in this paper, pure absorption is strong enough to prevent the radiation from penetrating to depths where scattering can take place.

Electrons and protons from the plasma sheet pitch-angle scatter into the atmospheric loss cone and precipitate to produce auroras. In the midnight sector both electrons and protons contribute to the aurora with sometimes coincident and sometimes separated latitudinal distributions (Whalen and Sharber, 1981). The proton and H-atom contribution to the auroral

AD-A126 318

UV EMISSIONS AND THE ELECTRON DENSITY IN THE AURORAL  
AND LOW TO MID-LATIT. (U) BEERS ASSOCIATES INC RESTON  
VA D J STRICKLAND ET AL. NOV 82 AFGL-TR-82-0373

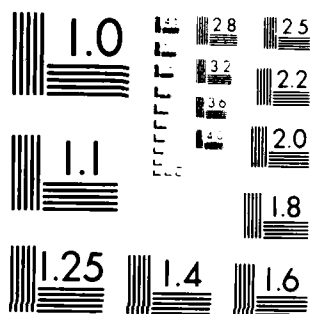
2/2

UNCLASSIFIED F19628-81-C-0066

F/G 4/1

NL

END
DATE
FILED
3 JUL
DTIC



MICROCOPY RESOLUTION TEST CHART  
 NATIONAL BUREAU OF STANDARDS-1963-A

ionization rate can be calculated (Jasperse and Basu, 1982) and, for coincident electron-proton precipitation and typical continuous (diffuse, auroral) conditions, the protons and H-atoms contribute about 10% to the total E-region ionization rate (Jasperse and Basu, 1982, Figure 8). In this paper we assume that the proton-H atom contribution to the FUV emissions is also about 10% of the electron contribution and consider only the effect of the latter. The two types of electron produced auroral forms we shall consider are the continuous aurora and the stable arc. They are discussed in detail in Section 3.

There have been many attempts at deducing the incident auroral spectrum from the intensities of optical emissions in the visible region (see, e.g. Rees and Luckey (1974), Vallance Jones (1975), Arnoldy and Lewis (1977), Shepherd et al. (1980), and references therein). The features considered have been OI 5577 Å, OI 6300 Å, and either  $N_2^+$  3914 Å or 4278 Å, all of which are prominent in auroras and can be observed from the ground. For most analyses, the intensity variations of these features with changing electron spectrum come from Rees and Luckey who characterized their spectra by Maxwellian distributions. As noted by Arnoldy and Lewis (1977), the technique has been fairly successful in estimating the mean electron energy and energy content of the incident electron spectrum. Rees and Luckey do acknowledge, however, a potential problem due to difficulties over the years in explaining the 5577 Å emission which is chemistry dependent. Examples of analyses where predictions have agreed poorly with observations may be found in Rees et al. (1977), Sharp et al. (1979), and Arnoldy and Lewis (1977). For this reason we prefer to study the relationship between the electron spectrum and the FUV features addressed in this paper which have the advantage of being chemistry independent.

## 2. BACKGROUND

The works of Strickland et al. (1976), Meier et al. (1980), Meier et al. (1981) and Conway (1982) form the basis for this study. The needed electron transport model comes from Strickland et al. (1976). Meier et al. (1980) achieved, for the first time, a self-consistent picture of the FUV  $N_2$  and NI dayglow emissions analyzing the rocket data of Gentieu et al. (1979). This work quantified the excitation sources and processes affecting the transmission of the photons, namely multiple scattering and pure absorption. Conway (1982) performed a line-by-line synthesis of individual LBH bands examining band transmission. He derived transmission functions for self absorption taking into account the varying strengths of the individual rotational lines and found the transmission to be larger than previously thought (Meier et al., 1981). This led to the important conclusion that  $O_2$  pure absorption dominates self absorption for all of the prominent bands. Meier et al. (1981) extended their dayglow work to the analysis of auroral rocket data of Feldman and Gentieu (1981) and again were able to achieve a self-consistent picture for the above features as well as NII 1085 A, OI 1356 A, and OI 1304 A. Regarding LBH, they showed that the  $v'$  populations of the  $a^1\Pi_g$  state were consistent with those for direct excitation from the ground state. They were also able to infer the approximate nature of the precipitating electron flux and the amount of  $O$  present from the available LBH and 1356 A data. The flux determination was made possible by the differing amounts of  $O_2$  pure absorption from one LBH band to another which is the effect to be discussed in some detail in this paper.

We are considering the following features:  $N_2^+$  1N (0,0) at 3914 A, OI 1356 A, and the  $N_2$  LBH bands at 1273 A (6,0), 1325 A (4,0), 1354 A (3,0), and 1384 A (2,0 and 5,2). Spectroscopically,  $N_2^+$  3914 A stands apart from the rest of the features but is included since its emission is strong, it is measured in most auroral particle and optical experiments, energy input relates directly to its intensity, and finally it is

well understood. The remaining features have been selected since 1) they possess no albedo from below the ionosphere, 2) some show strong variations with electron spectral hardness, 3) all are prominent in auroral FUV spectra, 4) blending is not a problem since they do not blend with one another (with the exception of OI 1356 Å and LBH 1354 Å as noted below) nor with other nearby features such as OI 1304 Å for resolutions better than, say, 10 Å (see, e.g., Feldman and Gentieu, 1981), and finally, 5) these features, like  $N_2^+$  3914 Å, are reasonably well understood (Meier et al., 1980; Meier et al., 1981). LBH 1354 Å and OI 1356 Å are effectively blended and for this reason will be discussed at times in this paper as one feature. We do not wish to eliminate them from consideration because of blending since OI 1356 Å has the potential as a useful signature on the amount of atomic oxygen (O) present. Mention should be made of OI 1304 Å since it is one of the most prominent features in the FUV spectral region. We choose not to include this feature in the above list for two reasons. First, there is a severe computational problem in accurately determining its emission properties due to extensive multiple scattering (Strickland and Donahue, 1970; Meier and Lee, 1982). Second, its nadir intensity is not necessarily an accurate signature of electron impact excitation along the given line of sight (even correcting for the obvious multiple scattering effects) due to the non-local nature of the given emission. If, for example, a nadir observation were made adjacent to some region of brighter emission, some of the observed signal would be due to radiation originating from this brighter region and would consequently overestimate the initial electron impact excitation in the observed region.

Zipf and his colleagues (McLaughlin et al., 1982) have recently reported that various LBH bands are blended with atomic nitrogen lines and other  $N_2$  bands. In addition, they suggest that optical pumping of the  $a^1\Pi_g$  state from the  $c_4'^1\Sigma_u^+$  state is a significant source in the upper atmosphere. These complications will not be addressed in this paper. First, such complications, from a computational point of view, will only affect the applied emission cross section for each feature so affected. This could lead to a change in the strengths of what we are referring to as our LBH features but not any noticeable changes in their relative behavior from one auroral situation to another. This last statement

applies because the same impact species ( $N_2$ ) is responsible for the multiple components suggested by McLaughlin et al. Second, our interest is in optical properties on the resolution scale appropriate to today's rocket and satellite borne UV spectrometers which do not resolve blended features as discussed above. We shall continue to refer to the features being considered as was done in the previous paragraph keeping in mind that some scaling may be called for in the future.

We noted above that there should be little relative intensity variation among those features being referred to as LBH bands due to either blending or cascading as auroral conditions change. This statement is based on the assumption that in going from one auroral situation to another, the electron spectrum has not shifted from its expected occurrence in the keV region to the sub-keV region. As long as we exclude that situation, there is little relative variation in excitation efficiencies between, say, the  $a^1\Pi$  and  $c'$  states as the electron spectrum is changed. One does arrive at a point, however, as the spectrum softens, where this is no longer true due to the differences in respective impact cross section shapes. For very soft auroral spectra, the more forbidden nature of the  $a^1\Pi$  cross section leads to relatively more  $a^1\Pi$  excitation compared to, say,  $c'$  excitation. Our transport calculations show that this effect is not important as long as the mean energy of the incident electrons is greater than approximately one kilovolt.

There is one obvious disadvantage to using the chosen set of features for probing the auroral ionosphere in contrast to the set  $N_2^+$  3914 Å, OI 5577 Å, and OI 6300 Å which we discussed earlier. That disadvantage concerns the demands placed on the measurements. A spectrometer is required for which one must be concerned with resolution, scanning rates, and signals weaker than from such prominent features as those just cited. This point is further emphasized by the present paucity of good spectral data from satellite experiments for our chosen set of features. Nevertheless, demands placed on instrumentation are becoming more modest with present advancements in state-of-the-art detection systems.

### 3. SOME FUV EMISSION OBSERVATIONS

An auroral optical spectrum including the FUV features of interest to this work is given in Figure 1. This spectrum was obtained in a rocket experiment with the spectrometer looking down from above the emitting layer (P.D. Feldman, private communication, 1981). The  $O_2$  pure absorption cross section is included as well as an altitude scale showing where unit optical depth occurs due to  $O_2$  absorption based on the adjacent cross section scale. In Section 6, we will show that absorption strongly affects the LBH band at 1384 Å but has little effect on the band at 1273 Å over the range of incident electron spectra considered.

There are two basic types of E-region auroras; continuous (or diffuse) and discrete. The two are different not only in spatial characteristics but also in temporal and precipitating particle characteristics. The two types are illustrated in Figure 2 which shows a latitudinal graph of a band of FUV emissions detected by a nadir viewing photometer on satellite S3-4 as it crossed the auroral region near midnight (Huffman et al., 1981). The band pass (full width at half maximum) of the filter used was 165 Å with its transmission maximum at 1550 Å. The broad continuum which peaks near  $-66.5^\circ$  C.G. latitude shows the continuous aurora; the peaks near  $-69^\circ$  and  $-70.5^\circ$  identify discrete auroras.

The latitudinal distribution of the continuous aurora has an FWHM of about  $5^\circ$  and so is consistent with other observations which find the distribution of precipitated particle energy flux to be near Gaussian in latitude with approximately the same scale parameter (Whalen, 1981). These observations also find the latitudinal distribution to be uniform throughout approximately 12 hours of magnetic local time. The distribution in Figure 2 departs somewhat from a Gaussian because the FUV emission is dependent not only on energy flux, but also on particle characteristic energy which is known to vary with latitudes (Sharber, 1981).

Although a very extensive and stable auroral feature, the continuous aurora has frequently not been detected because of its relatively low brightness. Even when detected, the morphology of this aurora has been difficult to describe because its distribution broadens in latitudinal width with decreasing intensity. As a result, its apparent width is a function of the threshold of the detector which observes it. Thus, the distribution of continuous aurora in Figure 2 would appear to be about  $2^\circ$  wide to a detector with a threshold corresponding to 100 R, but approximately  $8^\circ$  wide to a detector with a threshold of 6 R. Similar difficulties exist in the specification of the latitude of the equatorward boundary of this aurora because of its sensitive dependence on detector threshold.

The continuous aurora is stable on a time scale of at least minutes (Whalen, 1981) and is produced by precipitating keV electrons with a minor contribution from protons (Lui et al., 1977; Sharber, 1981). The energy spectrum of the electrons obtained by averaging over the loss cone is usually Maxwellian (Sharber, 1981).

Discrete auroras, on the other hand, are extremely variable in time, latitude, and longitude. The normal behavior of the discrete form is to change on a time scale that is short compared to an E-region chemical time constant ( $\sim 1$  minute). Discrete auroral forms that vary on a time scale longer than a chemical time constant will be regarded as stable arcs. The prominent auroral arc in Figure 2 was imaged by a DMSP satellite at approximately the same location at which the S3-4 satellite observed it (Huffman et al., 1981). Since the DMSP measurement preceded that of the S3-4 satellite by 10 minutes, the arc was apparently stable in position. However, there is no information which could insure that the arc was also stable in brightness. Discrete auroras are produced by precipitating electrons which have energy spectra that are often modelled by Gaussian functions of energy (e.g. Fontheim et al., (1982)

The source of particles that produce both types of auroral forms is apparently the plasma sheet; those electrons producing the continuous aurora usually have Maxwellian spectra characteristic of the plasma sheet (Rearwin and Hones, 1974) and those electrons producing discrete auroras have spectra consistent with additional acceleration produced by electric field structures located in the magnetosphere (Evans, 1974). In this regard the maximum in the near Gaussian latitudinal distribution for the continuous aurora is an important magnetospheric feature since it represents the normal equatorward limit of discrete auroras (Lui et al., 1977). In Figure 2 we note the absence of discrete auroras in the equatorward half of the latitudinal distribution. Furthermore, because of the uniformity of the continuous aurora in local time, the value of the energy flux at the maximum in the latitudinal distribution is an indicator of auroral activity on a large scale (Whalen, 1981). A further fundamental significance of the maximum in the latitudinal distribution shown in Figure 2 is its location at or near the interface between positive and negative field aligned currents (Robinson et al., 1982).

#### 4. APPROACH

For the chosen set of emission features we wish to know their relative variations in intensity as functions of the incident electron spectrum and the model atmosphere. To study this problem we solve the Boltzmann electron transport equation for several incident differential electron number fluxes characterized by Maxwellian and Gaussian distributions. The equation is

$$\begin{aligned} \mu \frac{d\phi(z, E, \mu)}{dz} = & k(z, E) \left[ -\phi(z, E, \mu) + \sum_{\ell} r_{\ell}(z, E) \int R_{\ell}(E', E, \Theta) \phi(z, E', \mu') d\Omega' dE' \right] \\ & + n_p(z) \frac{\partial}{\partial E} [L_p(z, E) \phi(z, E, \mu)] \end{aligned} \quad (1)$$

with terms defined as follows:

$z, E, \mu$	altitude, energy, and direction cosine
$\Theta$	scattering angle
$\phi$	differential electron number flux (electron spectrum) in $e/cm^2-s-eV-sr$
$k$	total inverse mean free path (IMFP) in $cm^{-1}$
$r_{\ell}$	fractional IMFP for $\ell^{th}$ species
$R_{\ell}$	scattering and energy loss redistribution function for $\ell^{th}$ species in $eV^{-1}sr^{-1}$
$n_p$	plasma density in $cm^{-3}$
$L_p$	plasma loss function in $eV-cm^2$ .

The function  $k$  is given by

$$k(z, E) = \sum_{\ell} n_{\ell}(z) \sigma_{\ell}(E) \quad [\text{cm}^{-1}] \quad (2)$$

where  $n_{\ell}$  is the  $\ell^{\text{th}}$  neutral density ( $\text{N}_2, \text{O}_2$ , or  $\text{O}$ ) and  $\sigma_{\ell}$  is the total electron impact cross section (elastic plus inelastic). The function  $r_{\ell}$  is

$$r_{\ell}(z, E) = [k(z, E)]^{-1} n_{\ell}(z) \sigma_{\ell}(E) \quad (3)$$

The function  $R_{\ell}$  contains several terms describing elastic scattering, excitation, and ionization. More details regarding  $R_{\ell}$  and the solution of Equation (1) may be found in Strickland et al. (1976).

Equation (1) yields a solution from primary electron energies in the keV range to secondary electron energies in the low eV range. Thus, the volume emission rates of interest to us here, lacking chemically produced components, may be obtained from this solution using

$$P_{\ell i}(z) = n_{\ell}(z) \int_{w_{\ell i}}^{E_{\text{max}}} \sigma_{\ell i}(E) \phi(z, E, L) 2\pi d\Omega dE \quad [\text{cm}^{-3} \cdot \text{s}^{-1}] \quad (4)$$

where  $w_{\ell i}$  is the threshold for the  $i^{\text{th}}$  excitation process of the  $\ell^{\text{th}}$  species. The corresponding intensity in the absence of enhanced emission caused by multiple scattering is

The function  $k$  is given by

$$k(z, E) = \sum_i n_i(z) \sigma_i(E) \quad [\text{cm}^{-1}] \quad (2)$$

where  $n_i$  is the  $i^{\text{th}}$  neutral density ( $\text{N}_2, \text{O}_2$ , or  $\text{O}$ ) and  $\sigma_i$  is the total electron impact cross section (elastic plus inelastic). The function  $r_i$  is

$$r_i(z, E) = [k(z, E)]^{-1} n_i(z) \sigma_i(E) \quad (3)$$

The function  $R_i$  contains several terms describing elastic scattering, excitation, and ionization. More details regarding  $R_i$  and the solution of Equation (1) may be found in Strickland et al. (1976).

Equation (1) yields a solution from primary electron energies in the keV range to secondary electron energies in the low eV range. Thus, the volume emission rates of interest to us here, lacking chemically produced components, may be obtained from this solution using

$$P_{\lambda i}(z) = n_i(z) \int_{w_{\lambda i}}^{E_{\text{max}}} c_{\lambda i}(E) \phi(z, E, \lambda) 2\pi dE \quad [\text{cm}^{-3} \cdot \text{s}^{-1}] \quad (4)$$

where  $w_{\lambda i}$  is the threshold for the  $i^{\text{th}}$  excitation process of the  $i^{\text{th}}$  species. The corresponding intensity in the absence of enhanced emission caused by multiple scattering is

$$I_{\lambda i}^j(z, \mu_0) = (4\pi)^{-1} \int_{z_{\min}}^z P_{\lambda i}(z') w_{\lambda i}^j \exp[-(t_{\lambda i}^j(z') - t_{\lambda i}^j(z))/\mu_0] T(z', z, \mu_0) dz' / \mu_0$$

[ph/cm<sup>2</sup>-s-sr] (5)

where  $\mu_0$  is the cosine of the look direction ( $\mu_0 = 1$  for true nadir direction),  $t$  is the pure absorption optical depth, and  $T$  is the self absorption transmission function (see, e.g. Strickland, 1979 for lines and Conway, 1981 for bands). The factor  $w_{\lambda i}^j$  is a branching ratio and allows for the possibility of more than one emission feature arising from the  $\lambda i^{\text{th}}$  excited state. For example, the index  $j$  for molecular bands represents the double index  $v' v''$  designating the upper and lower vibrational levels of the transition producing the band emission. Results to follow will be in the form of  $4\pi I$  with units of kilo-Rayleighs. I shall continue to use the term intensity for this quantity although more properly it is referred to as an apparent column emission rate. The depth  $z$  is given for  $O_2$  and has the form

$$t(z) = \sigma_{O_2}(\lambda_i) \int_z^\infty n_{O_2}(z') dz' \quad (6)$$

Figure 3 shows  $t$  versus  $z$  for the LBH bands under investigation. We note that unit optical depth occurs at less than 90 km for the 1273 Å feature in contrast to 120 km for the 1384 Å feature. In turn, as stated earlier, the 1273 Å intensity is not affected by pure absorption over the range of incident electron spectra being considered whereas the 1384 Å intensity is strongly affected.

A modified version of Equation (5) should be used for OI 1356 Å due to multiple scattering effects (Anderson et al., 1980). Its form is

$$I(z, \mu_0) = (4\pi)^{-1} \int_{z_{\min}}^z S(z') \left[ \frac{5}{8} T_5(z', z, \mu_0) + \frac{3}{8} T_3(z', z, \mu_0) \right] dz' / \mu_0 \quad (7)$$

where  $S$  is the total volume emission rate in both lines of this doublet feature (1355.5 Å and 1358.5 Å). The transmission fraction  $T_{\text{g}}$  refers to 1355.5 Å while its subscript refers to the statistical weight of the  $^3P_2$  ground state level. The function  $S$  is obtained from the integral equation

$$S(z) = S_0(z) + \int_{z_{\min}}^{z_{\max}} S(z')H(z,z')dz' \quad [\text{ph/cm}^3\text{-s}] \quad (8)$$

where  $S_0$  is the initial excitation rate [given here as  $P_{\text{gi}}$  in Equation (4)] and  $H$  is a modified Holstein  $H$  function (Holstein, 1947) taking into account the doublet structure of the 1356 Å feature. A detailed discussion of Equation (8) as it applies to another multiplet, that of OI 1304 Å, is given by Strickland and Donahue (1970). The differences arising in  $4\pi I$  by using Equation (7) in place of Equation (5) will be discussed later.

We have chosen to describe some of our incident electron spectra with Maxwellian distributions since they are characteristic of the precipitation producing the continuous aurora as determined by averaging spectra over the loss cone (Sharber, 1981 and Whalen and Sharber, 1981). In addition, Maxwellians are convenient to use and have been frequently used before (see, e.g., Roble and Rees, 1977 and Rees and Luckey, 1974). Let  $\phi_0(E)$  be the incident differential electron number flux which we assume to be isotropic. For a Maxwellian, it is given by

$$\phi_0(E) = \left( \frac{Q_M}{2\pi E_M^3} \right) E \exp [-E/E_M] \quad [\text{e/cm}^2\text{-s-eV-sr}] \quad (9)$$

where  $E$  is the electron energy,  $E_M$  is the characteristic energy and  $Q_M$  is the energy flux. Under certain conditions the incident spectrum includes a high-energy tail (Vondrak, 1981). A high-energy tail can be included by adding a second term to Equation (9) and would introduce additional parameters. Since the high-energy tail is not always present and since it produces mainly D-region effects we neglect its effect.

Maxwellian distributions do not characterize auroral and electron spectra very satisfactorily since these spectra generally have a sharper peak (see, e.g., Boyd, 1975 and Lui et al., 1977). For this reason we have included some narrow Gaussian distributions in our study. The expression for  $i_0$  using a Gaussian distribution is

$$i_0(E) = \left( \frac{Q_G}{-3/2 W E_G} \right) \exp \left[ - \left( \frac{E - E_G}{W} \right)^2 \right] \quad [\text{e/cm}^2\text{-s-eV-sr}] \quad (10)$$

where the quantities introduced have similar meanings as those introduced in Equation (9). In this work, the Gaussian scale parameter,  $W$ , has been given values equal to  $0.25 E_G$ . In the following sections, when general properties of the results are discussed, we shall use  $E_0$  and  $Q_0$  to refer to either  $E_M$  or  $E_G$  and to  $Q_M$  or  $Q_G$ .

## 5. MODEL ATMOSPHERE AND ATOMIC AND MOLECULAR PARAMETERS

The basic model atmosphere used in this work comes from Jacchia (1977). This is given in Table 1. An indication of density variability in the auroral ionosphere is given in Figure 4 where the Jacchia model is compared with one reported by Rees et al. (1977) and Sharp et al. (1979). The comparison is provided through ratios of the respective model densities. Atomic oxygen is seen to be more than a factor of three smaller as reported by Rees et al. and Sharp et al. Guided by such differences, some of our results have been obtained with a scaled down Jacchia O density. Specifically, intensities will be shown for the Jacchia O density reduced by three. There is also O<sub>2</sub> density variability shown in Figure 4 although this is modest below 120 km where pure absorption exhibits most of its effect. Results have been obtained with two scalings of the Jacchia O<sub>2</sub> density. The scaling factors are 1.5 and .667 which allow for a range of variables that we assume is more than adequate to reflect actual changes below 120 km.

A full set of electron impact ionization and excitation cross sections for N<sub>2</sub>, O<sub>2</sub> and O is needed to perform the transport calculations. The basic set is given by Strickland et al. (1976) and Oran and Strickland (1978) with some modifications based on recent experimental data. The needed rates  $P_{ij}$  require cross sections for exciting N<sub>2</sub>(a <sup>1</sup>Π<sub>g</sub>) and OI (<sup>5</sup>S) and ionizing N<sub>2</sub> to N<sub>2</sub><sup>+</sup>(B<sup>2</sup>Σ<sub>u</sub><sup>+</sup>). Table 2 gives peak cross section values  $\sigma_{\text{max}}$  and references to their full energy dependences. These are the same cross sections used in the auroral analysis of Meier et al. (1981). Table 3 gives the percent of N<sub>2</sub>(a <sup>1</sup>Π<sub>g</sub>) and N<sub>2</sub><sup>+</sup>(B<sup>2</sup>Σ<sub>u</sub><sup>+</sup>) production going to the various bands under consideration. The table also contains the O<sub>2</sub> pure absorption cross sections for all of the features. Again, these values are the same as those appearing in Meier et al. (1981). The emission factor in Table 3 for 3914 Å comes from Vallance Jones (1974). The factors for LBH were derived by R.R. Conway and are similar to those given by Vallance Jones for the specific bands of interest.

An assumption we make in this work is that the  $v'$  populations of the  $a^1\pi_g$  state do not vary with changing auroral conditions. In turn, this also means that the emission factors do not change. This assumption should be valid as long as additional excitation mechanisms beyond those discussed in Section 2 are not operating. Huffman et al. (1980) have reported satellite photometric and spectrometer observations of nighttime LBH emissions which extend into the auroral region. The nighttime band distribution is shifted to longer wavelengths compared to that for auroral electron impact excitation. Such a nighttime component of a low level auroral spectrum may change the assumed  $v'$  distribution since total nighttime LBH intensities in excess of 1 kR have been observed. Caution should, therefore, be exercised in using results to follow for weak auroras.

## 6. CALCULATED VOLUME PRODUCTION RATES AND INTENSITIES

### 6.1 Volume Production Rates as Functions of $E_0$

Results have been obtained for several values of  $E_M$  and  $E_G$ . These are  $E_M = .5, 1.0, 2.5$ , and  $5.0$  keV and  $E_G = 1.0, 2.0, 3.3, 5.0, 7.5$  and  $10.0$  keV. The energy parameters  $Q_M$  and  $Q_G$  have been selected to give  $1 \text{ erg/cm}^2\text{-s}$  for the incident energy. Figure 5 gives the  $N_2$  and  $O$  production rates for the incident spectra given by the above characteristic energies. The top panel contains the Maxwellian results while those for the Gaussian spectra appear in the lower panel.

As expected, the Gaussian results are more sharply peaked and one cannot find an  $E_G$  value which precisely reproduces the results for some given  $E_M$  value. The relationship  $E_G = 3E_M$  is approximately correct, however, for achieving the same altitudes of maximum excitation and ionization.

Figure 6 shows production rates for  $O(^5S)$ . For the larger characteristic energies, the area beneath a given profile (column production rate) decreases with increasing characteristic energy in contrast with the behavior in Figure 5. This is caused by the decrease in the  $O$  to  $N_2$  density ratio with decreasing altitude and has the desirable effects for producing stronger intensity variations with electron spectral hardness than would occur by pure absorption effects alone.

### 6.2 Intensities as Functions of $E_0$ and $Q_0$

For our standard model atmosphere (Table 1), intensities appear in Figures 7 and 8 versus characteristic energy for Maxwellian and Gaussian incident electron spectra. The dominant effect producing the

differing variations with  $E_0$  among these intensities is  $O_2$  pure absorption. At small values of  $E_0$ , pure absorption has little effect on any of the features since emission occurs where  $t_{O_2}$  is small. The fall off observed in the  $N_2$  emissions as  $E_0$  approaches zero results from high altitude energy deposition where there is relatively less  $N_2$  compared to  $O$  than at lower altitudes. Consequently, less of the available energy is being absorbed by  $N_2$  and more by  $O$  which results in weaker  $N_2$  emissions. At larger values of  $E_0$ , most emission occurs where strong contrasts exist in pure absorption from one feature to another. We see that this leads to relative variations as large as a factor of about four between 1273 Å and 1384 Å for the given  $E_0$  range. Variations of this strength make such features attractive as monitors of the hardness of the incident electron spectrum. The weakness of their intensities relative to  $N_2^+$  3914 Å may make it difficult to obtain good signal-to-noise ratios in actual observations unless the incident spectrum contains several ergs/cm<sup>2</sup>-s. It may be more attractive to monitor the intensity at 3914 Å in place of 1273 Å due to its brightness, its similar variation with  $E_0$ , and the ability to make the measurement with a photometer although account must be taken of albedo and backscatter unlike in the FUV region.

The strongest variations with  $E_0$  occur for OI 1356 Å and result from the combined effects of  $O_2$  pure absorption and the relative variation of  $O$  to  $N_2$  as a function of altitude. For larger values of  $E_0$ , less of the available incident electron energy goes to  $O$  due to lack of this constituent where the energy deposition is occurring. OI 1356 Å is clearly a useful feature for estimating electron spectral hardness if one knows the  $O$  density. We have seen evidence of enough variability in this density that such usefulness can be expected to be rather limited without some measure of this quantity. Subsection 6.3 will address the sensitivity of the 1356 Å intensity to scalings of the  $O$  density.

We noted earlier that there is some effect on the OI 1356 Å intensity due to multiple scattering. The extent of this effect has been determined for selected  $E_0$  values and two  $n(O)$  profiles (D.E. Anderson, Jr., private communication, 1982). One profile is that in Table 3, while the

other is obtained by scaling the first by .33. The difference between the single scattering (Equation 5) and multiple scattering (Equation 7) intensities is about 15% at small  $E_0$  values for  $n(0)$  given in Table 3. It decreases with increasing  $E_0$  because of the increasing importance of  $O_2$  pure absorption which inhibits multiple scattering. For the reduced  $n(0)$  profile, the maximum difference is only about 5%. In either case, multiple scattering effects will not significantly impact upon our long range goals in this work. They do become more important when viewing along greater lines-of-sight and should not be ignored, e.g., when considering limb viewing conditions (Strickland and Anderson, 1983).

Figure 9 shows the intensities as functions of  $Q_0$  for the Maxwellian characteristic energy  $E_M = 2.5$  keV. This value was selected because it lies in the middle of the applied range. Since the applied Boltzmann equation is linear, its solution as well as the intensities based upon it vary linearly with  $Q_0$ . In spite of this simple behavior, Figure 9 is included since it is useful for obtaining the various emission strengths at a glance for a range of the precipitating electrons' energy content.

### 6.3 Intensities as a Function of the Altitude for Maximum Energy Deposition

It is instructive to display the intensities in Figures 7 and 8 as functions of the altitude of peak energy deposition,  $z_p$ , which bears a one-to-one correspondence with  $E_0$ . By doing so, we may combine the intensities for Maxwellian and Gaussian electron spectra on the same plot and conveniently note similarities and differences in the intensity behavior for these two representations.

Figure 10 shows the intensities of Figures 7 and 8 versus the given altitude parameter. For convenience, let us refer to the intensities for the two source representatives as  $I_M$  and  $I_G$ . In general,  $I_G$  decreases more slowly with decreasing  $z_p$ . To understand why, we must consider the effect of pure absorption for volume emission profiles peaking at the same altitude but with different distributions about this peak. It is clear that a smaller amount

of the emission below the peak is purely absorbed for the Gaussian case since the emission does not extend as deeply into the atmosphere. The opposite effect occurs above the peak where relatively more of the emission for the Maxwellian case extends into the non-absorbing region. Pure absorption under these circumstances may lead to either greater or less intensity for one type of intensity versus the other. Greater intensities have been seen to occur in Figure 10 for the Gaussian case over the range of  $E_G$  considered. Less intensity will finally occur, however, with increasing  $E_G$  since pure absorption becomes so strong that only the upper part of the volume emission profile contributes to the intensity. Since this profile has relatively less extension to high altitudes compared to the Maxwellian case, relatively less radiation can escape. The altitude,  $z_p$ , at which this occurs is, of course, a function of the feature or wavelength. For all features shown, this altitude occurs below 104 km.

Our primary motivation for generating Figure 10 was to determine how well  $z_p$  can be specified from intensity ratios regardless of electron source characteristics. Clearly, these ratios are not useful for soft sources giving  $z_p \gtrsim 115$  km. The situation is much improved for harder sources leading to the exhibited variations. A unit ratio of  $4\pi I_{1384}$  to  $4\pi I_{1273}$ , for example, gives a value close to 105 km for either representation. Even better determination of  $z_p$  is possible using  $4\pi I_{1356}$  if one knows the  $O$  density profile.

#### 6.4 Intensities as a Function of the Model Neutral Atmosphere

We introduced our applied model atmosphere in Section 5 and noted the kinds of density variations that may occur under varying auroral conditions. Uncertainties in the  $O_2$  and  $O$  densities can have a strong impact on the usability of nadir intensities for the features being considered. For this reason, we have determined the sensitivity of these intensities to what we regard as reasonable ranges of variability in the above densities. Figure 11 gives the 1356 Å intensity versus  $E_M$  for the Jacchia  $O$  density and one scaled down by a factor of 3. The LBH contribution is unaffected by this variation. The  $OI$  1356 Å component, on the other hand, varies almost linearly with scalings of  $n(O)$ . This

behavior clearly limits the usefulness of the 1356 Å intensity as an indicator of electron spectral hardness unless  $n(0)$  is known. We may turn the argument around, however, and note that if the hardness is known by other means, then this feature will be useful for determining the amount of O present.

We now consider the sensitivity of selected intensities to  $n(O_2)$  variations. The results appear in Figure 12 for  $n(O_2)$  ranging from .67 to 1.5 times the Jacchia values. The given variations clearly complicate matters if  $n(O_2)$  cannot be better specified than, say, 50% in actual calculations. Specifically, we are addressing uncertainties below  $\sim 120$  km. At these lower altitudes, the model comparisons in Figure 4 lead to much smaller differences which if indicative of the actual degree of  $n(O_2)$  variability in the auroral ionosphere suggest that such variability will not play an injurious role in the use of intensities as proposed here.

## 7. CALCULATED IONIZATION RATES AND ELECTRON DENSITIES

In this section we go one step further in relating the intensities of UV features to conditions prevailing in the ionospheric under bombardment by auroral electrons. We shall introduce the electron density  $n_e$  and show its altitude dependence for the various incident electron spectra already discussed. There are certain caveats we wish to address before this is done. Many parameters effect  $n_e$  through chemistry, transport and auroral turbulence. To avoid the complicating effect of plasma transport, we limit our considerations to the E-region. We also consider situations where turbulence is weak enough not to measurably affect the distribution of the plasma.

A range of calculated  $n_e$  profiles is possible with regard to the chemistry through variations in densities with long resident times and uncertainties in rate coefficients which include those terms affecting temperatures as well as chemically derived densities. Examples of species with long resident times whose variations from aurora to aurora must be kept in mind are NO and O<sub>2</sub>. Variations in their densities can significantly affect ion concentrations although produce much less affect on their sum or equivalently,  $n_e$ . The concentration of NO will slowly build up under continuous auroral activity and thus can depend significantly on conditions minutes to hours earlier than the given time of interest. Table 1 gives the NO density as well as those of the dominant neutral species used to generate the  $n_e$  profiles to follow. The NO density comes from a previous calculation for modest energy deposition continuing for about 1 hour. Although we have used this NO density profile to calculate the  $n_e$  densities to follow, use of substantially different profiles (factor of ten either way, for example) would not noticeably affect  $n_e$  in comparison to the degree of effect caused by changes in the electron spectrum over the chosen range of spectral hardness.

We have calculated electron densities using a detailed chemistry model as well as the approximation

$$n_e(z) = [n_i(z)/\bar{\alpha}(z)]^{1/2} \quad \text{cm}^{-3} \quad (11)$$

where  $\alpha_i$  is the total ionization rate and  $\bar{\alpha}$  is the effective recombination coefficient. Densities to follow come from the detailed calculations but do not differ significantly from those obtained using Equation (11). The respective profiles are essentially the same below their maxima with  $\sim 30\%$  departure at higher altitudes. The larger values in the departure region refer to the simpler calculation.

In our chemistry model, we solve a set of coupled rate equations with each equation given by

$$\frac{dn_i(z)}{dt} = p_i(z) - l_i(z) \quad [\text{cm}^{-3}\text{-s}^{-1}] \quad (12)$$

where  $p_i$  and  $l_i$  are the production and loss terms for the ion chemical species. We currently model 16 species which include metastable as well as ground state ions and minor neutral species. The important ion species are  $\text{NO}^+$ ,  $\text{O}_2^+$ ,  $\text{O}^+$ , and  $\text{N}_2^+$  with the latter providing an important source to the others through charge transfer reactions. The electron density is specified by requiring charge neutrality. Most of our rate coefficients come from Roble and Rees (1977) with some adjustments based on Torr and Torr (1982). A number of these coefficients are allowed to vary with  $T_e$ , the electron temperature. For results to follow,  $T_e$  has been specified from those calculations by Roble and Rees (1977) which apply in an approximate way to our conditions.

Having briefly described the conditions under which  $n_e$  is specified, we now turn to our final results which appear in Figures 13 and 14. Shown are total ionization rates and corresponding  $n_e$  profiles for Maxwellian and Gaussian distributions. As before, energy content is fixed at  $1 \text{ erg/cm}^2\text{-s}$ . The chemistry calculations were extended to sufficiently long times that steady state conditions prevail. Our interest here is not so much in the detailed behavior of the  $n_e$  profiles shown but rather in their relative sensitivity to  $E_0$  over a range which gives measurable variations in the intensities under consideration. We will, however, make some comparisons between  $n_e$  profiles in further discussion below for the two chosen

source representations. Given our emphasis, we do not raise here the issue of just how accurately  $n_e$  profiles can be determined given present uncertainties in rate coefficients and the starting conditions of the ionosphere. That issue must eventually be addressed to help answer the question of the practicability of using satellite observed optical emissions for ionospheric monitoring. Returning to Figures 13 and 14, it is clear that  $n_e$  cannot be very well specified from our chosen set of UV features for soft electron precipitation such as given by  $E_m$  in the range .5 to say 1.5 keV. Over this range, intensity ratios change modestly whereas significant variations occur in the distribution of  $n_e$ . For harder electron spectra, a more precise specification of  $n_e$  is possible due both to the stronger intensity variations as shown in Figures 7 and 8 and to the more confined nature of the  $n_e$  profiles about their maxima.

In the previous section, we discussed the possibility of directly estimating the altitude of maximum energy deposition  $z_p$  from the chosen intensities. Figure 10 showed that such a specification of  $z_p$  improves as it decreases in value and that below a value of  $\sim 120$  km, the technique appears attractive. For such values,  $z_p$  also applies to  $n_e$  which thus allows us to directly estimate the altitude of maximum  $n_e$  from results like those in Figure 10. The fact that the energy deposition rate and  $n_e$  peak at the same altitude (provided that the electron spectrum is not too soft) can be seen by comparing the panels in either Figure 13 or 14. It should be added that the ion production rates shown have the same shape as the energy deposition rate to which Figure 10 refers.

To conclude this section, we briefly comment on differences between  $n_e$  profiles for the two source representations in which respective characteristic energies are chosen to give the same altitude for maximum ionization. We have in mind the situation where the altitude of  $n_{e\max}$  is approximately known using information such as given in Figure 10. The question then arises as to how much variation can be expected in  $n_e$  over the possible range of incident electron spectra which give the same altitude for  $n_{e\max}$ . In Figures 13 and 14, we see that  $E_m = 2.5$  keV and  $E_G = 7.5$  keV lead to a common altitude of  $\sim 109$  km for  $n_{e\max}$  and thus, let us address these energies. As expected,  $n_e$  is more broadly distributed for the Maxwellian source and accordingly has a smaller maximum. The difference in effective lower boundaries, as defined here to be where  $n_e$  is falling rapidly, is  $\sim 4$  km.

At higher altitudes, such as 160 km,  $n_e$  for the Maxwellian source is a factor of  $\sim 1.5$  larger in magnitude. Such differences appear modest under the conditions for which they arise. Nevertheless, whether such differences are important depends, of course, on how one wishes to use such deduced profiles.

## 8. DISCUSSION

There are many mechanisms one must consider in relating auroral optical properties to associated plasma conditions. Those considered in this paper have been 1) electron transport based on a particle-particle description, 2) excitation and ionization associated with this transport, 3) pure absorption, and 4) the chemistry which relates excitation and ionization rates to the electron and ion densities. Other mechanisms identified were photon scattering and plasma turbulence. Scattering was noted to have no effect on the features considered here with the exception of OI 1356 A for which minor effects occur. This statement is dependent on viewing conditions and here we are referring to non-horizontal look directions. Turbulence may manifest itself in modifying energy deposition of the incoming energetic auroral electrons or in creating irregularities in the plasma. Since neither effect has been addressed here, our conclusions relate to optical properties based on purely particle-particle interactions and a stable plasma.

Within the above confines, there are various issues to be addressed which we have begun to do in this work. They relate to 1) dependence of emissions on the neutral atmospheric composition and 2) sensitivity of these emissions to the incident electron spectrum. One would hope that a measure of the right set of intensities could yield both composition information and a useful description of the incident electron spectrum. By useful, we mean that the description is adequate to allow specification of, say, the associated electron density altitude profile to within some limit of tolerance defined by its application.

We have not yet carried out our analysis to the point of providing firm answers to questions of a practical nature related to degrees of uncertainty in the deduced parameters. It is clear, though, that accurate measurements of intensities such as those considered here will have useful diagnostic value in establishing dominant regions of excitation and ionization.

#### ACKNOWLEDGEMENTS

This work was partially sponsored by the DMSP Program Office, Space Division, Air Force Systems Command.

(km) z	(°K) T <sub>a</sub>	(cm <sup>-3</sup> ) N <sub>2</sub>	(cm <sup>-3</sup> ) O <sub>2</sub>	(cm <sup>-3</sup> ) O	(cm <sup>-3</sup> ) NO
250	950	5.5 ( 8)	2.9 ( 7)	1.5 ( 9)	1.2 (6)
200	885	3.2 ( 9)	2.1 ( 8)	4.3 ( 9)	7.0 (6)
150	664	3.1 (10)	2.7 ( 9)	1.8 (10)	4.2 (7)
125	408	2.0 (11)	2.1 (10)	6.5 (10)	7.0 (7)
110	242	1.6 (12)	2.6 (11)	2.3 (11)	7.2 (7)
100	194	9.4 (12)	2.1 (12)	4.6 (11)	6.0 (7)
90	190	5.6 (13)	1.5 (13)	2.4 (11)	2.0 (7)
80	210	3.2 (14)	1.0 (14)	3.2 (10)	-

Table 1. Model atmosphere used in the calculations. The N<sub>2</sub>, O<sub>2</sub>, and O densities come from Jacchia (1977). The NO density comes from chemistry modeling by us.

State	Bands/Line	Threshold (ev)	$\sigma_{\max}$ ( $\text{cm}^2$ )	$E(\sigma_{\max})$ (ev)	Reference
$\text{N}_2^+ (\text{B } ^2\Sigma_v^+)$	IN	18.7	2.6 (-17)	100	Borst & Zipf (1970)
$\text{N}_2 (\text{a } ^1\Pi_g)$	LBH	8.5	3.8 (-18)	17	Borst (1972)
$\text{O } (^5\text{S})$	1356 A	9.1	2.5 (-17)	15	Stone & Zipf (1974)

Table 2 Electron impact cross section information for the excited states of interest in this work.

BAND HEAD (A)	$v', v''$	EMISSION FACTOR (%)	O <sub>2</sub> PURE ABSORPTION CROSS SECTION ( $10^{-18} \text{ cm}^2$ )
1273	6,0	1.5	0.09
1325	4,0	4.9	2.0
1354	3,0	6.0	7.1
{1384} {1382}	{2,0} {5,2}	{4.9} {1.0}	13.0
3914	0,0	64.8	0.0

Table 3 Emission factors and O<sub>2</sub> pure absorption cross sections for the 3914 A and LBH bands under investigation. The emission factors are given as percents of the total  $a^{1-\pi}_g$  production.

# FIGURE CAPTIONS

- Figure 1. An Auroral FUV spectrum from P.D. Feldman (private communication, 1981) obtained in a rocket experiment with the spectrometer looking down from above the emitting region. Dashed curve gives the  $O_2$  photo absorption cross section. Altitude scale on right is to be used with adjacent cross section scale.
- Figure 2. Nadir viewing FUV photometer data obtained on satellite S 3-4 (Huffman et al., 1981). Peak sensitivity occurs at 1550 Å. Data show latitudinal distributions of the continuous and discrete auroras.
- Figure 3.  $O_2$  pure absorption optical depths for the LBH bands under investigation. These are obtained using the Jacchia (1977) model atmosphere.
- Figure 4. Density ratio profiles with the ratio given by the density values from Table 3 (Jacchia, 1977) divided by the corresponding values from the model reported by Rees et al. (1977) and Sharp et al. (1979).
- Figure 5.  $N_2$  ( $a^1\Pi_g$ ) volume production rates for incident electron spectra given by Maxwellian (upper panel) and Gaussian (lower panel) distributions. All incident fluxes contain  $1 \text{ erg/cm}^2\text{-s}$ .
- Figure 6. Similar to Figure 5 except for  $O(^5S)$ .
- Figure 7. Nadir viewing intensities versus characteristic energy  $E_M$  for incident electron spectra given by Maxwellian distributions. Each distribution contains  $1 \text{ erg/cm}^2\text{-s}$ .
- Figure 8. Similar to Figure 7 except for incident electron spectra given by Gaussian distributions.
- Figure 9. Nadir viewing intensities versus incident electron energy content  $Q_0$  for Maxwellian distributions with  $E_0 = 2.5 \text{ keV}$ .

- Figure 10. Nadir viewing intensities versus  $z_p$ , the altitude of peak energy deposition.
- Figure 11. OI 1356 A and LBH 1354 A nadir viewing intensities for two  $n(0)$  models.
- Figure 12. LBH nadir viewing intensities for three different  $O_2$  density distributions. The unscaled distribution is that given in Table 1.
- Figure 13. Total ion production rates and electron densities for Maxwellian distributions with  $Q_M = 1 \text{ erg/cm}^2\text{-s}$ .
- Figure 14. Similar to Figure 13 except for Gaussian distributions.

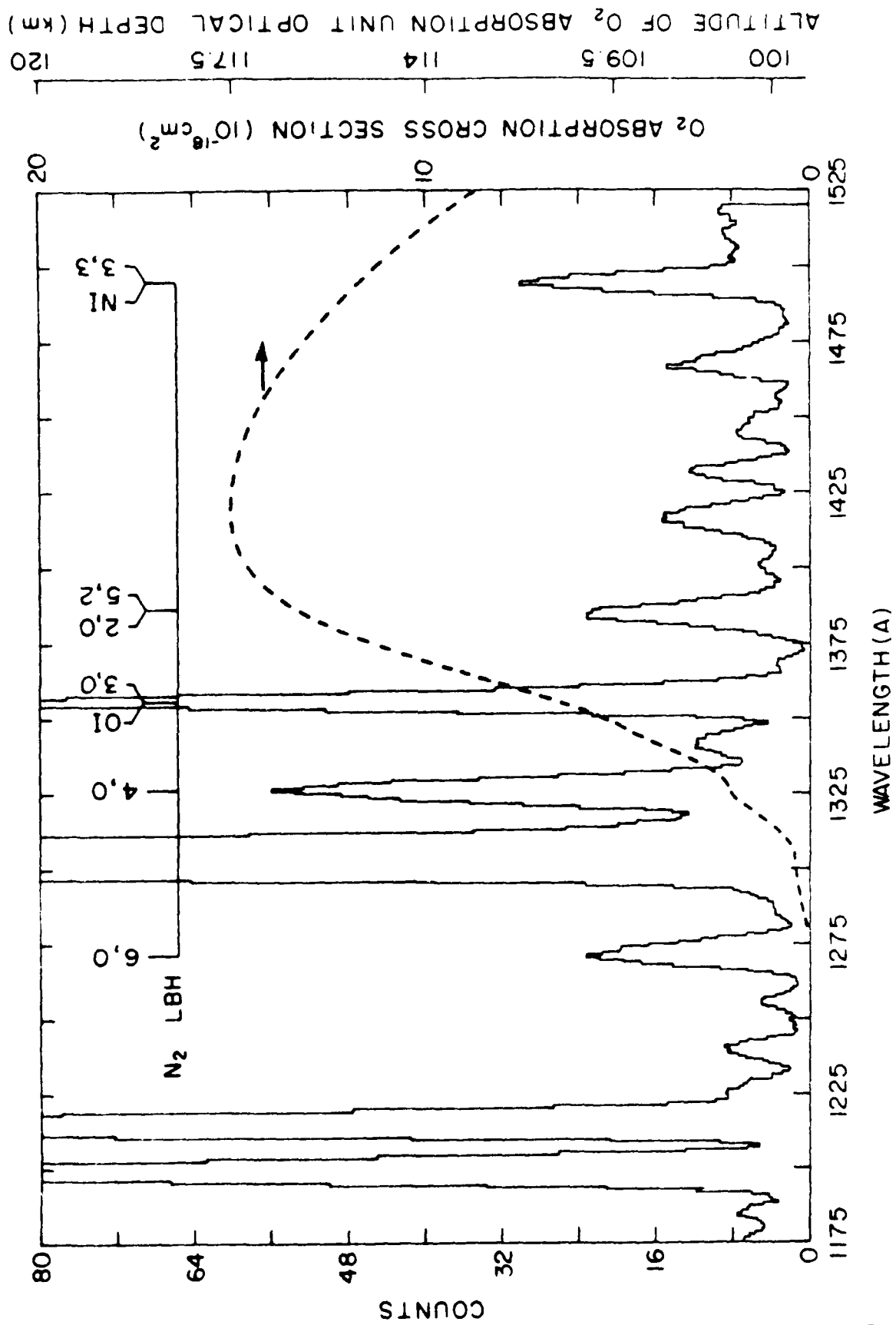


Fig. 1

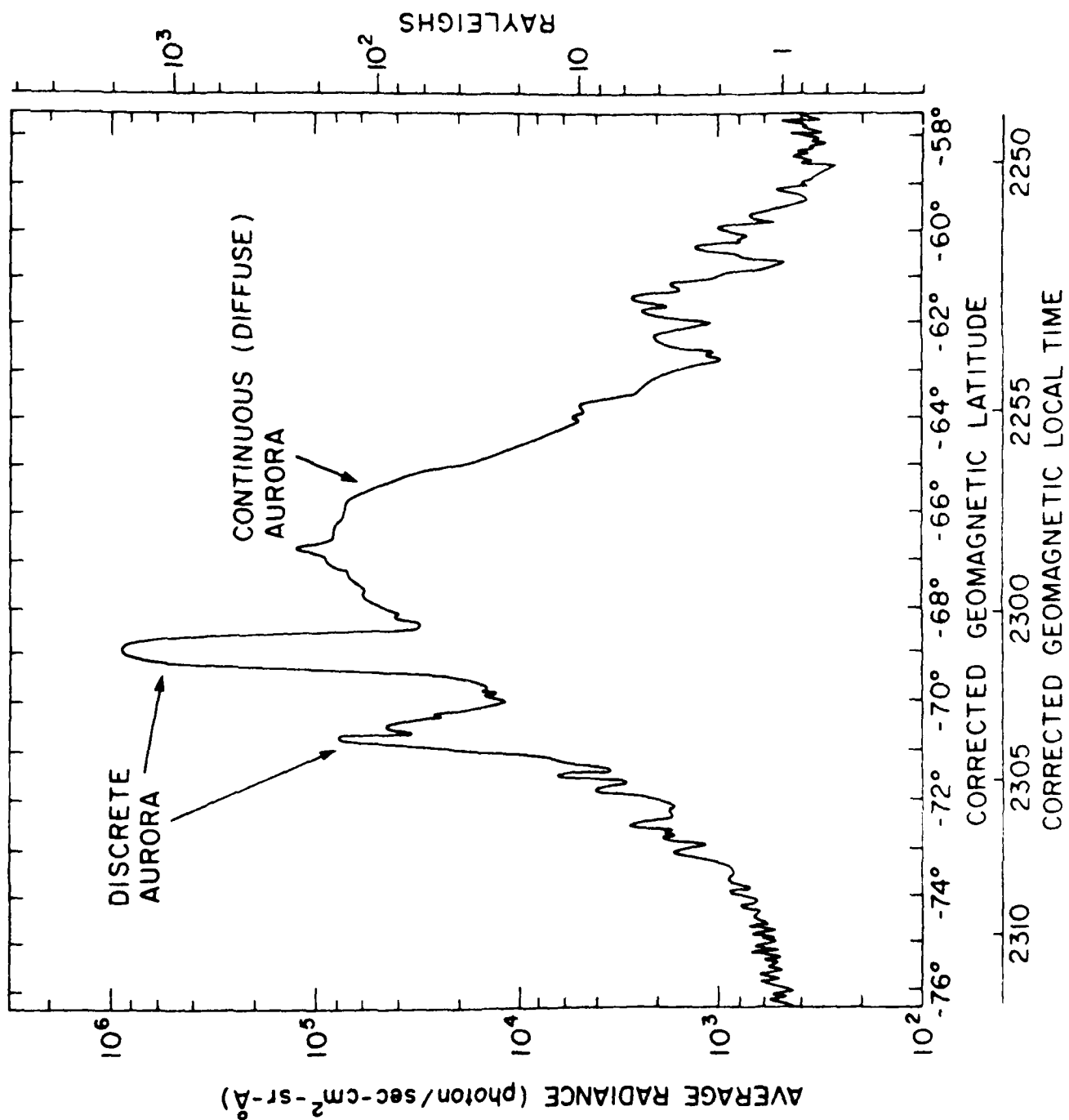


Fig. 2

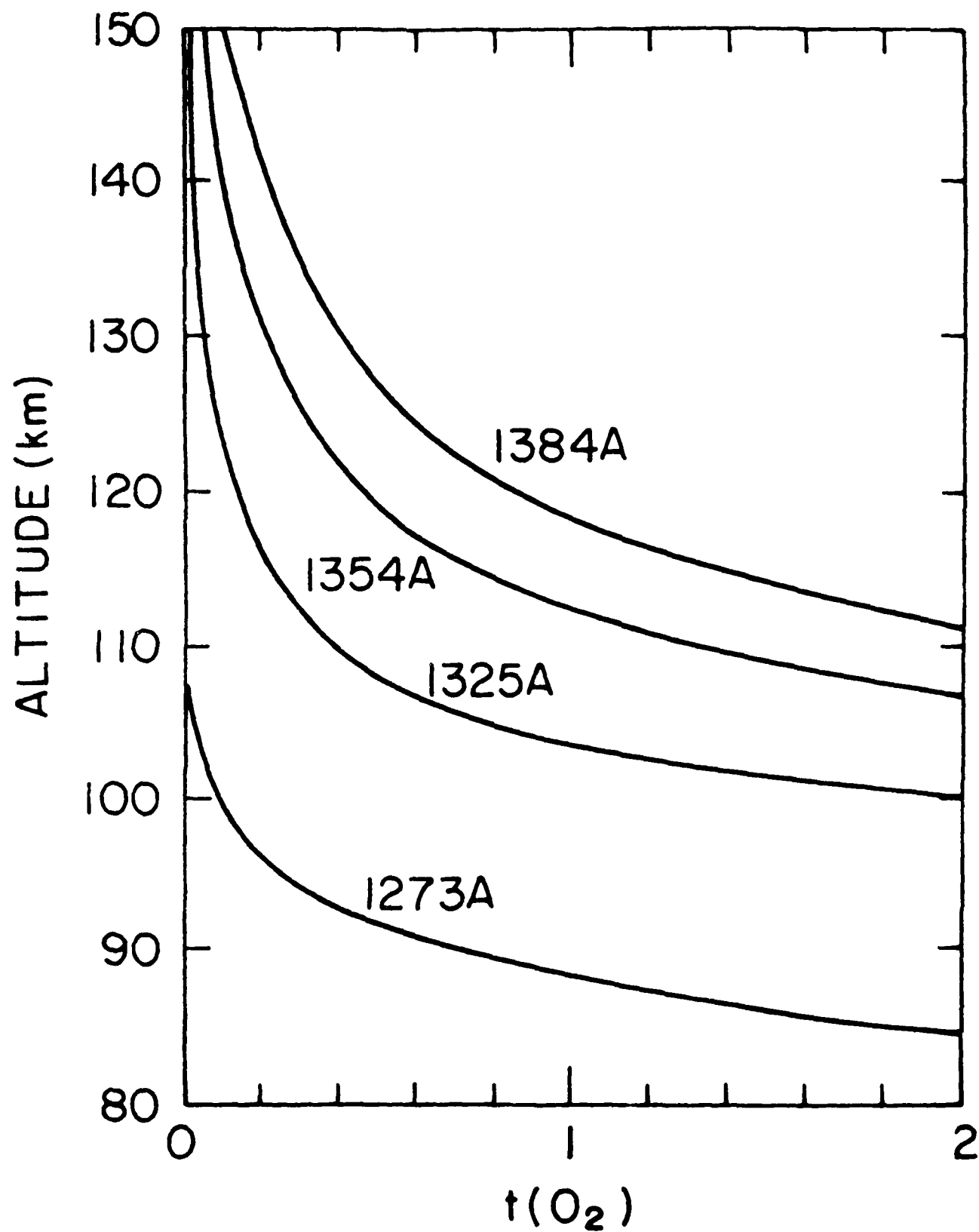


Fig. 3

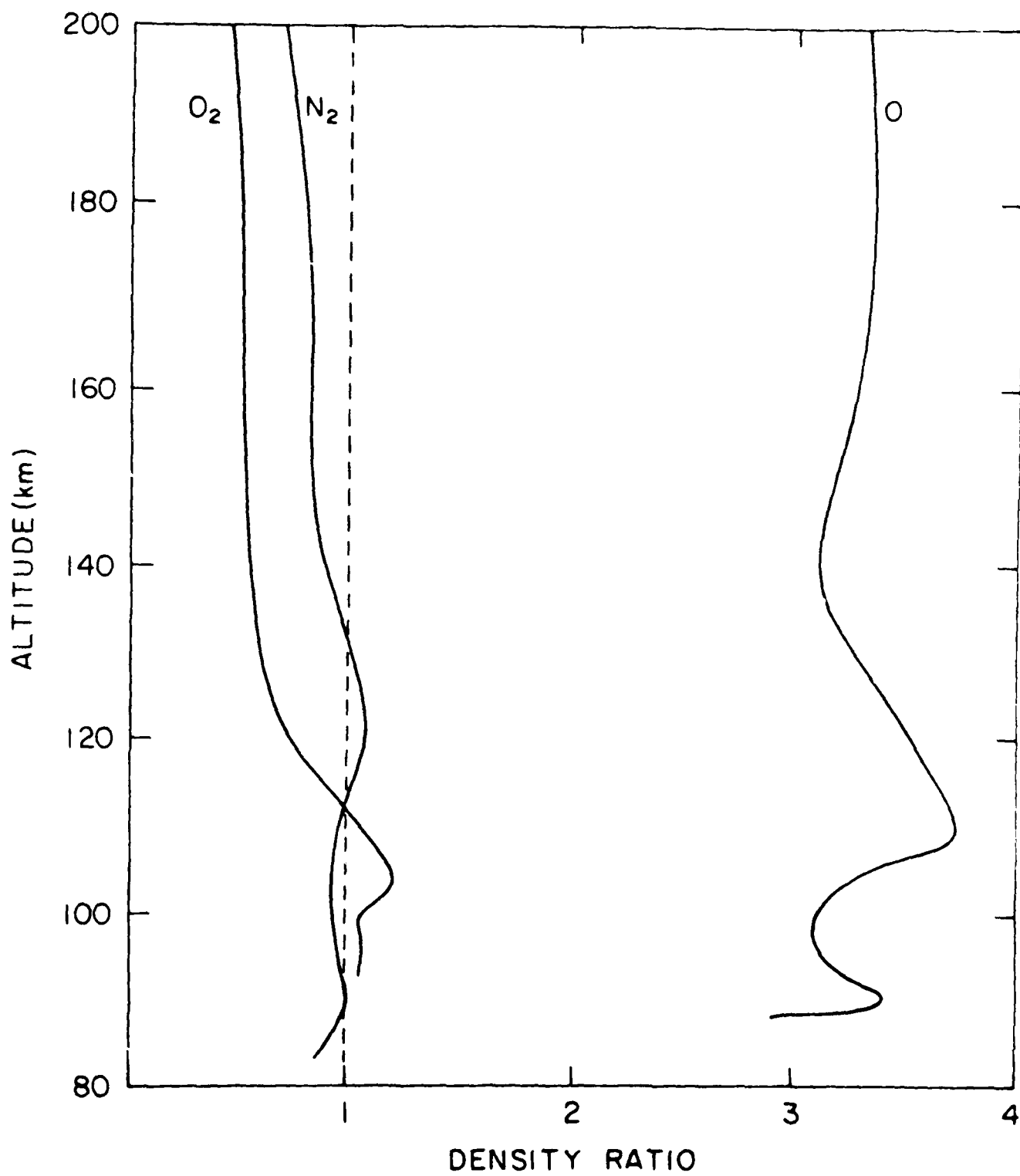


Fig. 4

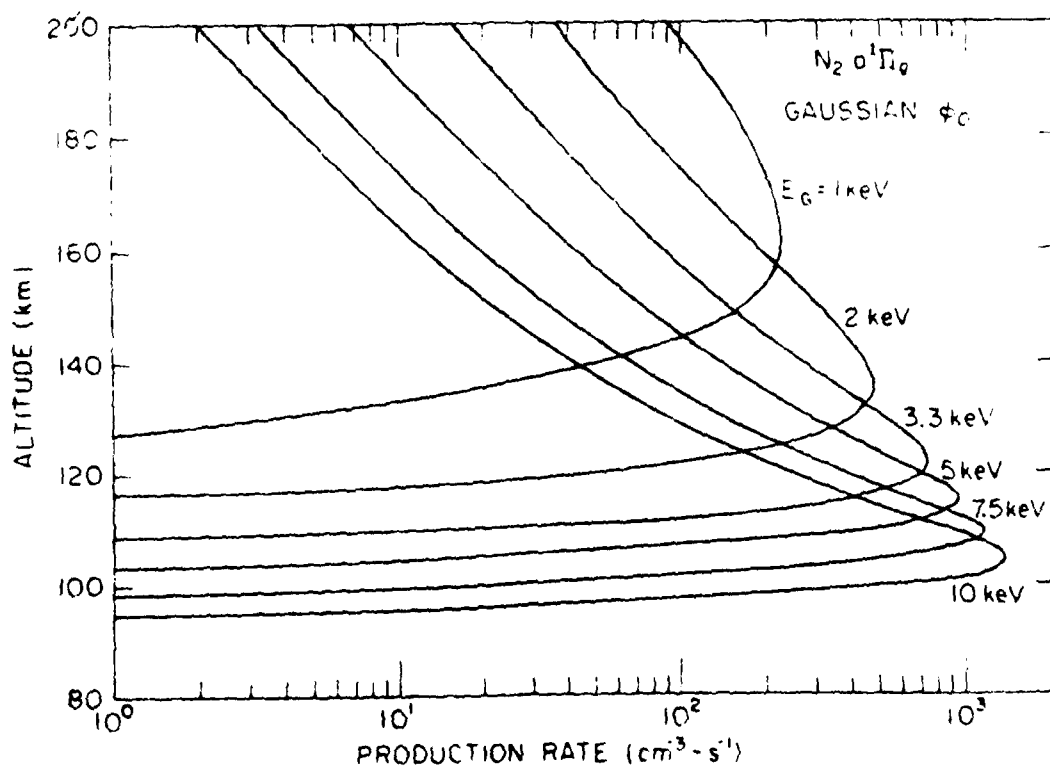
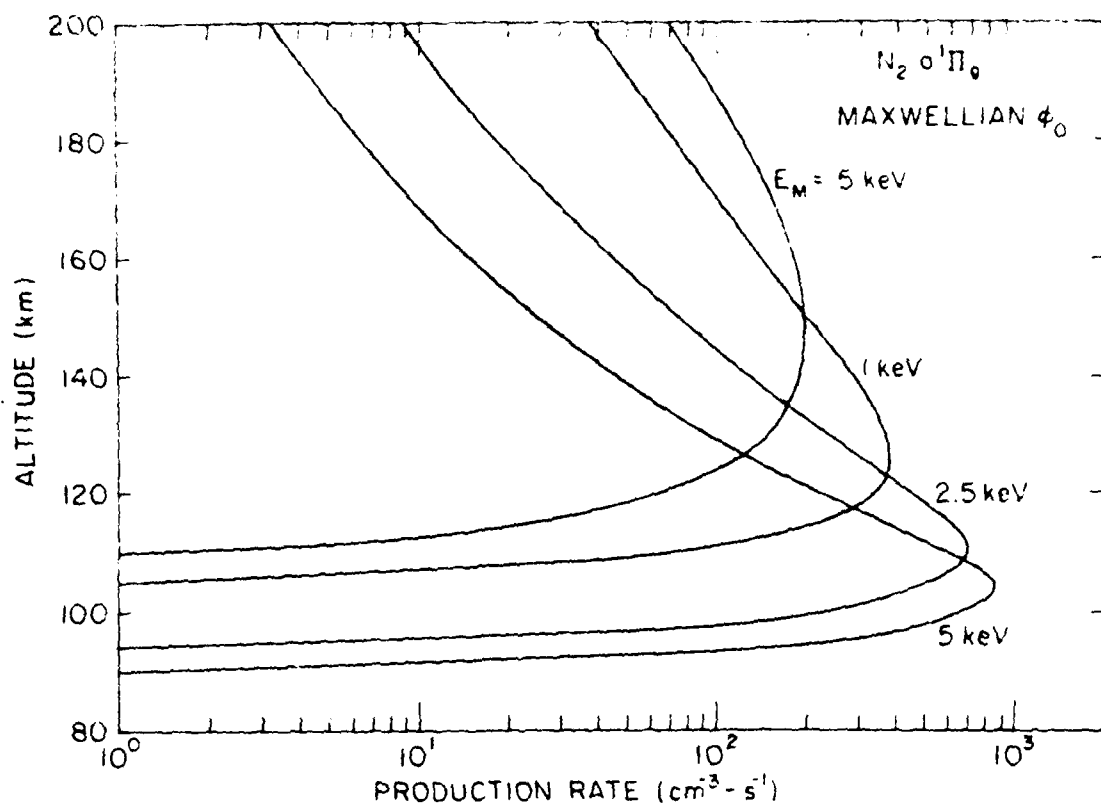


Fig. 5

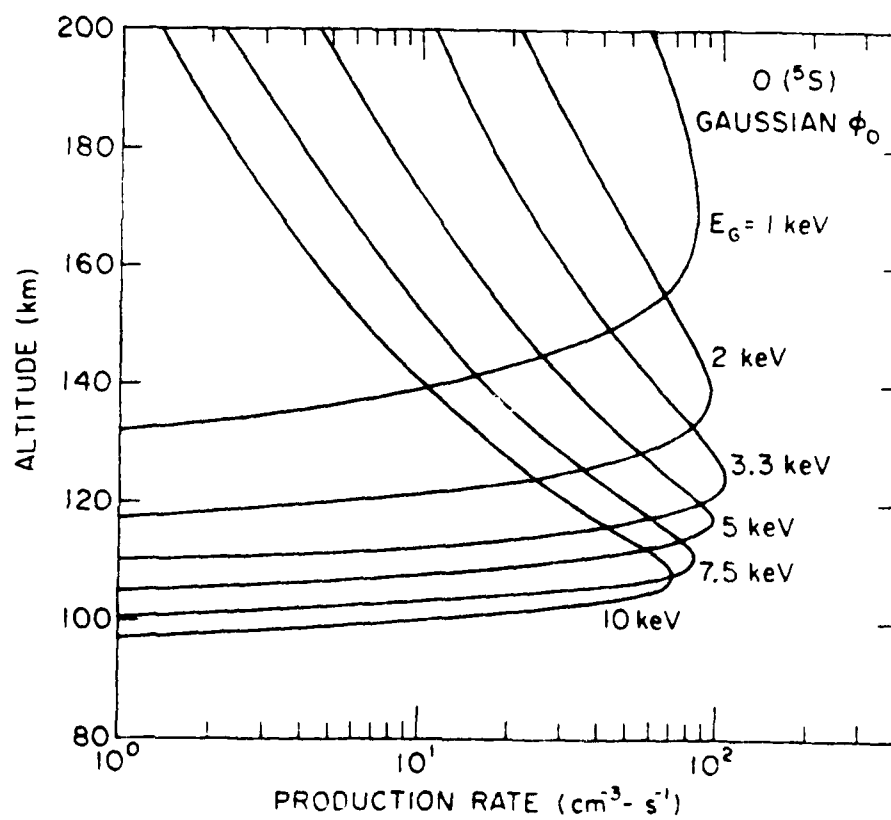
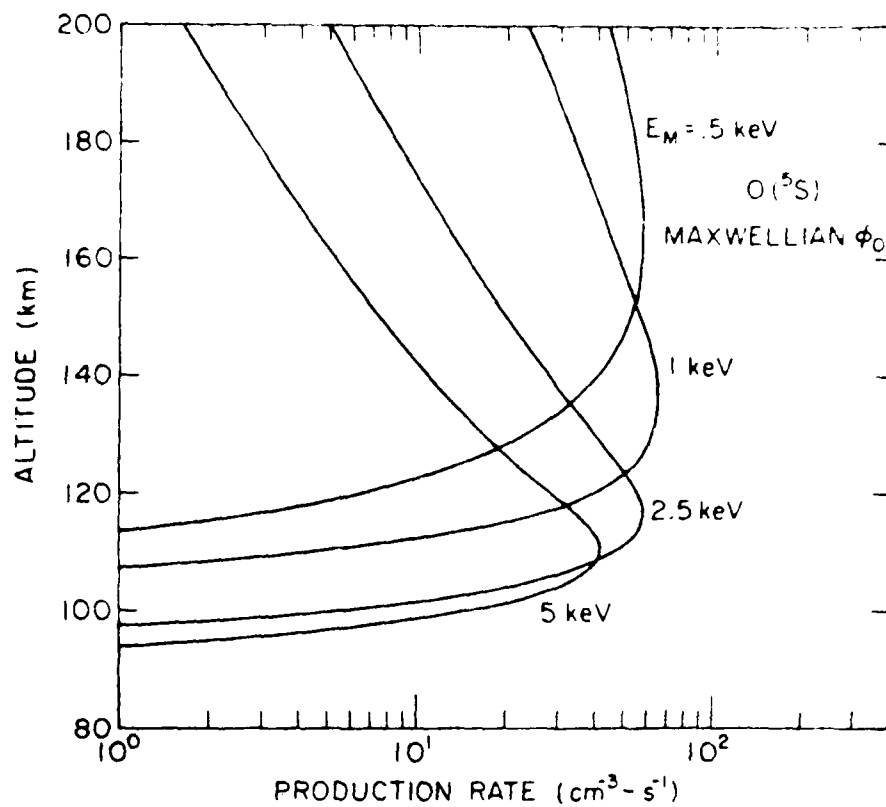


Fig. 6

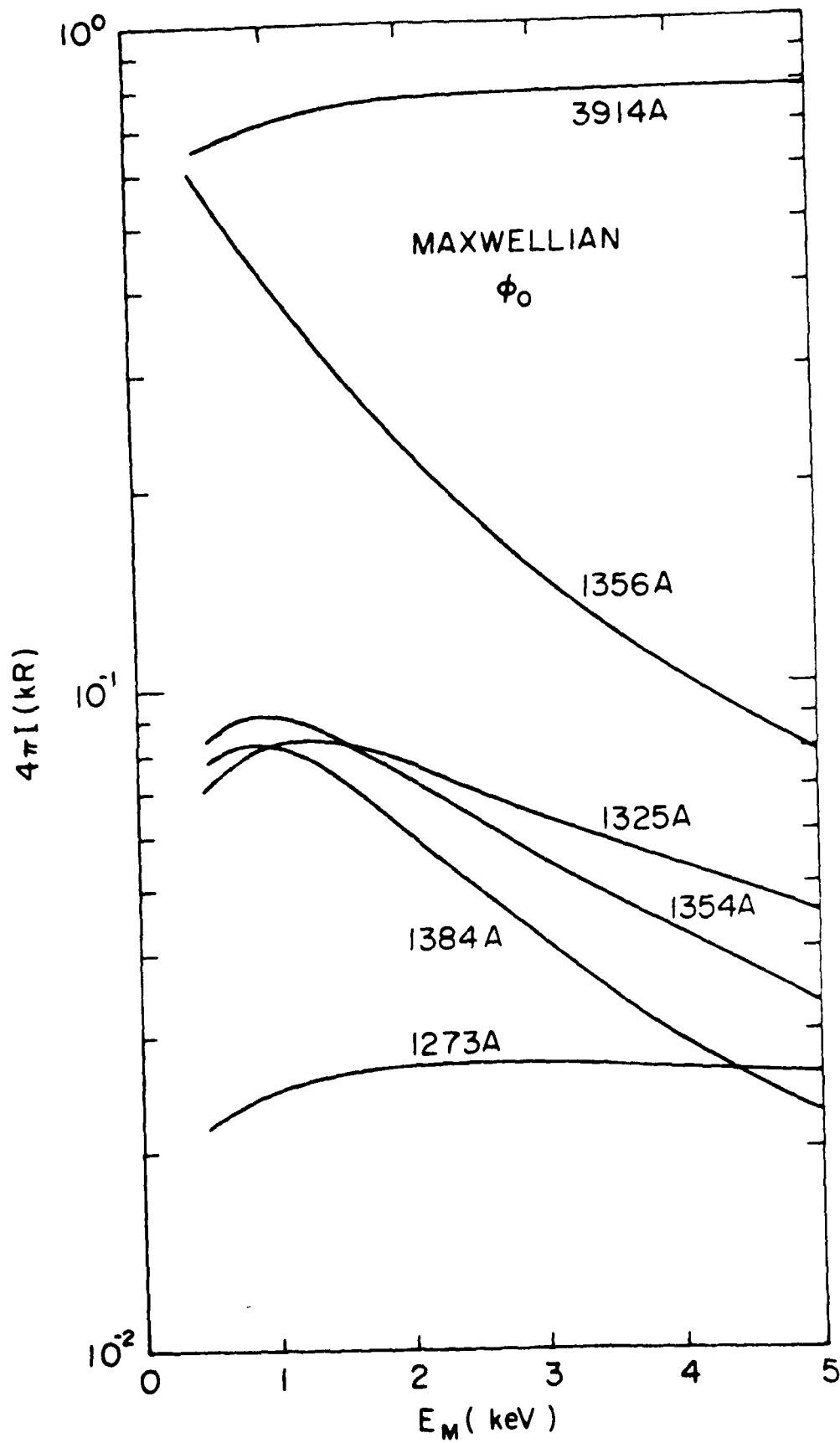


Fig. 7

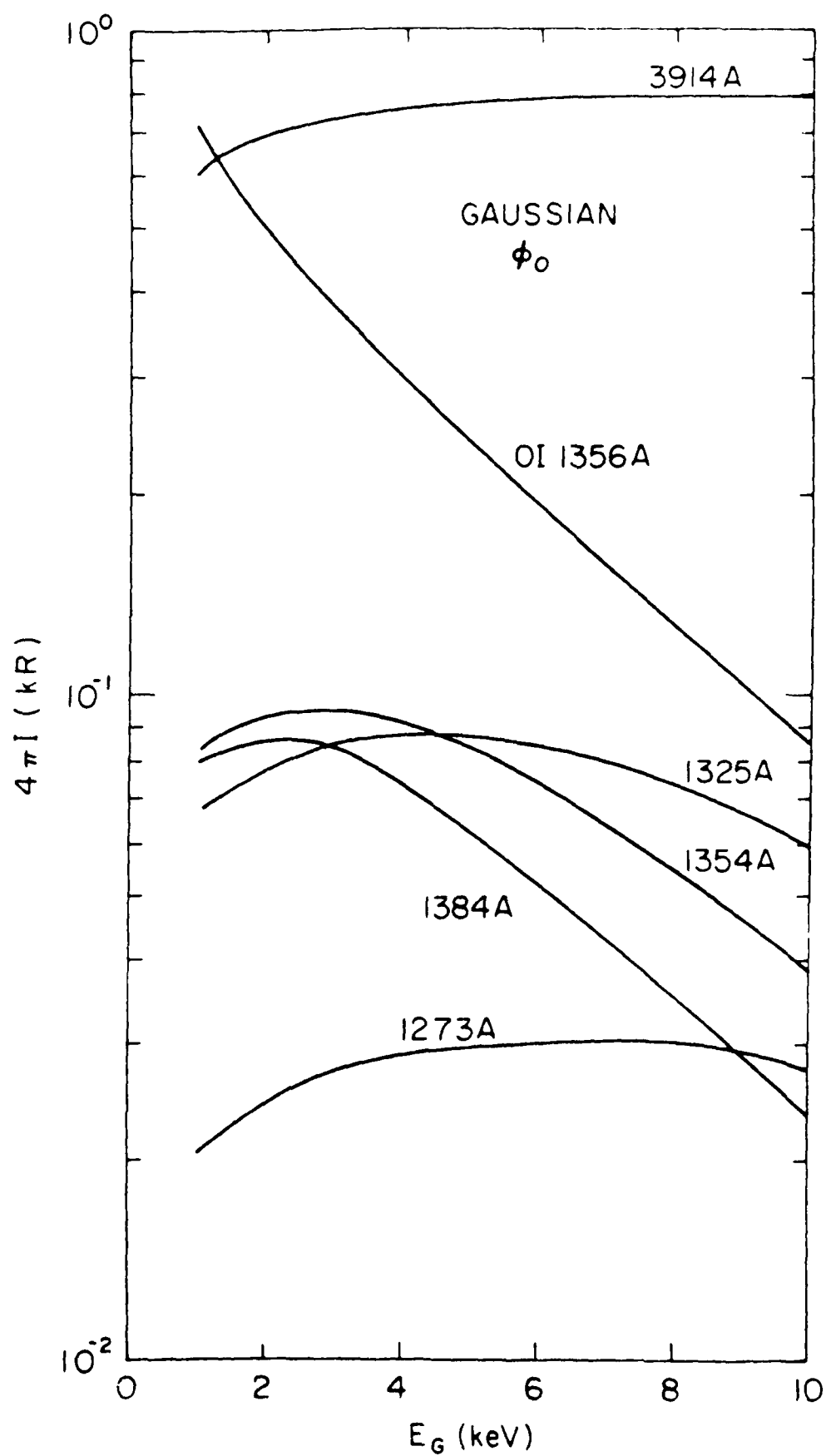


Fig. 8

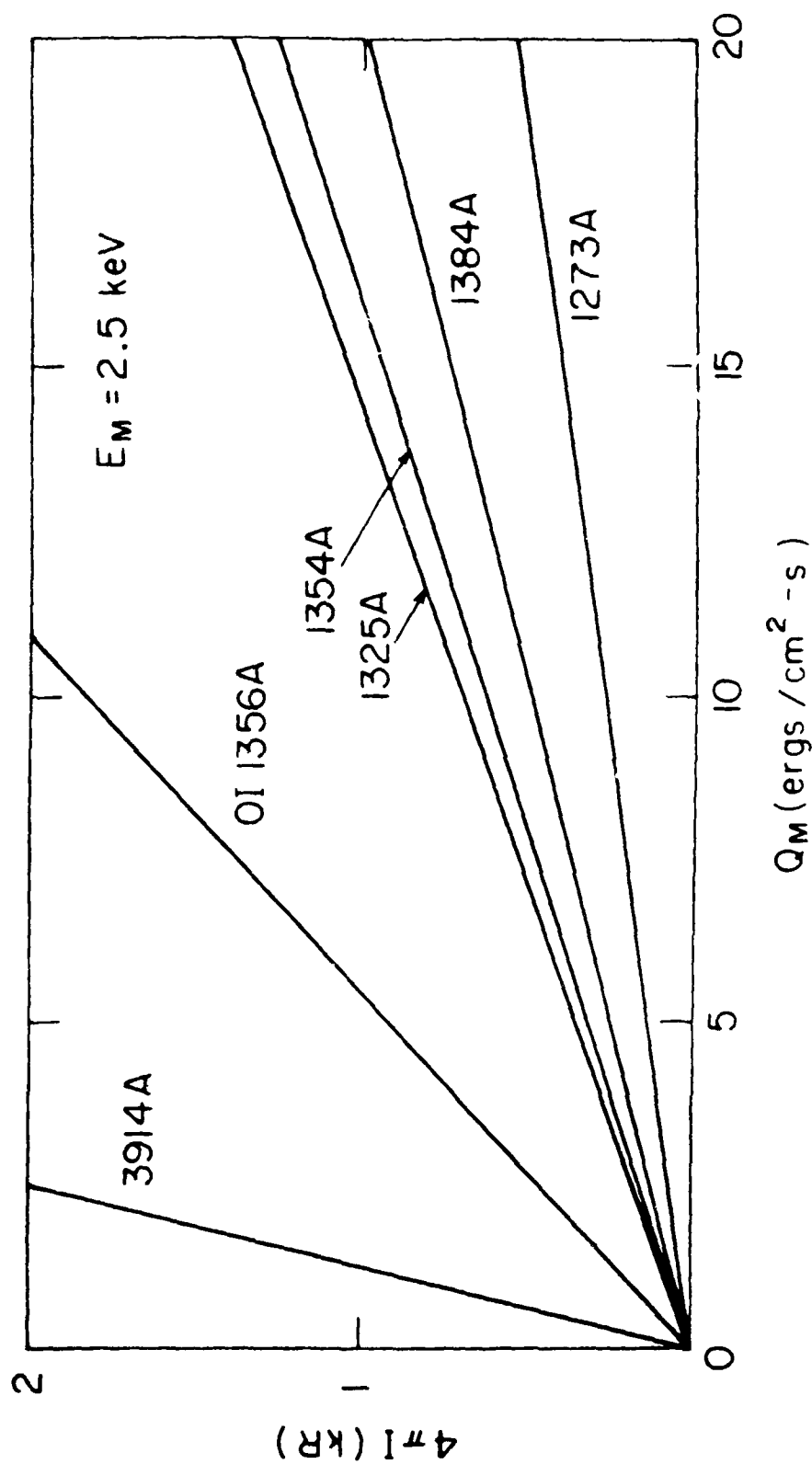


Fig. 9

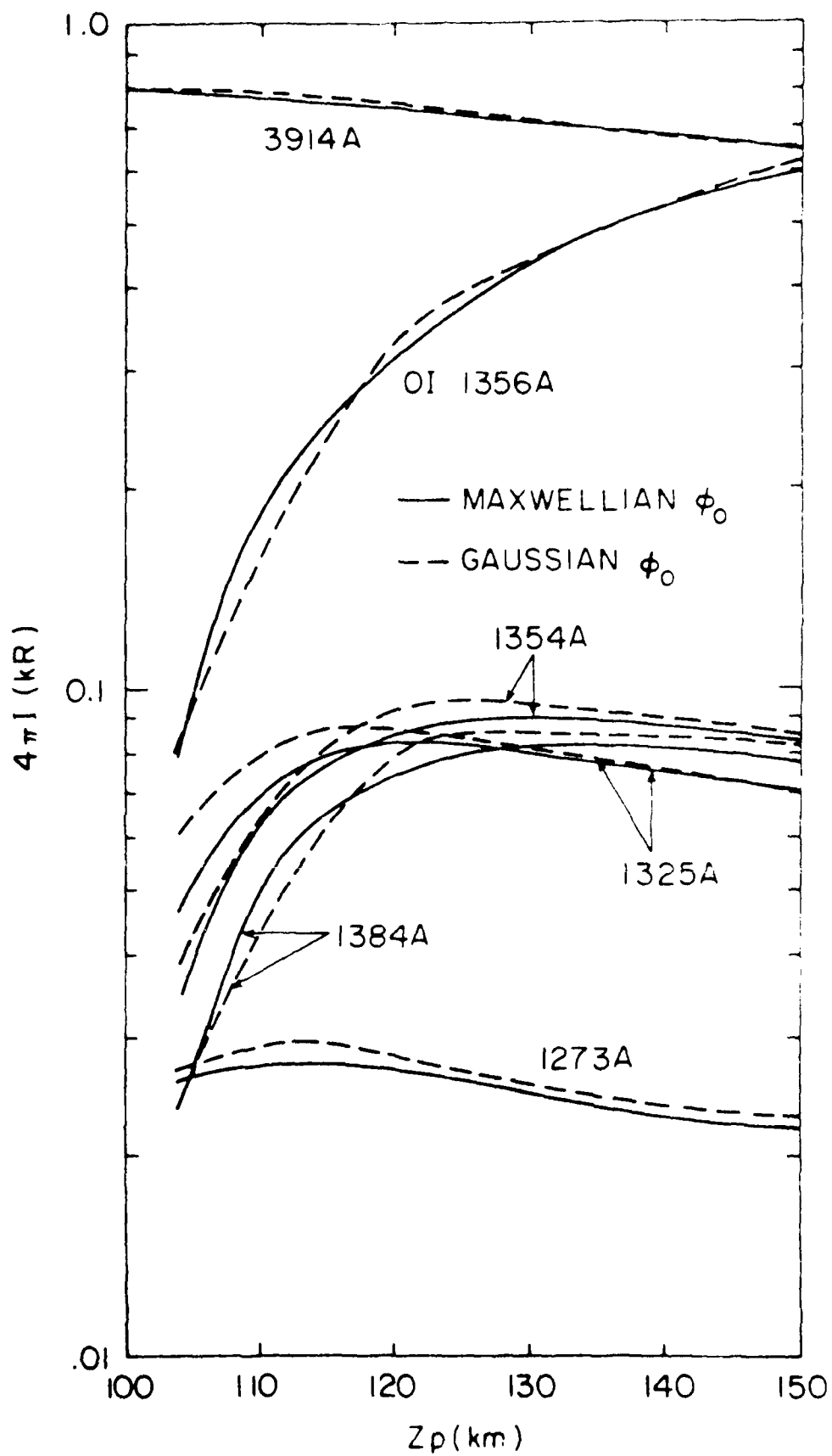


Fig. 10

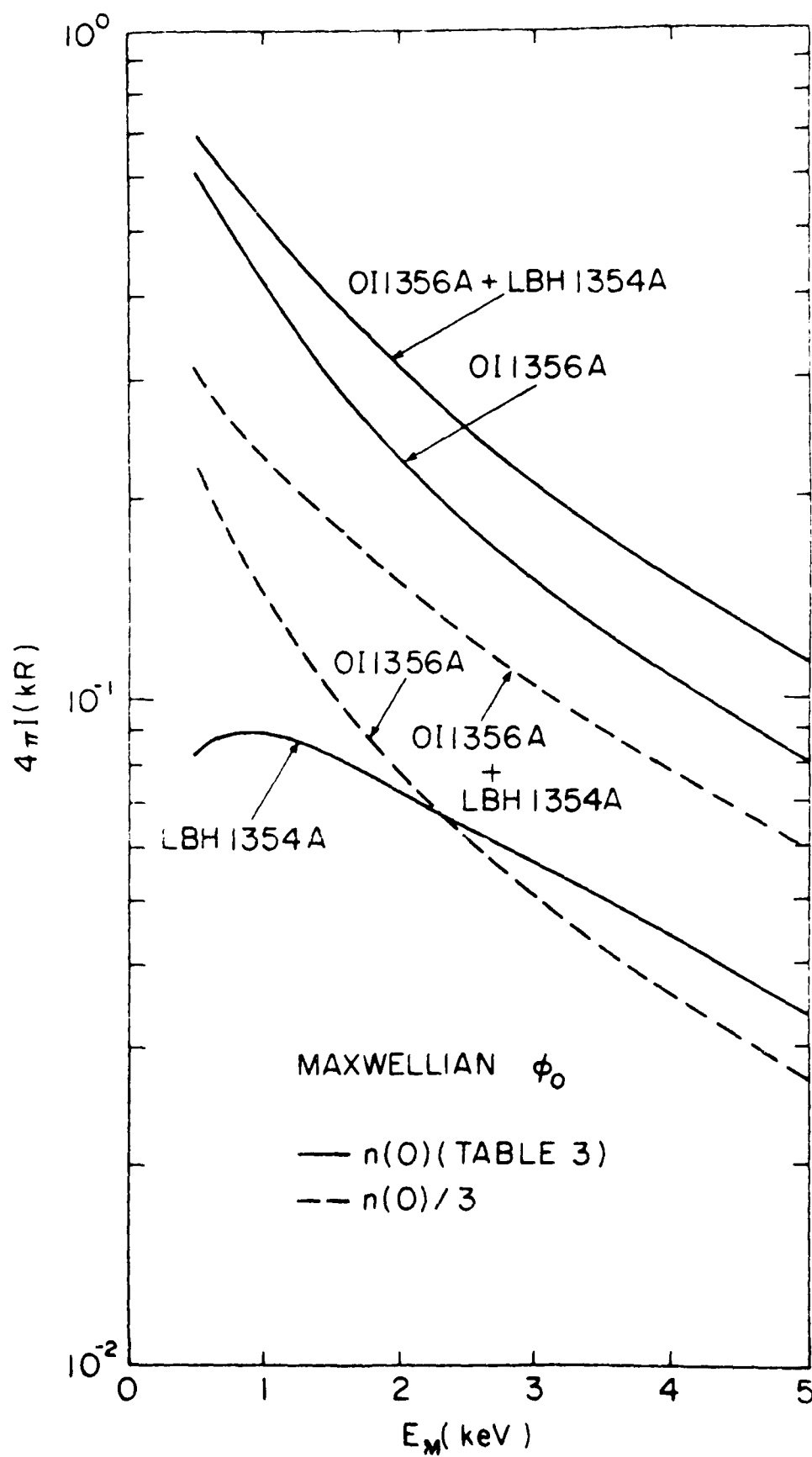


Fig. 11

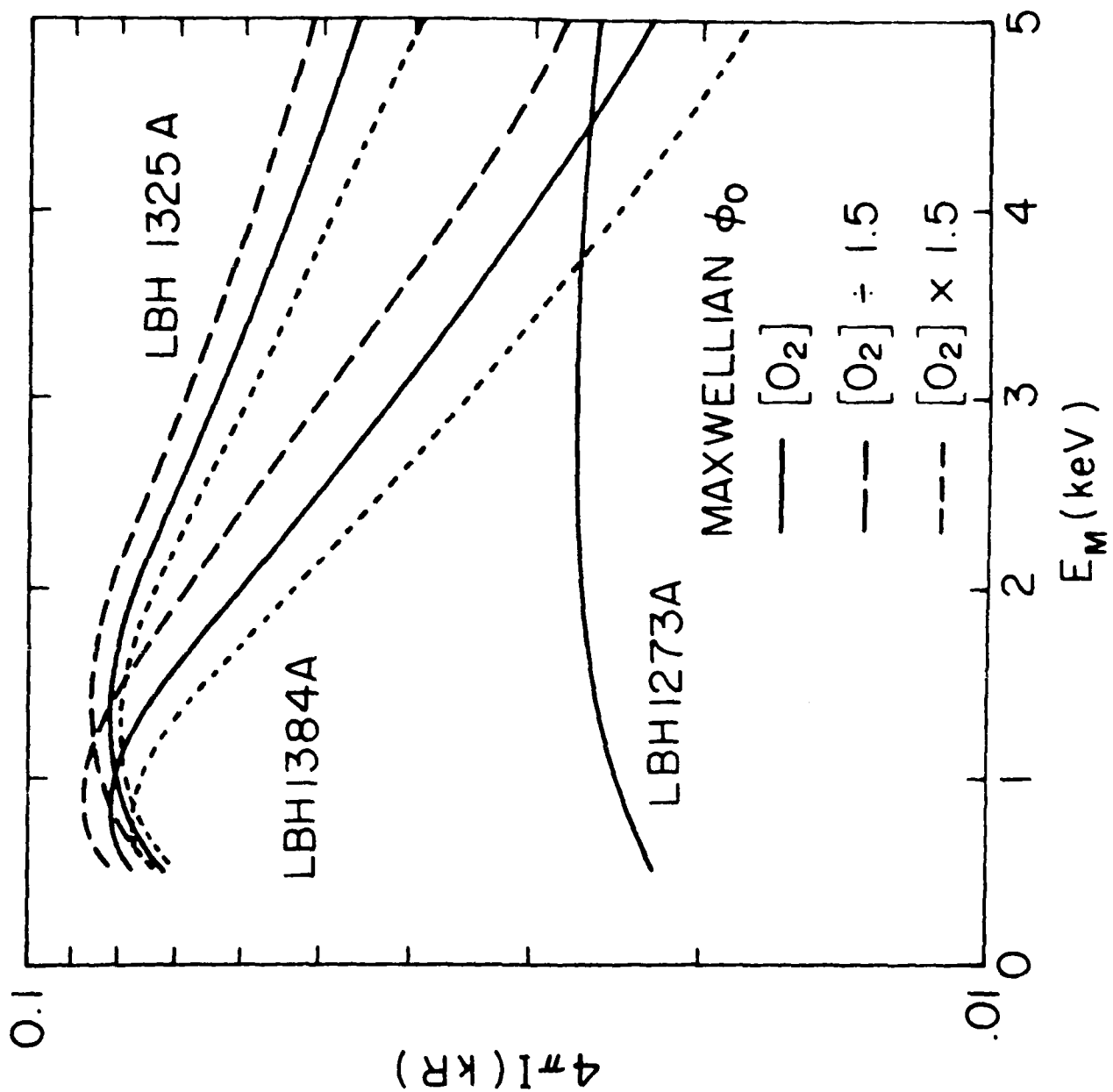
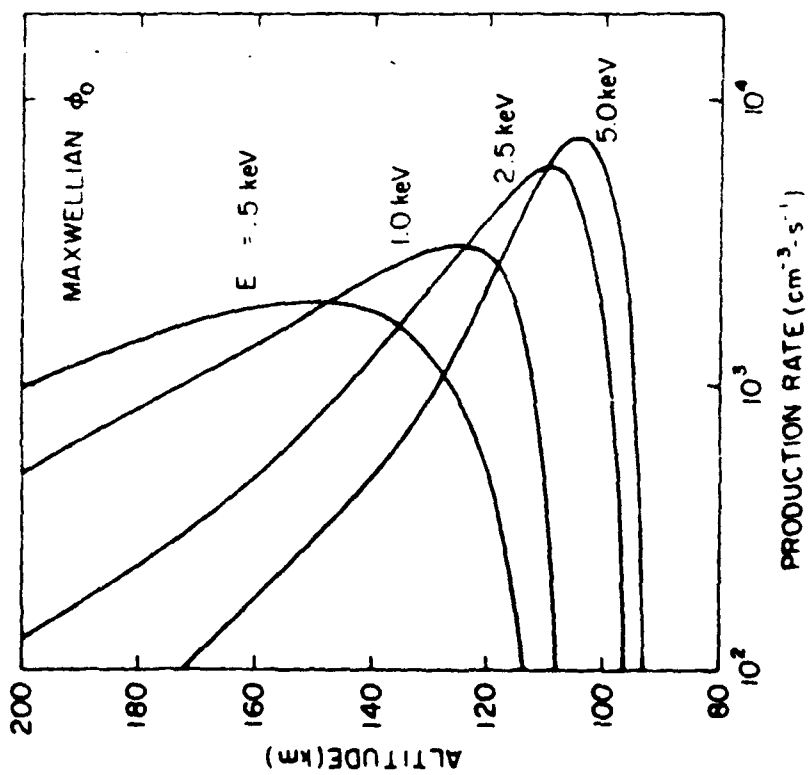
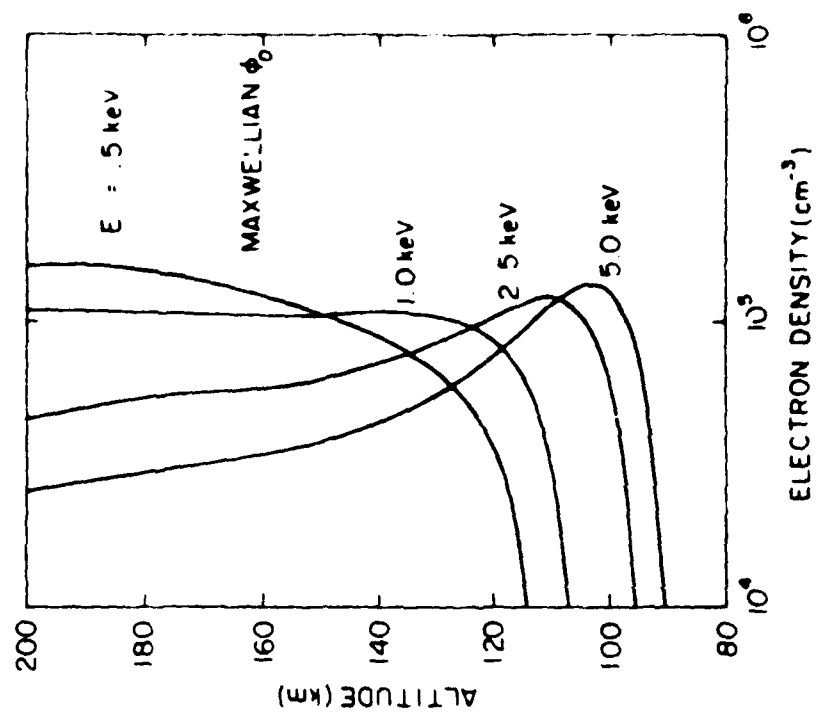


Fig. 12



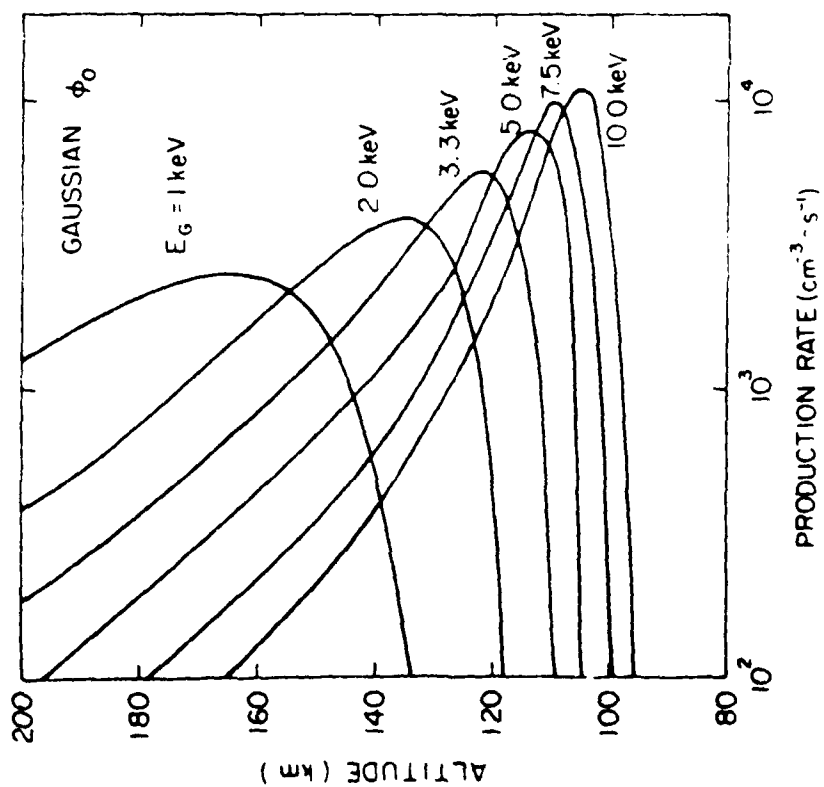
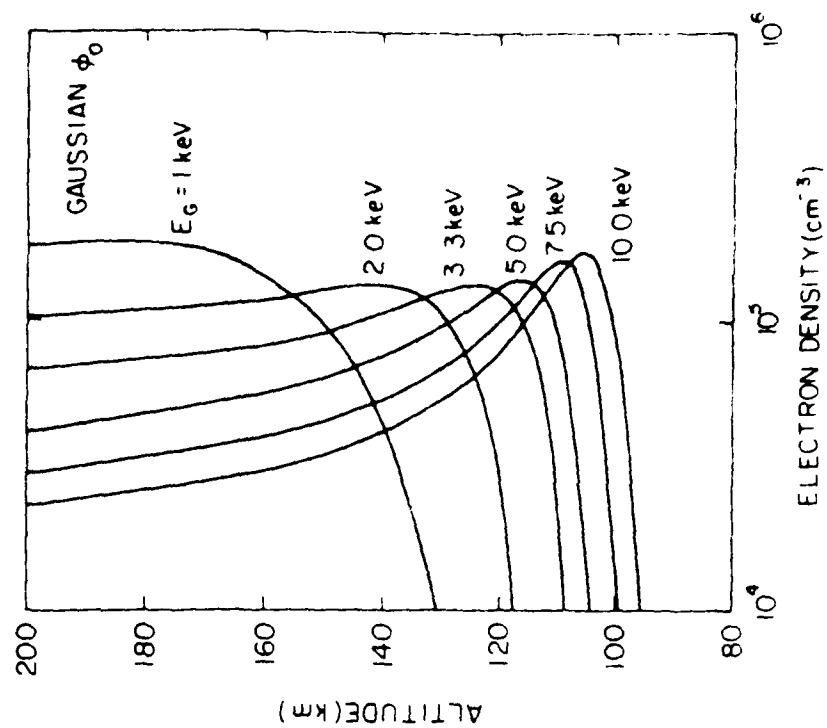


Fig. 14

## REFERENCES

- Anderson, D.E., R.R. Meier, P.D. Feldman and E.P. Gentieu,, The UV Dayglow 3, OI Emissions at 989, 1027, 1152, 1304 and 1356 A, Geophys. Res. Lett., 7, 1057, 1980.
- Arnoldy, R.I. and P.B. Lewis, Jr., Correlation of Ground-Based and Topside Photometric Observations with Auroral Electron Spectra Measurements at Rocket Altitudes, J. Geophys. Res., 82 5563, 1977.
- Borst, W.L. , Excitation of Several Important Metastable States of  $N_2$  by Electron Impact, Phys. Rev. A, 5, 648, 1972.
- Borst, W.L. and E.C. Zipf, Cross Section for Electron-Impact Excitation of the (0,0) First Negative Band of  $N_2^+$  from Threshold to 3 keV, Phys. Rev. A 1, 834, 1970.
- Boyd, J.S., Rocket-borne Measurements of Auroral Electrons, Rev. Geophys., 13, 735, 1975.
- Conway, R.R., Self-Absorption of the  $N_2$  Lyman-Birge-Hopfield Bands in the Far Ultraviolet Dayglow, J. Geophys. Res., 87, 859, 1982.
- Evans, D.S., Precipitating Electron Fluxes Formed by a Magnetic Field-aligned Potential Difference, J. Geophys. Res., 79, 2853, 1974.
- Feldman, P.D. and E.P. Gentieu, The Ultraviolet Spectrum of an Aurora 530-1520 A, J. Geophys. Res., 87, 2453, 1982.
- Forthem, E.G., K. Stasiewicz, M.O. Chandler, R.S.B. Ong, E. Gombosi and R.A. Hoffman, Statistical Study of Precipitating Electrons, J. Geophys. Res., 87, 3469, 1982.
- Gentieu, E.P., D. Feldman and R.R. Meier, Spectroscopy of the Extreme Ultraviolet Dayglow at 6.5 A Resolution: Atomic and Ionic Emissions Between 530 and 1240 A. Geophys. Res. Lett., 6, 325, 1979.
- Holstein, T., Imprisonment of Resonance Radiation in Gases, Phys. Rev., 72, 1212, 1947.
- Huffman, R.E., D.E. Paulsen, F.J. LeBlanc, and J.C. Larrabee, Ionospheric and Auroral Measurements from Space Using Vacuum Ultraviolet Emission, in "The Effects of the Ionosphere on Radiowave Systems", edited by J.F. Goodman, U.S. Government Printing Office, Washington, D.C., 1981.
- Huffman, R.E., F.J. LeBlanc, J.C. Larrabee and D.E. Paulson, Satellite Vacuum Ultraviolet Airglow and Auroral Observations, J. Geophys. Res., 85, 2201, 1980.

Jacchia, L.G., Thermospheric Temperature, Density, and Composition: New Models, Smithsonian Astrophysical Observatory Special Report No. 375, 1977.

Jasperse, J.R. and B. Basu, Transport Theoretic Solutions for Auroral Proton and H Atom Fluxes and Related Quantities, J. Geophys. Res., 87, 811, 1982.

Lui, A.T.Y., D. Venkatesan, C.D. Anger, S-I. Akasofu, W.J. Heikkila, J.D. Winningham, and J.R. Burrows, Simultaneous Observations of Particle Precipitations and Auroral Emissions by the Isis 2 Satellite in the 19-24 MLT Sector, J. Geophys. Res., 82, 2210, 1977.

McLaughlin, R.W., P.W. Erdman, and E.C. Zipf, On the Excitation of the N<sub>2</sub> LBH system in the Airglow and Aurora, EOS, 63, 394, 1982.

Meier, R.R., D.J. Strickland, P.D. Feldman and E.P. Gentieu, The Ultraviolet Dayglow 1. Far UV Emissions of N and N<sub>2</sub>, J. Geophys. Res., 85, 2177, 1980.

Meier, R.R., R.R. Conway, P.D. Feldman, D.J. Strickland, and E.P. Gentieu, Analysis of Nitrogen and Oxygen Far UV Auroral Emissions, J. Geophys. Res., 87, 2444, 1982.

Meier, R.R. and J.-S. Lee, An Analysis of the OI 1304 A Dayglow Using a Monte Carlo Resonant Scattering Model with Partial Frequency Redistributing, Planet. Space Sci., 30, 439, 1982.

Oran, E.S. and D.J. Strickland, Photoelectron Flux in the Earth's Ionosphere, Planet. Space Sci., 26, 1161, 1978.

Rearwin, S. and E.W. Hones, Jr., Near-Simultaneous Measurement of Low-energy Electrons by Sounding Rocket and Satellite, J. Geophys. Res., 79, 4322, 1974.

Rees, M.H. and D. Luckey, Auroral Electron Energy Derived from Ratios of Spectroscopic Emissions, 1. Model Computations, J. Geophys. Res., 79, 5181, 1974.

Rees, M.H., A.I. Stewart, W.E. Sharp, P.B. Hays, R.A. Hoffman, L.H. Brace, J.F. Doering and W.K. Peterson, Coordinated Rocket and Satellite Measurements of an Auroral Event, 1. Satellite Observations and Analysis, J. Geophys. Res., 82, 2250, 1977.

Robinson, R.M., R.R. Vondrak and T.A. Potemra, Electrodynamic Properties of the Evening Sector Ionosphere Within the Region 2 Field-Aligned Current Sheet, J. Geophys. Res., 87, 731, 1982.

Roble, R.G. and M.H. Rees, Time-Dependent Studies of the Aurora: Effects of Particle Precipitation on the Dynamic Morphology of Ionospheric and Atmospheric Properties, Planet. Space Sci., 25, 991, 1977.

Sharber, J.R., The Continuous (Diffuse) Aurora and Auroral-E Ionization, "Physics of Space Plasmas" edited by T.S. Chang, B. Coppi, and J.R. Jasperse, SPI Conference Proceedings and Reprint Series, 4, (Scientific Publishers, Cambridge, MA, 1981).

Sharp, W.E., M.H. Rees and A.I. Stewart, Coordinated Rocket and Satellite Measurements of an Auroral Event, 2, The Rocket Observations and Analysis, J. Geophys. Res., 84, 1977, 1979.

Shepherd, G.G., J.D. Winningham, F.E. Bunn and F.W. Thirkettle, An Empirical Determination of the Production Efficiency for Auroral 6300 Å Emission by Energetic Electrons, J. Geophys. Res., 85, 715, 1980.

Stone, E.J. and E.C. Zipf, Electron Impact Excitation of the  $^3S$  and  $^5S$  States of Atomic Oxygen, J. Chem. Phys., 60, 4237, 1974.

Strickland, D.J., The Transport of Resonance Radiation in a Nonisothermal Medium - The Effect of a Varying Doppler Width, J. Geophys. Res., 84, 5890, 1979.

Strickland, D.J., D.L. Book, T.P. Coffey and J.A. Fedder, Transport Equation Techniques for the Deposition of Auroral Electrons, J. Geophys. Res., 81, 2755, 1976.

Strickland, D.J. and T.M. Donahue, Excitation and Radiative Transport of OI 1304 Å Resonance Radiation-I. The Dayglow, Planet. Space Sci., 18, 661, 1970.

Strickland, D.J. and D.E. Anderson, Jr., Radiation Transport Effects on the 1356 Å Limb Intensity Profile in the Dayglow, submitted to J. Geophys. Res., 1982.

Torr, M.R. and D.G. Torr, The Role of Metastable Species in the Thermosphere, Rev. Geophys. Space Phys., 20, 91, 1982.

Valance Jones, A. Aurora, Geophys. and Astrophys. Monographs, D. Reidel Publ. Co. 1974.

Valance Jones, A., A Model for the Excitation of Electron Aurora and Some Applications, Can. J. Phys., 53, 2276, 1975.

Vondrak, R.R., Remote Sensing of High-altitude Ionization Profiles by Ground-based and Spaceborne Instrumentation, in "The Effects of the Ionosphere on Radiowave Systems", edited by J.F. Goodman, U.S. Government Printing Office, Washington, D.C., 1981.

Whalen, J.A., General Characteristics of the Auroral Ionosphere, in "Physics of Space Plasmas" edited by T.S. Chang, B. Coppi and J.R. Jasperse, SPI Conference Proceedings and Reprint Series, 4, (Scientific Publishers, Cambridge MA 1981).

Whalen, J.A., and J.R. Sharber, The Night-time Auroral-E Layer: Particle Production, Latitudinal and Longitudinal Structure and Dynamics, in "The Effects of the Ionosphere on Radiowave Systems" edited by J.F. Goodman, U.S. Government Printing Office, Washington, D.C., 1981.

END

DATE  
FILMED

4 - 83

DTIC